Master's thesis in Geography

Physical Geography

NDVI as a proxy for recent carbon accumulation and greening in Svalbard

Mitro Müller

2020

Supervisors:
Docent Minna Väliranta
Professor Miska Luoto

UNIVERSITY OF HELSINKI
FACULTY OF SCIENCE
DEPARTMENT OF GEOSCIENCES AND GEOGRAPHY
DIVISION OF GEOGRAPHY

P.O Box 64 (Gustaf Hällströmin katu 2)
00014 University of Helsinki

Tiedekunta – Fakultet – Faculty	Osasto – Institution – Department
Matemaattis-luonnontieteellinen tiedekunta	Geotieteiden ja maantieteen osasto

Tekijä – Författare – Author

Mitro Müller

Tutkielman otsikko – Avhandlings titel – Title of thesis

NDVI viimeaikaisen hiilen kertymän ja vihertymisen proksiaineistona Huippuvuorilla

Koulutusohjelma ja opintosuunta – Utbildningsprogram och studieinriktning – Programme and study track

Maantieteen koulutusohjelma, luonnonmaantiede

Tutkielman taso – Avhandlings nivå – Level of the thesis	Aika – Datum – Date	Sivumäärä – Sidoantal – Number of pages
Pro Gradu	07.08.2020	105

Tiivistelmä – Referat – Abstract

Maailmanlaajuisissa vuosikeskilämpötiloissa on havaittu lämpenevä kehityssuuntaus esiteolliselta ajalta lähtien. Vuosikeskilämpötilojen muutos Norjan Huippuvuorilla on maailmanlaajuista keskiarvoa voimakkaampaa. Huippuvuorten läntisissä osissa jäätikköjen vetäytyminen on jatkunut jo useita vuosikymmeniä, ja viime vuosikymmeninä biologiset prosessit ovat kiihtyneet. Nämä muutokset ovat todennäköisesti vaikuttaneet Huippuvuorten pääosin sammalpeitteisten tundra-alueiden hiilidynamiikkaan. Alueella on toteutettu vain rajallinen määrä paleoekologisia tutkimuksia, eikä varsinkaan korkeiden leveysasteisten sammalpeitteisten tundra-alueiden vastetta ilmastonmuutokseen vielä täysin ymmärretä.

Tämän tutkimuksen tavoitteena oli tutkia maaperän orgaanisen aineksen ja hiilen kertymisnopeuksien viimeaikaisia muutoksia sammalpeitteisillä tundra-alueilla Huippuvuorilla. Maaperän kairausprofiilit kerättiin neljältä koealalta Spitsbergen -saaren läntisistä osista. Radiohiili (^{14}C) ja lyijyajoitusmenetelmiä (^{210}Pb) käytettiin yhdessä ikä-syvyys -mallien ja maaperän ominaisuusanalyysien kanssa hiilen kertymishistorian rekonstruoimiseksi vuodesta 1900 jKr vuoteen 2018 jKr asti. Päätelmiä tukivat meteorologiset mittaukset alueelta. Lisäksi Landsat-satelliittiaineistosta johdettiin vuosittaisia normalisoituja kasvillisuusindeksejä vuodesta 1985 jKr vuoteen 2018 jKr, kasvillisuuden muutosten tutkimiseksi viime vuosikymmeninä. Kasvillisuusindeksien kykyä ennustaa maaperän hiilen kertymisen alueellista ja ajallista vaihtelua arvioitiin erikseen.

Kehityssuuntaus pääasiallisesti mineraalipitoisista maaperistä orgaanisiksi maaperiksi havaittiin useissa näytteissä, tämä voi merkitä, että alueilla on käynnistynyt soistumisprosessi. Viimeaikaiset hiilen kertymisnopeudet kasvoivat jokaisella koealalla. Alueen meteorologinen aineisto yhdessä kirjallisuuden kanssa viittasi alueen abioottisten ja bioottisten ympäristötekijöiden yhdessä ilmasto- ja sääolosuhteiden kanssa ohjaavan kertymisprosesseja. Kasvillisuusindeksit osoittivat merkittäviä muutoksia kasvillisuuden rakenteessa ja tuottavuudessa. Viimeaikaisten hiilen kertymisnopeuksien ja kasvillisuusindeksien välisen suhteen arviointi, ei tuottanut luotettavia tuloksia. Maaperän ja ilmakehän välisten hiilivoiden alueellinen ja ajallinen heterogeenisyys tuottaa suuria haasteita tämänhetkisille mallintamismenetelmille. Maaperänäytteiden ja kaukokartoitusaineistojen yhteiskäyttöä tulisi edistää, jotta tulevia muutoksia kyettäisiin mallintamaan tarkemmin.

Avainsanat – Nyckelord – Keywords

Arktinen alue, sammalpeitteinen tundra, hiilen kierto, kaukokartoitus, NDVI, ilmastonmuutos

Säilytyspaikka – Förvaringställe – Where deposited

HELDA - Helsingin yliopiston digitaalinen arkisto

Muita tietoja – Övriga uppgifter – Additional information

Tiedekunta – Fakultet – Faculty	Osasto – Institution – Department
Faculty of Science	Department of Geosciences and Geography

Tekijä – Författare – Author

Mitro Müller

Tutkielman otsikko – Avhandlings titel – Title of thesis

NDVI as a proxy for recent carbon accumulation and greening in Svalbard

Koulutusohjelma ja opintosuunta – Utbildningsprogram och studieinriktning – Programme and study track

Master's programme in geography, Physical geography

Tutkielman taso – Avhandlings nivå – Level of the thesis	Aika – Datum – Date	Sivumäärä – Sidoantal – Number of pages
Master's thesis	07.08.2020	105

Tiivistelmä – Referat – Abstract

A warming trend of annual average surface temperatures since pre-industrial times has been observed globally. High-arctic area of Svalbard, Norway is undergoing amplified change of annual average temperatures when compared to the global average. Decline of glaciers in western Svalbard has been ongoing for several decades, and in the recent past, rapid biological successions have taken place. These changes have likely had effect on regional scale carbon dynamics at Svalbard's moss tundra areas. Possibly indicating onset of paludification process of these areas. However, palaeoecological studies from the area are scarce, and the response of high-latitude moss tundra areas to past or ongoing climate change, are still not fully understood.

This thesis aimed to bring forward information of changes in recent organic matter and carbon accumulation rates at Svalbard, Norway. Soil profiles were collected from four moss tundra sites, located on coastal areas and fjords descending towards Isfjorden, on the western side of Spitsbergen island. Radiocarbon (^{14}C) and lead (^{210}Pb) dating methods with novel age-depth modelling and soil property analyses, were used to reconstruct recent organic matter and carbon accumulation histories from 1900 AD to 2018 AD. Accumulation histories were supported by meteorological measurements from the area. In addition, annual maximum value Normalized Difference Vegetation Indices for 1985 AD till 2018 AD period were produced, to study vegetation succession in the recent past. Lastly, possibility to predict spatiotemporal variation of soil carbon accumulation with satellite derived vegetation indices was assessed.

Development from predominantly mineral soils to organic soils was distinguishable within multiple soil profiles, pointing to potential paludification. Recent apparent carbon accumulation rates showed an increasing trend. Supporting meteorological data and literature suggest that regional abiotic and biotic factors in synergy with weather and climate are contributing to this observed trend. Vegetation indices pointed to major changes in vegetation composition and productivity. However, investigation of relationship between recent carbon accumulation rates and vegetation indices did not produce reliable results. Spatiotemporal heterogeneity of carbon soil-atmosphere fluxes presently imposes large challenges for such modelling. To alleviate this problem, efforts for more efficient synergetic use of field sampling and remote sensing -based material should be undertaken, to improve modelling results.

Avainsanat – Nyckelord – Keywords

Arctic, moss tundra, carbon cycle, remote sensing, NDVI, climate change

Säilytyspaikka – Förvaringställe – Where deposited

University of Helsinki electronic theses library E-thesis/HELDA

Muita tietoja – Övriga uppgifter – Additional information

Table of contents

1. Introduction

Peatlands form significant terrestrial carbon (C) stocks, containing ~20% to ~30% of global soil C pool located within a few meters of soil-atmosphere interface (Loisel et al., 2014; Swindles et al., 2019; Z. Yu et al., 2011). Gross portion of these peatlands lie north of latitude 45°N. Globally a warming trend of mean surface temperatures since pre-industrial times has been observed (Field et al., 2014). Global mean surface temperature, for the years 2006–2015 was 0.87°C higher than the average over the 1850–1900 period (Intergovernmental Panel on Climate Change, 2018). At arctic areas warming is two to three times higher than the global average. Recently, it was proposed that if global mean warming approaches 2°C, respectively, the Arctic (64°N to 90°N) may reach 4°C warming of annual average temperature, and 7°C winter warming (Post et al., 2019). The response of high-latitude organic soils to the climate warming is still unclear. At Svalbard, Norway rapid succession of plant species has taken place in recent past (Nakatsubo et al., 2005; van der Knaap, W.O, 1988; Yoshitake et al., 2011). These changes can be expected to affect C dynamics at Svalbard's moss tundra areas.

United nations set a goal in Paris agreement to limit the global average temperature increase to 1,5ºC above pre-industrial levels, recognizing that this would significantly reduce impacts of climate change (United nations, 2015). Concurrently, France put forth initiative called 4 per 1000 ("4 per 1000" Initiative, 2018). Initiative suggests that annual 0.4% increase in soil C stocks would be enough to stop the rise of carbon dioxide (CO_2) concentration in the atmosphere. It has been estimated that total C stock of northern peatlands is 500 ± 100 Gt (Z. C. Yu, 2012). The greatest source of uncertainty for modern C-stock estimates, is the lack of data, including depth, bulk density, and C accumulation information (Tarnocai et al., 2009). In addition, peat depth and accumulation rates can largely vary within small area; inside individual peatland (Zhang et al., 2018).

Balance of soil organic C stocks are controlled by two principal fluxes (Lund et al., 2010). First, the fixation of C through vegetation photosynthesis, known as gross primary production (GPP). Secondly, the loss of C through ecosystem respiration (ER), that consists of the vegetation and soil respiration. Difference between GPP and ER constitutes net primary production (NPP). Warming climate lengthens the growing season, and likely accelerates organic matter accumulation rates and increases NPP (Gallego-Sala et al., 2018). On the other hand, rising temperature could affect microbial acclimation and the rate of CO_2 and methane (CH_4) production, or advance development

of drier conditions, which could increase of oxidation organic matter (Sihi et al., 2018; Swindles et al., 2019). Thus, imposing contradictory effects to accumulation rates.

Large uncertainties in predictions of climate-induced changes in C dynamics of organic soils still exists (Lara et al., 2018; McLaughlin & Webster, 2014). Estimates can be attained through climate models that simulate atmospheric CO_2 changes (Charman et al., 2013). However, most of these models do not take into consideration climate-related variations in the soil C sequestration rates. Better understanding of factors controlling these soil C fluxes and the role of organic soils in the global C cycle of the past, can be achieved through palaeoenvironmental, palaeoecological and palaeogeochemical studies, relying on stratigraphic sub-sampling of soil profile samples and varying dating methods (Vleeschouwer et al., 2010). Present alteration of peatland C sequestration rates is commonly measured using gas flux chambers and eddy covariance flux towers (McLaughlin & Webster, 2014). These measurements are often used in combination with supporting data sources, to evaluate the C balance of certain area (Alm et al., 2007). When studying vast and remote areas field sampling and measuring methods become laborious quickly and depict circumstances at certain location at a certain point of time (de Paul Obade, 2013). Due to lack of spatially continuous measurements, demand for supporting data sources increases.

In the late 1970's use of photographic infrared and red linear combinations for monitoring vegetation biomass and physiological status were studied (Rouse et al., 1974; Tucker, 1979). It was observed that infrared/red ratio -vegetation indices, were sensitive to photosynthetically active biomass. Best known of those indices, is normalized difference vegetation index (NDVI). NDVI is seen as indicator for fraction of photosynthetically active radiation absorbed by vegetation (fPAR) and is widely used as a proxy for plant biomass and vegetation productivity (Santin-Janin et al., 2009). Changes in NDVI values recorded by satellite platforms from arctic and boreal areas indicate that northern ecosystems are experiencing rapid ecological change in response to climate warming (McPartland et al., 2019). These observations have been linked with changes in community composition and leaf area indices.

Landsat satellite-mission image archive provides record with unmatched value for monitoring global land cover and ecological change (Wulder et al., 2012). However, at high-latitude areas, large portion of Landsat record imagery does not meet the quality criteria to support time-series analysis (Dwyer, 2019). These images fall back to lower processing level categories. Thus, ruling out direct use of Landsat record in timeseries studies at these areas. This factor complicates monitoring of long-term land cover changes at Svalbard.

2. Theoretical Background

2.1 Organic soils, peat formation and carbon dynamics

Soil can be defined as a mixture of minerals, living organisms, and decaying organic matter, located between base rock, atmosphere, and vegetation (Kutsch et al., 2010). Soils store substances that are essential to ecosystem processes and enable multitude of biogeochemical transformation and transfer processes. C content is often especially high in soils with high organic matter content, located in wet and cold environments (Jobbágy & Jackson, 2000). These terrestrial C pools interact with atmospheric composition, climate, and land cover change. Thus, ability to assess and predict climate changes influence on these C pools, calls for better understanding of the distributions and controls of these soil C pools, and how they relate to changes in surface vegetation composition.

United States Department of Agriculture's definition of organic soil material relies on the period of annual water saturation (Soil Survey Staff, 1999). Soils saturated for less than 30 days (cumulative) per year in normal years, must contain more than 20 percent (by weight) organic C. If soil is saturated for 30 days or more cumulative in normal years, a three-class definition is used. If mineral fraction contains over 60% clay, over 18% must be of organic matter. Secondly, if mineral fraction contains no clay, over 12 % must be of organic matter. Thirdly, if mineral fraction contains less than 60 % of clay, over 12 + (clay percentage multiplied by 0.1) percentage must be of organic matter. Although peat is formed by organic matter, it also contains small amount of mineral matter (Rydin et al., 2006). Minerals are present as bound components in the organic matter and as free minerals in the peat matrix. Current classification systems regarding peat, often use percentage of organic matter as the only parameter (Joosten & Clarke, 2002; Andrejko et al., 1983; Landva et al., 1983). Geological definition requires 30-centimetre thick profile of accumulated organic matter before the soil is classified as peat (Herranen, 2009).

Despite classification standards, required environmental conditions and elementary processes for peat formation, have been extensively studied for decades. Peat formation requires anaerobic conditions resulting from near continuous soil saturation, where ecosystems GPP exceeds ER (Moore, 1987). Hence, occurrence of peatlands is often geographically associated to areas with fresh water and cool climate (Z. Yu et al., 2011). ER consists the efflux of C from the ecosystem as CO_2 and CH_4 to the atmosphere, including the aboveground plant respiration and soil respiration (Barba et al., 2018).

Soil respiration is a measure of decomposition rate of organic material in the soil (Kutsch, W. et al., 2010). It consists of two main components, 'autotrophic' and 'heterotrophic' respiration (Figure 1). The autotrophic component can be further separated into respiration of the roots and their mycorrhizal symbionts and the microbiota of the rhizosphere. Heterotrophic component is due to soil micro-organisms that decompose the organic materials from above-ground and belowground litter. Decomposition rate in the oxygen-rich surface layer (acrotelm) of a profile is greater than in water-saturated layer (catotelm) (Clymo, 1965; Moore, 1987). Efflux from aerobic decay releases CO_2. Anaerobic microbial decay occurs more slowly, and efflux mainly as CH_4. Part of the CH_4 produced in the catotelm is consumed by methanotrophic bacteria in the acrotelm (Lai, 2009). In addition, compounds which can be used by heterotrophic decomposers are produced. Large spatial and temporal variation in these respiration rates are common.

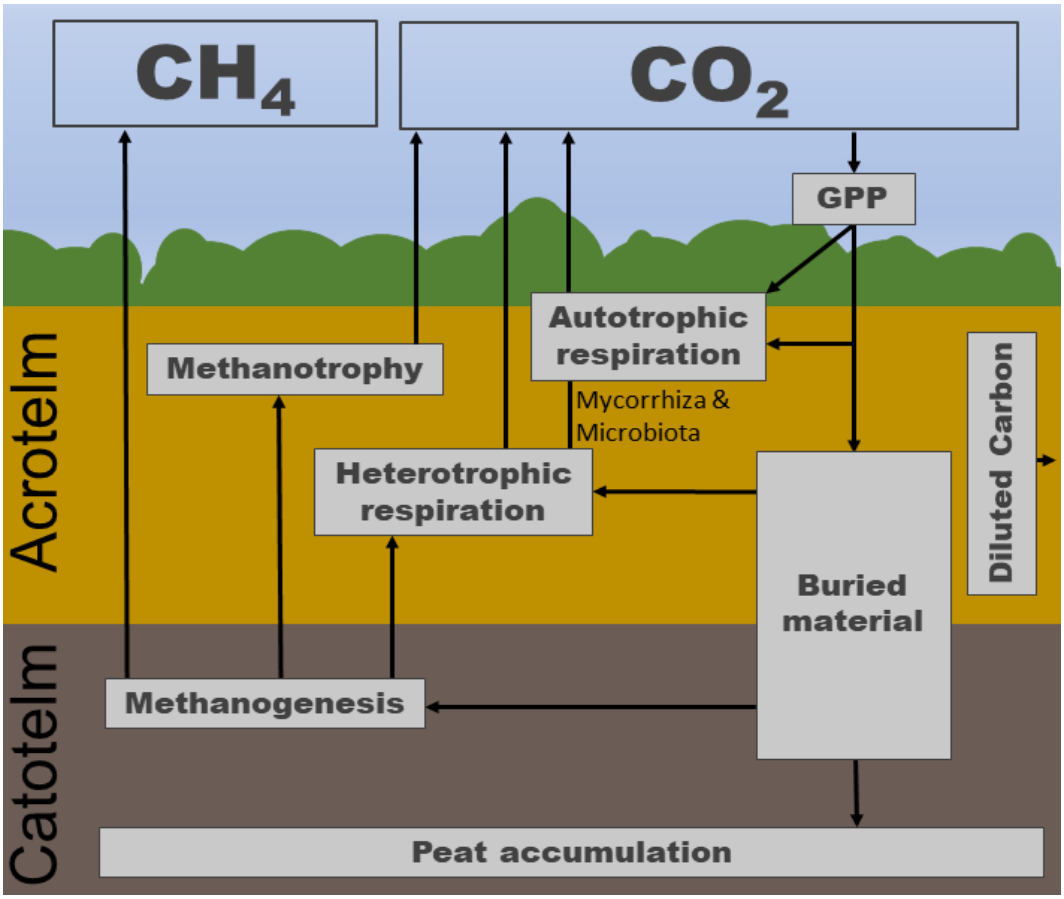

Figure 1. Simplified carbon dynamics of peatlands. Gross primary production (GPP) produces influx of carbon (C) to the system. Part of C is utilized in plant metabolism, producing outflux of C via autotrophic respiration. Respiration takes place at above (leaves and stems) and below ground (roots) parts of the plants. In time, portion of the organic matter produced gets buried. Buried material is either deposited as peat or decomposed by heterotrophic respiration. Decomposing in aerated acrotelm layer produces carbon dioxide (CO_2) and methane (CH_4) in unaerated catotelm. Part of the produced CH_4 is used by methanotrophic bacteria and additional compounds are produced that can be used by heterotrophic decomposers. Portion of C is exported in diluted form with outflowing water. (Figure modified from Lees et al. (2018))

Peatlands are mostly located at boreal and subarctic regions and extensive development has been detected at western Siberia, central Canada, north western Europe, and Alaska (Z. Yu et al., 2011). Peatlands north of 45°N have accumulated ~500 gigatons of C mostly during the Holocene (Loisel et al., 2014). However, plant growth at arctic climate conditions is very limited and peat formation is not common (Clymo R.S., 1998). Still, Arctic plays an important role in the global C dynamics. It has been a sink for atmospheric CO_2 (0 to 0.8 Pg. C yr^{-1}) during recent decades (McGuire et al., 2009). Simultaneously, acting as a substantial source of CH_4 to the atmosphere (32 to 112 Tg. CH_4 yr^{-1}), primarily because large areas covered by wetlands. Large spatiotemporal variations in C accumulation rates of arctic peatlands have been observed, both at local and regional scales (Zhang et al., 2018). Nevertheless, evidence of paleoenvironmental studies shows higher accumulation rates during past warmer climate phases (Charman et al., 2013; Z. Yu et al., 2011). Data of those studies is mostly collected from boreal area, leading to uncertainties of the impacts of rising temperature to the arctic areas. Another source of increasing uncertainty is the number of interconnected ecosystem components controlling the C accumulation rates.

In addition to soil respiration rates, NPP is a significant component affecting the accumulation rates. NPP is closely linked to the length of the growing season and cumulative photosynthetically active radiation during the growing season (Gallego-Sala et al., 2018; Loisel et al., 2014; Piilo et al., 2019). Thus, predictions of increase in C accumulation rates in a warming climate are reasonable. As a whole, dynamics governing the accumulation rates are much more complex. Multiple factors impact alteration in cohesion with temperature, for instance peat composition soil hydrology and presence of permafrost (Klein et al., 2013; Z. C. Yu, 2012).

Peat composition (organic matter content and C/N mass ratios) is directly linked to the type of vegetation covering the soil (Wang et al., 2015). Thus, composition of parent material also affects the rate of C accumulation. Then again vegetation type and soil hydrology are strongly connected. It has been suggested that alteration of water table depth affects peatland accumulation rates non-linearly, as both too shallow (wet conditions) and too deep (dry conditions) water table level hampers litter production (Rennermalm et al., 2010). Decomposition rates are highly influenced by the degree of soil water saturation. In addition, water availability together with atmospheric acid deposition strongly controls the rate of C being dissolved, while hydrological processes govern exportation (Xu et al., 2020). At arctic areas permafrost has restrained exportation dissolved C (Ma et al., 2019).

Permafrost depicts subsurface earth materials that remain below 0 °C for two or more consecutive years (Boike et al., 2018). Gross portion permafrost areas are in the Arctic, where organic C remain stored in a frozen form. Warming of Arctic may further permafrost thawing, making these areas important components of the global climate system. Permafrost and its thawing rates can also alter C budgets by creating drier or wetter conditions (McLaughlin & Webster, 2014). Wetter conditions can lead to rise of the water table level, slowing down decomposition rates, but enhancing CH_4 emissions. Drier conditions lead to lower water table levels, enabling increase in biomass at surface but also higher quantity of peat is now exposed to aerated conditions, enabling aerated decomposition of peat and higher CO_2 emissions.

In conclusion, peatland NPP and C balance are mostly defined by GPP and ER, as large component of C fluxes in terrestrial ecosystems takes place in gaseous form (Alm et al., 2007). Nevertheless, multiple factors with direct and indirect pathways impact GPP and ER rates. Thus, reliable C balance estimates often require multi-source data.

2.2 Factors contributing to vegetation dynamics

Large-scale spatiotemporal variations in C accumulation rates are controlled by regional and local environmental conditions. Variations in characteristic and processes typical to the area can have significant effects to soil formation and vegetation dynamics in general. Harsh arctic climate conditions and low availability of nutrients are limiting factors for vegetation development at Svalbard (Gąsiorowski, 2019). Thus, processes affecting sediment supply, hydrological conditions, and nutrient distributions in the landscape, could have strong impacts to plant nutrient supply and development.

Arctic is warming faster than anywhere else on Earth, impacts of this can be seen in Glacier dynamics of Svalbard. Holocene maximum glacier extent was reached during the “Little ice age”, that started with ice advancement in the 13^{th} or 14^{th} century (Svendsen & Mangerud, 1997). Cold climate phase of “Little ice age” prevailed at Svalbard between 1500 and 1900 AD (Yang et al., 2020). Svalbard is a low mass-balance-gradient glacial environment (accumulation and ablation rates altitudinal variation across the glacier is minor), with mostly temperate glaciers (Hodgkins, 1997). Temperate glaciers are entirely at the melting temperature, except transiently cooling surface layer during winter. Only at perennial basis glaciers at high elevations can be defined non-temperate. Decline of glaciers

in western Svalbard, where our study are resigns, has been ongoing for several decades (Bourgeois et al., 2016).

Glaciers are sensitive to climate shifts and these effects are often seen in the variation of rock-flour production (van der Bilt et al., 2015). As glaciers mechanically grind rock beneath them, rock-flour is produced, through this glacial erosion. Meltwater flushes suspended sediments downstream with runoff water, enhancing sediment deposition at lowlands and changing the hydrological environment. Fine grainsized rock flour has a high reactivity and may therefore help to rejuvenate nutrient poor soils and provide nutrients to plants (Gunnarsen et al., 2019). Thus, proglacial areas, located in front of glaciers are strongly influenced by these fluxes of water and sediment (Hodgkins et al., 2009). Also, glacial retreat leads to expansion of new habitats for fauna and flora of the area.

Despite the limited number of large herbivores, Svalbard's vegetation is strongly affected by fauna. Dating results have indicated occurrence of reindeer at Svalbard over 5000 years ago and sea bird colonization at Svalbard over 9000 years ago (Yuan et al., 2010; van der Knaap, 1989). Svalbard reindeer (*R. t. platyrhynchus*) colonize nearly all non-glaciated land area (Le Moullec et al., 2019). Grazing pressure and fertilizing effects of reindeer faecal pellet have been presumed to affect productivity of tundra vegetation (Albon et al., 2017; Sundqvist et al., 2019). As accumulation of reindeer faecal pellets can have fertilizing affects, so does excrement of seabirds. Via seabird excrements marine bio-elements are transported to land. Areas located under bird colonies present exceptions to otherwise nutrient poor soils (Gąsiorowski, 2019). Nutrients from bird excrement are washed out from the colonies by precipitation, fertilizing areas affected by runoff. Important herbivore bird species at Svalbard are Svalbard rock ptarmigan (*Lagopus muta hyperborean*) and migratory geese species (pink-footed (*Anser brachyrhynchus*), barnacle (*Branta leucopsis*) and Brent goose (*Branta bernicla*)) (Descamps et al., 2017). Predatory bird species are glaucous gull (*Larus hyperboreus*) and skua spp..

In conclusion, external abiotic and biotic factors typical to Svalbard, most likely have an impact on soil and vegetation dynamics. Melt waters from the glaciers affect regional sediment supply, hydrological conditions, and nutrient distributions. Also, fauna of the area impact vegetation productivity. Grazing reindeers use ground vegetation as nutrition, and simultaneously shape insulation capabilities of mosses covering the soil and their excrement offers nitrogen (N) fertilization. Even stronger variation in soil nutrient availability is caused by large seabird colonies Areas located under cliffs with large bird colonies likely have much better nutrient availability.

2.3. Normalized difference vegetation index

NDVI is widely used as a proxy for plant biomass and vegetation productivity, also known as a "greenness index" (Santin-Janin et al., 2009; Vogelmann et al., 2012). Index is based upon the observation, that by measuring red and near infrared (NIR) wavelengths of electromagnetic spectrum, and calculating ratio between these wavelengths, an index sensitive to photosynthetically active vegetation is produced (Rouse et al., 1974; Tucker, 1979). Chlorophyll of healthy green plants absorb more light in the red wavelength and due to plant cell structure, higher reflection characteristics are recorded in the NIR wavelength (Nouri et al., 2017). Thus, high index values are recorded in areas that have dense coverage of photosynthetically active vegetation. NDVI can be calculated by equation:

$$NDVI = (NIR - red) / (NIR + red)$$

Index values vary between -1 to +1 (Nouri et al., 2017). Negative values are recorded from areas covered by clouds, water or snow (Figure 2). Values close to zero primarily depict rocks or bare soil. Usually shrubs and meadows return values ranging between 0.2 to 0.3, while values above 0.6 often indicate forest or other highly dense vegetation. At arctic areas where moss communities constitute most of the understory, interpretation of NDVI values is more challenging.

Compared to vascular plants moisture content of mosses can vary more widely and rapidly (Hajek & Beckett, 2007). Many species show abilities to recover even after extreme desiccation. Nevertheless, drying affects photosynthetic activity of mosses negatively. Yet, optimal water content for peak photosynthetic rate does not necessarily occur at full saturation (Harris, 2008). Experimental study noted that as moisture content of sphagnum moss communities (*Spaghnum augustifolium* and *Spaghnum capilliofilium*) declined from 80% to 70%, recorded NDVI index value reduced by 0.17 to 0.2 (May et al., 2018). Respectively, with pleurocarpus moss communities (*Hylocomium splendens, Aulocmnium spp* and *Polytichum spp.)* NDVI index value reduced by 0.06 to 0.12. Thus, short term changes in moisture conditions can considerably affect NDVI values recorded at areas where mosses cover the ground.

As multiple variables can affect calculation of NDVI negatively, ways to reduce uncertainties have been developed. Appropriate order and pre-processing steps of optical remote sensing data provides necessary foundation to prepare data for ecological analyses (Young et al., 2017). When spectral values are being compared across images from multiple time-windows, imagery should be pre-

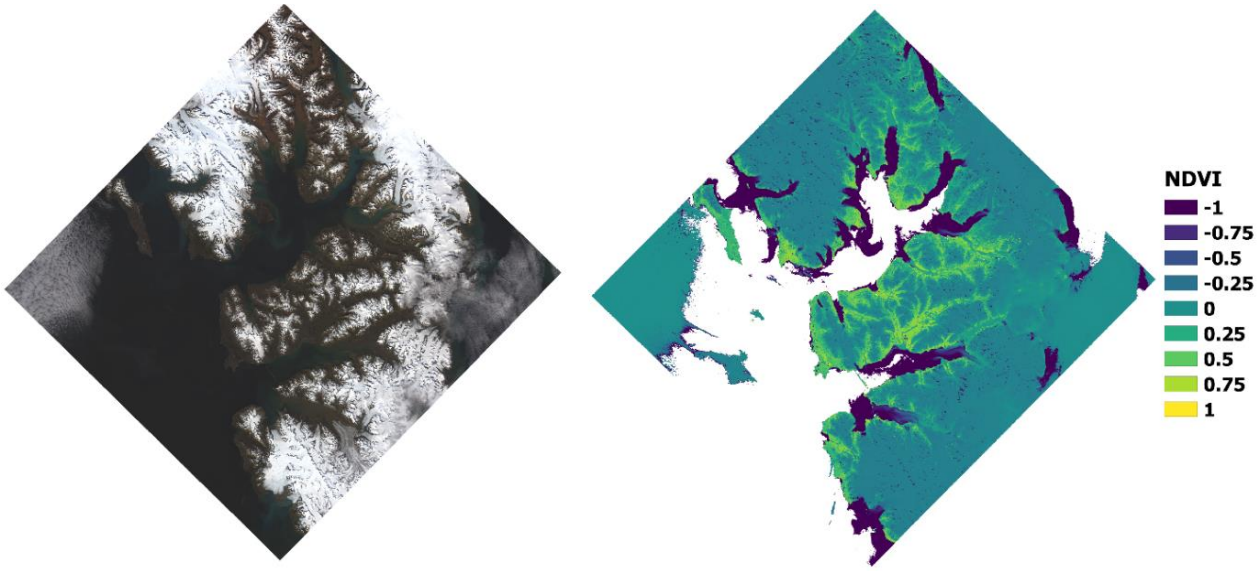

Figure 2. Landsat 8 acquisition (LC08214004201407150 1T1) presented as red, green and blue- (RGB) and as NDVI-image. RGB-composite on the left was composed from the bands 4, 3 & 2. On the right side NDVI-image is calculated using near infrared and red channels (bands 5 & 4). Before the calculation, pixel values out of valid range were set to NA (blank pixel at sea areas). Areas with glaciers clearly distinguishable in the RGB image, have NDVI values close to 0. High NDVI values can be seen at the vegetated valley areas.

processed either to surface reflectance or to relative values to ensure comparability. Clouds, cloud shadows, and snow can significantly influence the spectral bands of optical sensors (Zhu et al., 2015). Their presence can cause serious problems in calculation of vegetation indices and especially in change detection. Compositing images from known time periods (i.e. mean, median and maximum value calculation over all images of period), can reduce effects of short term variations due to cloud cover and moisture conditions, which is desirable when studying long-term changes of landcover using NDVI time-series (Baniya et al., 2018; Chen et al., 2003; Fassnacht et al., 2019; Vickers et al., 2016; Zhou et al., 2001).

Terrestrial C cycle models often require information on photosynthetically active radiation incident on the vegetation, fPAR, and conversion efficiency of absorbed energy (Jung, 2008; Monteith, 1977; Scholze et al., 2017). Spatiotemporal modelling requires parameterization of the land surface, which is only possible using remote sensing (Hilker et al., 2008). NDVI can be seen as representation of the fPAR, as it indicates distribution of leaf area and chlorophyll amount (Lees et al., 2018). Therefore, it has been used also as a proxy when estimating GPP within the spatiotemporal C models. Still, it is good to acknowledge that NDVI indicates “greenness” of the vegetation, not the actual photosynthesis.

3. Research questions

This Master's thesis was brought forth as a part of a larger research project studying response of high-latitude peatlands and organic soils to past and recent warming. Classical biogeography's view suggest that ecosystems are strongly governed by climatic constrains regarding their structure and functions (Reichstein et al. 2014). My research hypotheses are that global climate change has affected environmental conditions at Svalbard's moss tundra areas, altering their C dynamics. Secondly, history of these changes can be reconstructed from soil profile segments by dating methods supplemented with soil property analyses. Furthermore, these changes are partly caused by increase in vegetation productivity, which can be detected with using NDVI time series.

Presently only a limited number of palaeoenvironmental studies concerning soil C cycles from Svalbard exists (Nakatsubo et al., 2015; J. Rozema et al., 2006; van der Knaap, W.O, 1988; Wojcik et al., 2019). As global warming likely affects the mass balance of C near soil surfaces, where surface temperatures fluctuate with air temperature, it is important to focus research efforts on C cycling of recently accumulated soil (Turetsky et al., 2004). Here palaeoenvironmental methods and remote sensing-based vegetation indices are combined, to study recent changes in soil properties and soil C accumulation rates at four study sites. Thesis investigates following research questions:

- Have organic matter and carbon accumulation rates of Svalbard's moss tundra areas changed during the recent past? If so, when and why?
- Do changes in the recent organic matter and carbon accumulation rates reflect changes in the weather history of the study area?
- Can Landsat data from the study area be used to monitor changes of vegetation composition, and to detect spatiotemporal variation of recent carbon accumulation rates?

Organic matter and C accumulation histories are reconstructed using dating methods supplemented with soil property analyses. In terms of environmental drivers, meteorological measurements are emphasised, other factors potentially contributing to changes in accumulation rates are assessed through literature. Landsat derived NDVI indices may enable monitoring of changes in vegetation composition and productivity, at wide areas with medium spatial resolution. If proven that Landsat derived NDVI data offers a proxy for soil C accumulation, valuable spatiotemporal information of high-latitude moss tundra and peatland areas' accumulation histories covering multiple decades could be derived.

4. Study area

Svalbard is an archipelago of Norway. Study area is located at the largest island of the archipelago, Spitsbergen. Terrain of Spitsbergen is mountainous, and large portion of the island is covered by glaciers. Long-term presence of glaciers can be seen in the island's topography, as it is deeply carved by fjords. All study sites surround Isfjord, located at latitude 78.3°N and longitude 15.0°E. Study area consists of four different moss dominated tundra areas, which are Alkehornet, Colesdalen, Björndalen and Bolterdalen (Figure 3).

Sites where chosen as they have other active study and monitoring efforts already established (Christensen et al., 2020; COAT, 2020). Alkehornet is only site situated at the northern shore of Isfjord, on a small headland (Figure 4). Soil mass movements induced likely by gelifluction and cracking of peat are common at the slopes of Alkehornet. Coring points at Alkehornet were chosen so, that no alteration in soil due to gelifluction or peat cracking was noticeable near these points (Table 1). Rest of the sites are situated at valleys, descending to southern shores of Isfjord. Varying erosion and accumulation patterns of sediments could be seen at bottom of the valleys. Colesdalen -valley has the warmest microclimate of the four sites. River Coleselva runs at its bottom flowing towards Isfjord. Björndalen is small valley close to the shoreline. Bottom of the valley is flat, with streams flowing from Håberg -glacier towards Isfjord. Bolterdalen is a valley with a small river running on the bottom. Valley descends to a larger Adventdalen -valley, where Longyearbyen, the largest settlement of Svalbard resides.

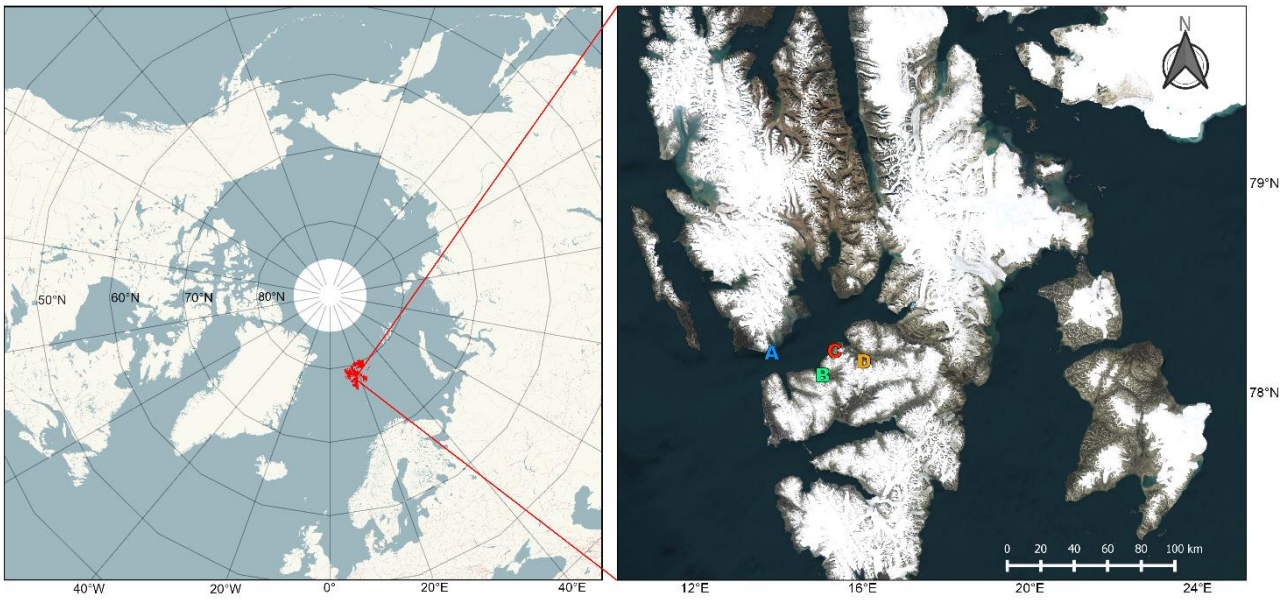

Figure 3. Left panel presents the location of archipelago of Svalbard at the Northern hemisphere. Right panel presents locations of study sites at the island of Spitsbergen, Svalbard. Sites are presented by alphabets running from west to east (Alkehornet = A, Colesdalen = B, Björndalen = C and Bolterdalen = D).

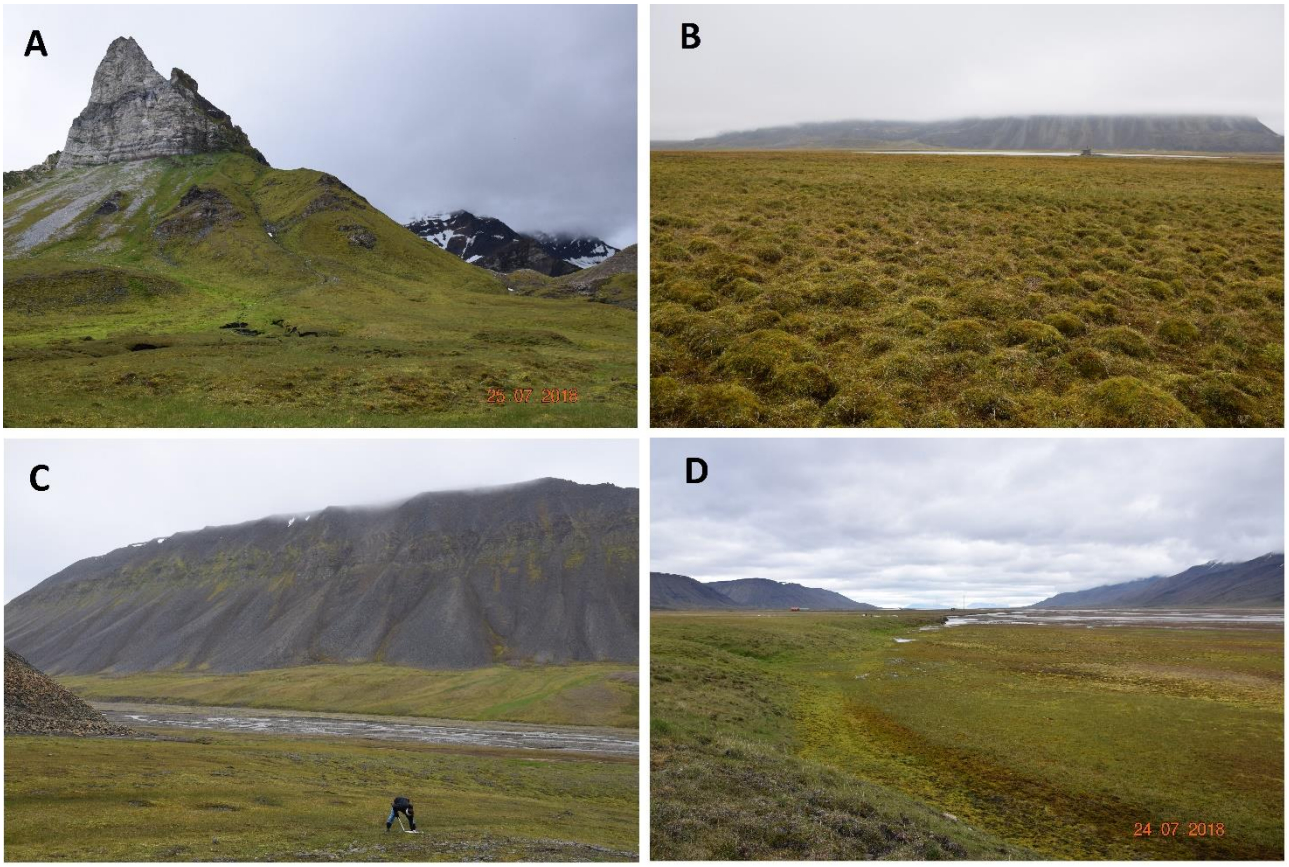

Figure 4. Photograph of each study site presented above (© Piilo, 2018). ***Photo-A*** *shows landscape characteristic to Alkehornet. Steep cliffs dominate the landscape, with distinct mass movements down the slopes. Low lying areas have wet soils with large quanties of moss plants growing.* ***Photo-B*** *shows hummocky vegetation covering the field layer of Colesdalen -valley. In the background flows Coleselva -river and behind it steep slopes surrounding the valley ascend.* ***Photo-C*** *is taken from the bottom of Björndalen valley. Flowing meltwater streams run through otherwise flat floor of the valley.* ***Photo-D*** *is taken from Bolterdalen. Left side of the photo shows rather dry herbaceous moss tundra typical to the area. On the right, area with wetter depression is shown. These environments alternate within the valley.*

Due to arctic climate, productivity of terrestrial ecosystems is limited, thus leading to thins soils (Gąsiorowski, 2019). This sets limitations to development of vascular plants. Therefore, paludified soils composed of bryophytes are the most widespread type of vegetation at arctic areas. Description of vegetation types of the study sites differs, depending on the source. Elvebakk A. (2005) classified Alkehornet as a circumneutral tundra characterized by *Luzula nivalis* and rest of the sites as *Cassiope tetragona* tundra. In more recent digital vegetation maps, pixelwise classifications of the sites consists pixel values representing wet moss tundra, swamps or mires, bird cliff vegetation and *Cassiope tetragona* heaths (B. E. Johansen et al., 2012; Norwegian Polar Institute, 2020). Also, on finer spatial scale variation in the tundra landscape of Svalbard, snow cover duration, efficiently determines the landscape-scale distribution of arctic and alpine plants (Cooper et al., 2011).

Table 1. In situ measurements per coring point. Coordinates are as decimal degrees. Elevation is presented as meters above sea level. Water table depth is centimetres from soil surface. pH at accuracy of 0.5

Site	Core id	Coordinates	Elevation	WTD	pH
Alkehornet	Alk.1	78.215, 13.826	67	NA	6
Alkehornet	Alk.3	78.214, 13.828	29	NA	4.5
Alkehornet	Alk.4	78.214, 13.831	26	NA	5
Alkehornet	Alk.5	78.214, 13.827	38	10	5.5
Alkehornet	Alk.7	78.213, 13.830	23	NA	4.5
Björndalen	Bj.1	78.224, 15.331	23	6	5
Björndalen	Bj.2	78.224, 15.328	30	8	5
Björndalen	Bj.3	78.223, 15.328	29	6	5
Bolterdalen	Bo.1	78.172, 16.034	34	NA	5
Bolterdalen	Bo.3	78.172, 16.033	29	NA	5
Bolterdalen	Bo.4	78.172, 16.034	29	8	5
Bolterdalen	Bo.6	78.173, 16.030	20	NA	5
Colesdalen	Col.1	78.108, 15.044	11	NA	5
Colesdalen	Col.2	78.108, 15.043	11	32	5
Colesdalen	Col.4	78.104, 15.049	NA	NA	5

In situ observations proved that species composition at all the sites is highly uniform. Vegetation at the sites can be described as herbaceous moss tundra. Prevailing species were identified (Table 2). Notable observations altering from general trend of the sites were scarce *Sphagnum* species observations at Björndalen and Colesdalen. At Björndalen patches with *Sphagnum squarrosum* were observed. Two different Sphagnum species were observed at Colesdalen (*Sphagnum fuscum* and *Spaghnum squarrosum*). However, the abundancies were very minor.

Table 2. Taxa recorded in the proximity of coring sites.

SPECIES
Tomentypnum nitens
Aulacomnium palustre
Sanionia uncinata
Equisetum arvense spp.
alpestre
Salix polaris
Bistorta vivipara
Petasites frigidus
Dupontia fisheri
Dryas octopetala
Saxiafraga hirculus
Eriopohorum scheuchzeri
Cassiope tetragona
Poa alpina
Deschampsia alpina

Reindeer faecal pellets were found abundantly at every study site, which implies that grazing of reindeer packs occurs at all the sites. No estimates of quantity of individuals grazing at the sites, or differences between the sites are available. Large-scale declination of moss or vascular plant cover, due to grazing was not noted. Large bird colonies inhabit the cliffs ascending over Alkehornet study sites. No large bird colonies were noted near the other three sites.

5. Material

Field samples were collected, and measurements recorded between the dates of 24.7.2018 and 29.7.2018. Remote sensing data and historical weather data were collected during autumn of 2019 and spring of 2020. In this chapter these datasets are individually presented.

5.1 Soil samples

Each sampling point was individualized with an id-code and exact coordinates and elevation information were saved using a GNSS receiver. Plant species covering the soil in a near proximity of the sampling points were identified to general level; no species-specific identification was done. Information on water table depth, pH and other individual traits of the site were reported. Total of 22 soil profiles were collected during the field work period. In this thesis, 15 of those samples are studied. Samples were chosen so, that they form a representative sample of every study area.

5.2 Digital surface model

Version 3.0 Digital surface model (DSM) tiles with spatial resolution of 10 meters, were downloaded from ArcticDEM server (Porter et al., 2018). ArcticDEM project provides automatically produced high-resolution, high quality, DSM of the Arctic. Data is constructed from in-track and cross-track high-resolution (~0.5 meter) imagery acquired by the DigitalGlobe constellation of optical imaging satellites. DSM are assembled from these images by using optical stereo imagery, high-performance computing, and open source photogrammetry software. To cover all the area surrounding Isfjord, four tiles all in all were downloaded. Grid id values of downloaded tiles are 34_51_10m, 35_51_10m, 34_52_10m and 35_52_10m.

5.3 Landsat data

To be able to detect temporal changes within a time frame, comparable to C accumulation data derived from dated soil sections, large image collections spanning over decades are required. In addition, requirements for spatial and temporal resolution are present. To detect land cover changes in the near proximity of the coring points, high enough spatial resolution is required. In the High Arctic, snow cover melts usually in June, and plant senescence starts in early August (Cooper et al., 2011). Thus, the growing season is very short, though strong interannual variation takes place. This

sets requirements to temporal resolution, especially at areas where imaging is often hampered by cloudiness. Here Landsat data were used to meet these requirements.

Landsat data were ordered via Earth Explorer, user interface for online search and orders (United States Geological Survey, 2019a). Data query was filtered by sensor, data processing level and to touch only summer months (June, July and August). Landsat 5, 7 and 8 -satellite missions' data (Collection 1 processed to Level-2 –state) were selected and ordered (only available on-demand) (Dwyer, 2019; United States Geological Survey, 2019c, 2019b). Products generated from Landsat 5, 7 and 8 sensors all share 30-meter spatial resolution on a Universal Transverse Mercator or Polar Stereographic mapping grid. This enables pixelwise change detection between products. Bulk downloading of the ordered and processed data were carried out with python based espa-bulk-downloader (appendix A) (*USGS-EROS/Espa-Bulk-Downloader*, 2015/2020).

Level-2 products are processed to surface reflectance. Surface reflectance measures the fraction of incoming solar radiation reflected from Earth's surface to the Landsat sensor (United States Geological Survey, n.d.-b). Surface reflectance products improve comparison between multiple images over the same region. This is due to processing steps accounting for atmospheric effects such as aerosol scattering and thin clouds, which can help in the detection and characterization of Earth surface change. Surface reflectance products are assigned to certain collections based upon their quality assessment. Tier-1 data is processed to Precision and Terrain corrected products (L1TP) with image-to-image registration to the Global Land Survey control of ≤12-meter radial root mean square error (Dwyer, 2019). If his registration threshold is not met, data is processed either to Systematic and Terrain Corrected products (L1GT) or to systematically corrected (L1GS). L1TP data is radiometrically calibrated and orthorectified using ground control points and DSM to correct for relief displacement. L1GT data is radiometrically calibrated and systematic geometric corrections applied using the satellites ephemeris data and DSM to correct for relief displacement. L1GS data is radiometrically calibrated with only systematic corrections applied using satellite ephemeris data. Only L1TP data is suitable for pixel-level time series analysis as it is.

Availability of images was largely limited because high level of cloudiness in the study area. Due to cloud coverage in every image, no images were downloaded from the years 1997, 2003 and 2007. In total 94 images were downloaded, placing between the years 1985 to 2018. Image pool consisted 30 of Landsat 8 images (L1TP products), 27 Landsat 7 images (L1GT products) and 37 Landsat 5 images (L1GS products). These images were filed in folders, per sensor name and the image coverage area.

Image coverage is described by Worldwide Reference System 2 (WRS2) -scene code (Masek, 2020). WRS-2 is a global notation system for Landsat data. It specifies a nominal scene centre designated by path and row numbers. Downloaded data originated from 11 individual WRS-2 scenes.

5.4 Weather data

Measured weather data was downloaded, in attempt to evaluate climate trends at Isfjord area during the 1900 AD to 2018 AD period. Data recorded at Longyearbyen station covers the period from 1917 to 1976 (station ended operating at 1977). Data recorded at Svalbard airport covers the period 1977 to 2018. Airport is located at the shore of Isfjord, 28 meters above the sea level, residing near Longyearbyen, the administrative centre of Svalbard.

Annual mean air temperatures from Longyearbyen area are available from 1898 onwards (Norwegian Meteorological Institute, 2020a). Secondly, seasonal mean temperature dataset includes annual average temperatures separately for winter, spring, summer, and autumn months (Norwegian Meteorological Institute, 2020c). For some years, the data is missing. Variation in ice condition strongly affects the temperature in Svalbard, leading to large interannual variations. Therefore, in the seasonal data variations on time scales shorter than 10 years have been smoothed. Dataset of annual total precipitation at Svalbard airport was downloaded (Norwegian Meteorological Institute, 2020b). Precipitation measurements are available from the year 1915 till present. Data regarding monthly sum of the effective temperature during the growing season was downloaded (temperature sum accumulates if the daily mean temperature exceeds 5 ºC. Portion of the daily mean temperature that exceeds 5ºC, is then added to the monthly sum. This dataset was compiled using daily mean temperature averaged from multiple measurement stations around Svalbard) (Norwegian Meteorological Institute, 2020d). From these monthly sum values, annual sum values of the effective temperature were derived.

6. Methods

This study is primary based on in-situ collected soil samples and downloaded remote sensing data. To support these datasets measured weather data were downloaded as well. First, methods used to study soil samples are described. Secondly, methods used to study remote sensing data are described.

6.1. Soil profile sample coring and storing

Soil profiles were collected using box auger, until reaching the mineral soil or ice. Samples were wrapped in plastic and transported to laboratory in sealed PVC tubes. Individual id codes were determined for each profile (first three letters of the site and then running number). At Alkehornet site mineral soil was reached only with Alk.1 soil profile. Bottom layers of other cores from Alkehornet were frozen, preventing sampling from deeper layers. At other sites mineral soil was reached with every core. While still in Svalbard all samples were stored in a freezer (-80 °C) for more than 40 hours. This was a precaution to prevent possible spreading of Ecinococcus parasite to Finland. Then samples were transported to University of Helsinki, Finland, where the samples were stored in a freezer.

For analyse purposes, cores were defrosted and subsampled into 1-cm thick slices. Outermost layer of the core was discarded to avoid any contamination. Slicing was carried out either by knife or sharp set of scissors. To avoid contamination equipment was cleaned between every subsampling operation. Subsamples were named by their stratigraphic position within the core and stored into sealed plastic bags. Sample from topmost centimetre (0-1 cm) was named 1. Naming id was then continuously increased as sample-depth increased.

6.2 Bulk density

To enable C accumulation analyses, sample bulk density was calculated for every subsample. (Chambers et al., 2011). First, plastic containers with volume of 5 cm^3 were weighted. From every soil subsample 5 cm^3 volumetric sample was extracted into a weighted plastic container with a pair of tweezers. Container was filled with intent not to compress the sample by pressing down on it but at the same time avoiding leaving air pockets. Container was sealed with parafilm perforated by needle. This protects the samples but enables moisture to efflux. Then samples were refrozen, and freeze-dried. Dried samples were weighed, and the weight of the plastic container was subtracted. Finally, bulk density was calculated by dividing dry peat weight by wet peat volume (g/cm^3).

6.3 Organic material, carbon and nitrogen content

From every subsample portion of organic material was separated and loss on ignition (LOI) measurements conducted (Heiri et al., 2001). Sample crucibles were cleaned, dried, and weighed before setting samples in. Crucible and the sample were then weighted together. Samples were kept in furnace with a temperature of 550 °C for four hours. Crucibles were set to cool down in a desiccator. Then crucibles with burnt material were re-weighted, considering weight of the crucible itself. Weight of sample material left, presents the mineral material, after the organic material has burnt away. From the weight lost in ignition, proportion of organic matter in the sample was defined.

C/N content measurements were performed at four-centimetre intervals for nine of the cores (Alk.3, Alk.4, Alk.7, Bj.1, Bj.3, Bo.3, Bo.4, Col.1 and Col.2). Analysis requires sample weight of only 0.015g. Thus, small fraction of the dried samples was ground using a mortar. C and N content was measured from sub-samples using LECO TruSpec Elemental Determinator at the University of Helsinki, Finland. From these results site-specific average C content was calculated. This average C value was used for the six profiles for which C analyses were not carried out.

6.4 Radiocarbon ^{14}C and lead ^{210}Pb dating

Chronologies were composed by dating subsamples either with radiocarbon (^{14}C) accelerator mass spectrometry or lead (^{210}Pb) dating methods. Radiocarbon dating was used in particularly to date profile bottom layers with high organic content. Lowest subsample segment presumed as organic soil was determined by visual inspection. For radiocarbon dating plant macrofossils were collected from the inner parts of the lowest subsample to avoid contamination with modern C. Sampling equipment was kept clean to mitigate possibilities of contamination. Dating itself was conducted in two parts. Nine of the bottom samples were sent to Poznan Radiocarbon Laboratory (Poznan, Poland). Later, six more bottom samples and one additional segment from middle of Alk.4 profile were sent to Finnish Museum of Natural History (LUOMUS, Helsinki, Finland).

Accelerator mass spectrometry radiocarbon dating can be used to reliably date < 50 000 old material (Piotrowska et al., 2011). The ^{14}C isotope is produced in upper atmosphere, through nuclear reactions between thermal neutrons and N nuclei. Plants assimilate CO_2 and simultaneously ^{14}C through photosynthesis. As the plant dies, no further radiocarbon is assimilated, and previously assimilated radiocarbon begins to decay. ^{14}C decays back to ^{14}N. Half-life of the isotope is estimated to be 5730 ± 40 years (Goodwin, 1962).

Atmospheric ^{14}C concentration varies through time (Reimer et al., 2013). Fluctuation in the isotope production rate is caused by geomagnetic and solar modulation of the cosmic-ray flux, and the C cycle. If the conventional calculated ^{14}C age (non-calibrated) is placed within the past 200 years, it is termed as 'Modern' (Stuiver & Polach, 1977). Non-calibrated modern 14C dates are reported as percentage of modern C (pMC). pMC represents the proportion of anthropogenically-induced radiocarbon atoms in the sample compared to the 1950 AD level. Influx of artificial radiocarbon into the atmosphere was a result of nuclear bomb tests and led to a situation where modern age calculations present 'future' calculated date. Hence, a calibration of radiocarbon years is necessary. Initial results were calibrated with IntCal 13 calibration curve. It has been agreed that the year 1950 AD is used as the standard reference year (zero year), when converting ^{14}C age estimates to AD calendar years (Flint & Deevey, 1962). Thus, the ^{14}C dates can be converted to the AD scale without ambiguity arising from the year of measurement, publication, citation or from the decay of ^{14}C in oxalic acid. Accelerator mass spectrometry radiocarbon dating of modern peat samples can offer decadal-scale age resolution over the last several thousands of years and even more accurate results for the recent past (Turetsky et al., 2004). As related to methodological uncertainties, a combination of dating techniques should be preferably used.

^{210}Pb dating is one of the few independent dating methods that can yield a continuous chronology. Here it was used to increase temporal resolution for the recent changes in accumulation history. 70 profile sample segments were extracted from 9 of the profiles for ^{210}Pb dating. Profiles were subsampled with three-centimetre interval from surface downwards. Samples were freeze-dried and grinded fine. These samples were transported to University of Exeter in May of 2019. There ^{210}Pb dating was conducted by the author and a fellow student, with guidance of the laboratory personnel.

Samples were set into beakers and spiked with 1 ml of polonium-209 isotope (^{209}Po) yield tracer. Nitric acid (HNO_3 70%) was added to the mixture and set to a hotplate. Samples were brought to dryness, cooled down and then 10 ml of hydrogen peroxide added (30% H_2O_2). Once more, 5ml hydrochloric acid was (6M HCL) added, samples set back to the hot plate and brought to dryness. Residue formed was dissolved to hydrochloric acid (0.5M HCL). Solution was set into a centrifuge. Supernatant was moved to plating jars with added hydrochloric (0.5M HCL) and 0.2 grams of ascorbic acid ($C_6H_8O_6$). Silver discs were placed into the plating jar, suspended at end of a string. Plating jars were set to a magnetic stirring table (850rpm) for 24 hours. Here polonium's alpha emitting isotopes (^{209}Po & ^{210}Po) are absorbed to silver plates. Plates were removed, cleaned with

distilled water and then dated. Dating was conducted using Ortec Octête Plus Integrated Alpha-Spectrometry System (Software: Maestro-32).

When ^{14}C information relies on C assimilation of plants, lead-dating relies on ^{210}Pb deposits as dry or wet deposition from the air (Turetsky et al., 2004). Uranium-238 is a primordial nuclide with a long half-life (4.46×10^9 yr.). ^{238}U is found in all sediments and through a continuous decaying process produces ^{210}Pb and other daughter isotopes. Within soil uranium decays to multiple decay products, which subsequently decay to inert Radon gas (^{222}Rn). Through a series of short-lived isotopes ^{222}Rn decays to ^{210}Pb (half-life of 22.3 yr.). Thus, total ^{210}Pb found in soils has two components: component produced within soil by decaying ^{222}Rn and component derived from ^{222}Rn that was first diffused into the atmosphere and subsequently decayed to ^{210}Pb. Through dry fallout or wet deposition this diffused ^{210}Pb is then deposited to soil from the atmosphere. Thus, activity of the deposited ^{210}Pb in undisturbed, vertically aggrading soils, is greatest in young surface deposits (Appleby' & Oldfield, 1983). Activity tends to decrease in older, deeper material as a result of radioactive decay.

6.5 Age-depth models and recent accumulation rates

With R-based Bacon-package semi-automatic age-depth modelling script was composed, using ^{14}C and ^{210}Pb dating results jointly as input data (Appendix B) (Blaauw et al., 2020; R Core Team, 2019). For profiles that had only bottom layer dated, surface layer (0-1 cm) formation year was defined to sampling year. Bacon applies Bayesian statistics with prior information, using self-adjusting Markov Chain Monte Carlo -sampling method (Christen & Fox, 2010), returning posterior probability distribution of date estimates within 95% probability interval. Mean values of these date estimates, with one-centimetre interval were extracted.

Site-specific average C content was calculated from all successfully dated soil profile segments (Alkehornet: 31.9%, Björndalen: 40.5%, Bolterdalen: 26.3% and Colesdalen: 39.4%). For profiles with no C measurements conducted, site-specific average C content was imposed on every profile segment. Utilizing bulk density, C content information, and age-depth model results, recent C accumulation rates (g C m^{-2} yr^{-1}) were calculated for every soil profile with one-centimetre interval (Mäkilä, 2011). Due to large variation of mineral content in part of the subsample segments, formula used was adjusted to take this factor in consideration (Juselius et al. unpublished). Instead of using

dry bulk density of the whole subsample, bulk density of the organic material was used to dismiss impact of mineral material in samples. The adjusted formula is:

$$A\,c = r \times \omega \times C \times 1000$$

Where Ac = carbon accumulation rate (g C m^{-2} yr^{-1}), r = rate of vertical soil increment (mm yr^{-1}), ω= organic bulk density (dry bulk density × LOI) and C = carbon content as a proportion of dry bulk peat (%). Average non-cumulative apparent accumulation rates were calculated for three time-windows: 1900 AD, 1940 AD and 1980 AD till present, respectively. These focus periods were chosen to depict post "Little ice age" period, looking for signal related to recent climate warming. Calculations were carried out soil profile- and site-specific.

6.6 Digital surface model

Four DSM tiles with spatial resolution of 10 meters were pre-processed using QGIS 3.10.2 (QGIS Development Team, 2020). Tiles were re-projected to WGS84 / UTM 33N (EPSG: 32633) projection. Secondly, four tiles were merged to one raster and clipped to represent only area of Isfjord. Resulting product was visually inspected in case of anomalies. Artefacts showing high elevation values of over 400 meters, were identified over water areas of Isfjord. To ensure that these artefacts would not affect later processing steps, sea areas were masked out by using shapefile of Spitsbergen islands land area (Norwegian Polar Institute, 2014). Minor high-altitude areas with missing data were identified at southwestern part of the study area. These areas were covered by ice or snow in Landsat imagery. Thus, it was presumed that these deficiencies would not affect NDVI analysis negatively. Lastly, multilevel b-spline interpolation was used to reduce spatial resolution of the data to 30 meters, matching the spatial resolution of Landsat satellite imagery.

6.7 Landsat cloud masking

Boolean cloud mask raster layers were iteratively composed, based on quality assurance bands of every acquisition (appendix C) (United States Geological Survey, 2019b, 2019c). Pixels with low confidence of clouds were not included in the mask layers. Hence, possibility of losing valid pixels was avoided. Every pixel determined as cloud shadow, cloud, medium confidence cloud, high confidence cloud or high confidence cirrus was added to the mask file. These new cloud mask -raster files were iteratively written within every acquisition folder.

6.8 Data cubes and acquisition co-registration

Landsat product processing levels are defined so, that for time-series analysis, an image-to-image registration accuracy of ≤12-meter (RMSE) must be met (Dwyer, 2019). Additional georeferencing is likely needed when working across large spatial extents or timeframes, working with older imagery in the Landsat archive or areas of the world where sufficient ground control points have not been obtained (N. E. Young et al., 2017). Jupyter notebook was used through Anaconda science platfrom to compose Python script to select needed bands, stack these bands into data cubes and then co-register every cube (Appendix D) (Anaconda Software Distribution, 2016). Sub-pixel accuracy was set for accuracy requirement for co-registration.

Red band, NIR band and cloud mask were selected and these raster layers stacked. This was done iteratively to every acquisition. For every WRS-2 scene, that had Landsat 5 or 7 data downloaded, one Landsat 8 L1TP -image, was chosen as a reference image. Reference images with no cloud cover were preferred, or image with cloud cover as little as possible. For three of the WRS-2 scenes, Landsat 8 L1TP -images with low cloud cover were not available. Adjacent WRS-2 scenes have a large overlap at high-latitudes, so for these images, adjoining scene was selected as reference. Lower processing level Landsat 5 and 7 acquisition were co-registered with a Landsat 8 L1TP image.

Co-registration was conducted with python based AROSICS (Automated and Robust Open-Source Image Co-Registration Software) -package (Scheffler et al., 2017), using a computer running 64-bit Windows 10 Home Client, Intel i3-7100 3.91GHz CPU and 8.00 Gt RAM. AROSICS is independent of spatial or spectral characteristics and robust against high degrees of cloud coverage and spectral and temporal land cover dynamics. Methodology is based on phase correlation to estimate sub-pixel shifts in the frequency domain. To achieve this, Fourier shift theorem in a moving-window manner is utilized. Phase correlation delivers high accuracy co-registration results, even in the case of poor signal-to-noise ratios and substantial ground cover changes between different images (i.e. snow cover variation, deglaciation, and vegetation dynamics). A dense grid of spatial shift vectors is created, together with total of five individual validation and quality estimation metrics. These steps are: validity check of calculated integer shifts, displacement threshold check, cross-power spectrum reliability check of the respective tie point, image similarity evaluation before and after shift correction and utilization of robust RANSAC algorithm to estimate the parameters of an assumed affine transformation between the images, thus identifying outliers among the previously calculated shift vector grid (Fischler & Bolles, 1981; Hast et al., 2013).

AROSICS offers two optional approaches for co-registration, that the user can choose from, “local” and “global” approach (Scheffler et al., 2017). The local co-registration approach applies phase correlation in a moving-window manner to a regular grid of coordinate points and estimates X/Y translations for each point within the overlapping area of the input images. The global co-registration approach computes the displacements at only one small image subset, user defined by given grid size and centre coordinates. Global co-registration assumes that the whole misregistration between images can be described by a constant shift value and no displacement alteration occurs within the target image. Primarily, local co-registration was utilized. Tie point grid resolution was set to 40 pixels, max iterations to 20, maximum shifts to 80 and size of the moving window to 400 × 400 pixels. In un-successful cases, target image went through a two-step registration. First, global registration was used, to detect the large “main” shift. Secondly, new locally registered file was written, and the global approach was used into take in consideration the remaining shifts within this image.

6.9 Topographic correction

Topographic correction refers to the compensation of the different solar illuminations due to the irregular shape of the terrain (Riano et al., 2003). Due to this effect variation in the reflectance response of similar vegetation types occur. Shaded areas show less than expected reflectance, whereas in sunny areas the effect is the opposite. Topographic correction may be crucial for multispectral and for multitemporal analysis in areas of rough terrain.

Due to large topographic variation of the study area, R-based script was composed to consider the spectral variation caused by topography (appendix E). RStoolbox -packages topCor -function was applied, utilizing average cosine correction (Civco, 1989; Leutner, 2019). Average cosine correction was designed to compensate for overcorrection by the original cosine method (Pimple et al., 2017; Teillet et al., 1982). Thus, the average illumination is also included in the calculation formula of the method.

6.10 Annual NDVI composites and sensor harmonization

Co-registered imagery were clouds masked and NDVI was calculated. Resulting NDVI images were filed in folders based on their acquisition year. For every year pixel-wise maximum NDVI composite was created. If some year had only one acquisition, this image would be directly used. Maximum

NDVI, represents the peak vegetation photosynthetic activity of the growing season. It serves as an indicator of tundra biomass reached at that point of time. This parameter is least influenced by noise, cloud cover or variation in growing season length (Vickers et al., 2016; Walker, 2003). Also, in May 2003 Landsat 7 suffered the loss of its scan line corrector, leading to data gaps within images (Landsat Science, n.d.). Composites compiled from multiple images, can help to fill in these no data areas present in individual acquisitions.

R-based script was composed to calculate annual maximum NDVI composites and to consider the sensor harmonization (appendix F) (Robert J. Hijmans, 2020). When using data from three different sensors it is likely that cross-sensor discrepancies appear. There are small differences between red and NIR bands' spectral resolution between the sensors (United States Geological Survey, 2019b, 2019c). Ju and Masek (2016) proposed a method to derive cross sensor scaling factors between NDVI values. Method utilizes the fact that swath from two adjacent Landsat imaging paths have a side lap, which widens with increasing latitude. Images captured on consecutive days with two different sensors, are collected to compose a sequence of "triplet observations". Triplet observations are used to evaluate discrepancies between the sensors.

Not enough cloud-free imagery on consecutive days with differing sensors was found for the study area to empirically reproduce cross sensor evaluation. Using methodology depicted above calibration coefficients between Landsat 5 and 7, and between Landsat 7 and Landsat 8 sensors have been calculated for high-latitude acquisitions from Northern Canada (Pironkova et al., 2018). The NDVI composite scaling factors presented were, 1.036 to adjust Landsat 5 to its Landsat 7 equivalent, and 1.086 to adjust Landsat 8 to its Landsat 7 equivalent. Here those calibration coefficients were directly utilized. No smoothing was imposed to the harmonized annual composites, as averaging of NDVI values would be present in extraction of soil profile-wise time-series.

6.11 Statistical methods

Series of statistical tests were used to analyse the changes over time. R-based script to assess gradual change in vegetation over the whole Isfjord area and to extract soil profile coring pointwise timeseries was composed (appendix G). First, possible trends in vegetation cover composition during the 1985 to 2018 period was studied. Secondly, relationship between soil profile coring pointwise timeseries and apparent C accumulation rates were studied.

For trend detection pixelwise Regional Kendall Test was performed, which utilizes the Mann-Kendall rank correlation and Theil-Sen's slope estimator (Marchetto & Marchetto, 2017). Analysis does not require a normally distributed data; computations are possible even if data includes missing values, and the weight of extreme values does not affect the results the same way as in many other correlation tests. Regional Mann-Kendall test returns three raster files that include pixelwise values of Kendall's Tau, Theil-Sen's slope estimator and p-value. Kendall's Tau is a measure of concordance between two variables (time and NDVI) (Hamed, 2011; Kendall, 1948). Tau statistic presents the difference between the probabilities of concordance and discordance between the two variables. Tau values can vary between -1 (both variables have negative trend in perfect concordance) and +1 (both variables have positive trend in perfect concordance). Theil-Sens slope estimator is a non-parametric method to estimate linear trend, by fitting a line to the sample points in the plane, by choosing the median of the slopes of all lines through pairs of points (Theil, H., 1950). Pixelwise subset of resulting Theil-Sen's slope raster was compiled from pixels, that have Tau value <-0.4 or >0.4 and p-value < 0.05. Resulting in a raster that depicts pixels that has a negative or positive trend based on Tau values, and significant p-values on the level of 0.05 (Appendix H).

Theoretical analyses and field studies have shown that NDVI is near-linearly related to photosynthetically active radiation absorbed by a plant canopy, therefore also related to photosynthesis occurring in vegetation cover (Glenn et al., 2008). To compile soil profile-wise NDVI timeseries, buffer with radius of 50 meters, was determined around sampling point coordinates. A weighted mean of cell values falling within the buffer area was calculated. Approximate fraction of each raster cell falling within the buffer zone was used as the weight-component in the calculation. Valid values were restricted to higher than zero, to ensure that no snow-covered observations were considered. To assess relationship between the soil C accumulation rates and NDVI, a linear mixed effect model approach was adapted. Mixed models offer a useful approach to analyse unbalanced repeated measurements (Cnaan, 1997). Method differs of ordinary linear regression as it allows lack of independence between observations and to model more than one error term. Typical types of random effects are the division of study area to blocks or observational studies that are replicated across the sites or times (Bolker et al., 2009).

Soil profile coring plots had variation in environmental conditions and vegetation cover composition. Thus, variation in plot-wise NDVI values and their development during the study period was presumed. Recent apparent C accumulation rates were calculated for soil profile segments one centimetre thick, thus covering soil accumulated during several years or even tens of years

(accumulation rates ranged from 0.002 to 0.5 cm yr^{-1}, with average of 0.10 cm yr^{-1}). To reduce the difference in length of periods that the variables depict, a three-year moving-window averaging was applied to profile-wise NDVI timeseries. Normality of input data were assessed. Impact of averaging was evaluated by calculating Pearson's correlation coefficient between C accumulation rate and both averaged and non-averaged data before model fitting.

Presumed presence of differences in the slopes and intercepts of soil profile coring plot-wise NDVI and accumulation relationships were evaluated. First visual inspection was conducted, by fitting plot-wise linear regression lines. Then, a linear mixed effects model was composed using R-based lme4 -packages lmer-function (Bates et al., 2015) (Appendix I). Recent apparent C accumulation rates were determined as response variable, averaged NDVI as a fixed effect and individual coring plots were defined as random effect variables. Validation of mixed effects models is more complicated compared to linear models. Forming p- or R2-values for mixed models are not as straightforward as they are for the linear model. However, one can extract a significance values from comparison of two models. Requirements to consider random effects were studied by composing models sequentially and comparing them. Then marginal r-squared values and conditional intraclass correlation (ICC) for the models were calculated (Nakagawa et al., 2017). Marginal r-squared presents the proportion of the total variance explained by the fixed effects, and conditional ICC defines proportion explained by plot-wise clustering.

In total three models were composed: intercept only, random intercept (NDVI as fixed parameter with random intercept) and full model (NDVI as fixed parameter with random intercept and slope). Maximum likelihood estimation was used in model fitting, so that model fit comparison with analysis of variance (ANOVA) -test would be possible (McNeish, 2017). Maximum likelihood incorporates information about both the fixed effects and the variance components. For sequential comparison Akaike information criterion (AIC), Bayesian information criterion (BIC), conditional ICC, marginal R2, root-mean-square deviation and 95% confidence interval information were extracted to compare model goodness of fit (Akaike, 1974; Schwarz, 1978).

7. Results

7.1. Soil profile properties

Thickness of obtained soil profile samples varied greatly. Frozen soil restricting sampling depth at Alkehornet, indicated presence of permafrost. Average thickness of all the 15 soil profiles collected was 15.5 centimetres. Large site- and core-wise variation in soil properties was observed. At three of the sites: Björndalen, Bolterdalen and Colesdalen core-wise bulk density measurements followed lowering trend from bottom towards surface with slight variation. Highest bulk density values were measured from bottom samples. However, samples from Alkehornet showed large variation within profiles. Alk.7 profile deviated partly from the lowering trend from bottom to surface, with bulk density growing from bottom upwards, reaching peak at 6-7 cm depth, then declining towards the surface. Alike variation in samples from Alkehornet could also be seen in measured LOI values.

At Björndalen, Bolterdalen and Colesdalen slight variation in organic matter content was noted, but mainly all profiles followed an increasing trend in LOI values from bottom towards surface. At Alkehornet only Alk.1 profile had clear increasing trend, without large variation of LOI values. Other Alkehornet profiles showed large fluctuation of LOI within the soil profiles, with variation most evident in Alk.3 profile (Figure 5). LOI measurements of Alk.3, Alk.5, and Alk.7 showed high organic matter content in bottom samples, as LOI values calculated were still high (79.4%, 68.9% and 84.1%).

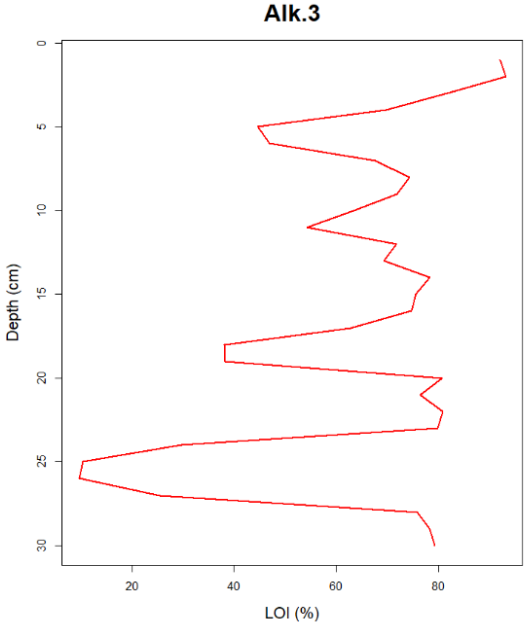

Figure 5. LOI measurements for Alk.3 soil profile. LOI (%) presents relative organic matter content as percentages. Highest content was measured at surface sample 0-1cm. Bottom sample (29-30 cm) has LOI (%) of 79.43. Variation within the soil profile is large, which implies that at multiple occasions mineral soil has mixed with the accumulated organic soil matter.

C and N values were derived from individual profiles and site-specific averages calculated. Profile-wise N content did not show clear trends. Content varied within profiles, without evident increasing or lowering trend, that would have followed sampling depth. However, variation between site-specific average N content was evident (Table 3). N content results from Alkehornet showed notably higher values compared to other sites. C content measurement results mainly showed increasing trend in soil profile segments from bottom to surface. Alkehornet site's sample profiles that had fluctuation in bulk density and LOI, also had variation discrepancies in

C content measurements within profiles. Site-specific C average values ranged from 23.28% to 38.55%. From C and N measurements C/N ratio was calculated. Higher N content at Alkehornet is visible also when comparing site-specific C/N results.

Table 3. Site-specific data (minimum, average and maximum) of nitrogen content in percentages (N%), carbon content in percentages (C%) and ratio of the nitrogen and carbon content (C/N). Alkehornets' nitrogen content results clearly differ from other three sites. Variation in maximum carbon content measurements between the sites is small. More variation is perceived in minimum and average values. C/N ratio shows clear difference between Alkehornet and other sites. At Alkehornet all C/N ratio statistics are considerably smaller than at other sites.

Site	Alkehornet			Björndalen			Bolterdalen			Colesdalen		
stat	min	avg.	max	min	avg.	max	min	avg.	max	min	avg.	max
N%	0.95	1.99	3.04	0.15	0.93	1.4	0.29	0.60	1.02	0.52	0.97	1.59
C%	13.62	32.335	40.94	3.93	32.24	42.37	7.63	23.28	38.56	31.94	38.55	41.13
C/N	10.42	17.57	40.44	26.97	40.37	53.14	17.86	37.86	64.63	20.12	45.48	78.51

7.2 Chronologies and age-depth models

Large portion of bottom layers dated with ^{14}C method yielded modern ages (deposited after 1950 AD) (table 4). Alkehornet soil profiles were much deeper and older than the profiles collected from other sites. Alk.4 bottom sample (depth of 24-25 cm) yielded oldest calibrated age of 5863 BP, and the additional sample towards top (depth 14-15 cm) age of 1341 BP. Youngest bottom sample from Alkehornet was Alk.1 (depth of 10-11cm). It was dated to 1950 BP. Regarding Björndalen, Bolterdalen and Colesdalen, the calibrated ages of the bottom samples varied between 155 BP and -31 BP. Multiple bottom samples from these three sites had low LOI, which indicates that visual determination of lowest organic sample segment was inaccurate.

In general, the amount of ^{210}Pb extracted from sample segments with three-centimetre interval, expressed decreasing activity of ^{210}Pb as presumed (Figure 6). For an unresolved reason Col.1 profile did not follow a decreasing trend. Thus, date estimation for this profile was unsuccessful with ^{210}Pb method and only ^{14}C bottom layer age could be used as input for age-depth model. Zero activity level of the profile subsamples was often reached near a halfway of a profile. Thus, ^{210}Pb procedure did not provide age-estimation for the deeper layers.

Table 4. Results of ^{14}C dating, with samples identified by unique Id and the sample depth. Loss on ignition percentage (LOI %) indicates percentage of organic material in the sample. Non-calibrated dating results are reported as BP ^{14}C dates. Modern non-calibrated dates are reported as percentage of modern carbon (pMC). Calibrated ages are reported as calibrated before present dates (BP cal.)

Site	Core Id	Depth (cm)	LOI %	BP ^{14}C	BP cal.
Alkehornet	Alk.1	10-11	33.47	2003 ± 23	1950
Alkehornet	Alk.3	29-30	79.43	1510 ± 35	1497
Alkehornet	Alk.4	24-25	12.01	5030 ± 40	5863
Alkehornet	Alk.4	14-15	82.10	1195 ± 22	1341
Alkehornet	Alk.5	23-24	68.91	3079 ± 22	3218
Alkehornet	Alk.7	31-32	84.14	4480 ± 35	5228
Björndalen	Bj.1	12-13	52.34	100.11 ± 0.31 pMC	67
Björndalen	Bj.2	9-10	39.86	129,31 pMC	-27
Björndalen	Bj.3	6-7	49.92	106.98 ± 0.33 pMC	-33
Bolterdalen	Bo.1	11-12	19.05	101,76 pMC	-7
Bolterdalen	Bo.3	12-13	20.83	107.38 ± 0.33 pMC	-10
Bolterdalen	Bo.4	15-16	11.13	100.41 ± 0.32 pMC	-7
Bolterdalen	Bo.6	8-9	12.39	103,34 pMC	-10
Colesdalen	Col.1	10-11	41.93	128 ± 0.37 pMC	-31
Colesdalen	Col.2	10-11	23.67	102.24 ± 0.32 pMC	-8
Colesdalen	Col.4	7-8	68.03	176 ± 26	155

^{210}Pb-based chronology from Alkehornet reached the early 1800s AD. The Björndalen chronology reached early 1970's AD. The Bolterdalen chronologies covered approximately half of the profiles in terms of depth. For Bol.3 and Bol.4 profiles the chronologies reached until 9 cm deep, with an age estimate placing in the 1950's AD and early 1910's AD, respectively. Out of Colesdalen profiles, only Col.2 profile was reliably dated by ^{210}Pb. Col.2 reached chronology reached 6-7cm depth with an age estimate of 1995 AD.

Profiles that had only bottom layer dated, the accumulation rates were practically linearly modelled (Figure 7). Profiles with combined chronologies showed larger variation in accumulation rate patterns. At Alkehornet steep increase in accumulation rates of Alk.4 and Alk.7 profiles was distinguished. Björdalen profiles Bj.1 and Bj.3 showed more moderate, but steady increase in accumulation rates. At Bolterdalen Bo.3 and Bo.4 profiles have alike sections in the depth of circa nine to four centimetres, where the accumulation rates lower slightly, and then start to increase. At Colesdalen, Col.2 profile shows a steady increase of accumulation rate, but large uncertainty area for the lowest ^{210}Pb dated sample exists (area coloured with cyan colour).

Bo.4 profile had one 210Pb age at depth of 8-9 cm, which was an outlier. This age was omitted, and confidence rather put on the bottom age of the profile. Decision was justified as Bo.3 and Bo.4 bottom ages supported each other. Profiles with multiple dated samples, showed conformingly increasing accumulation rates towards the profile tops.

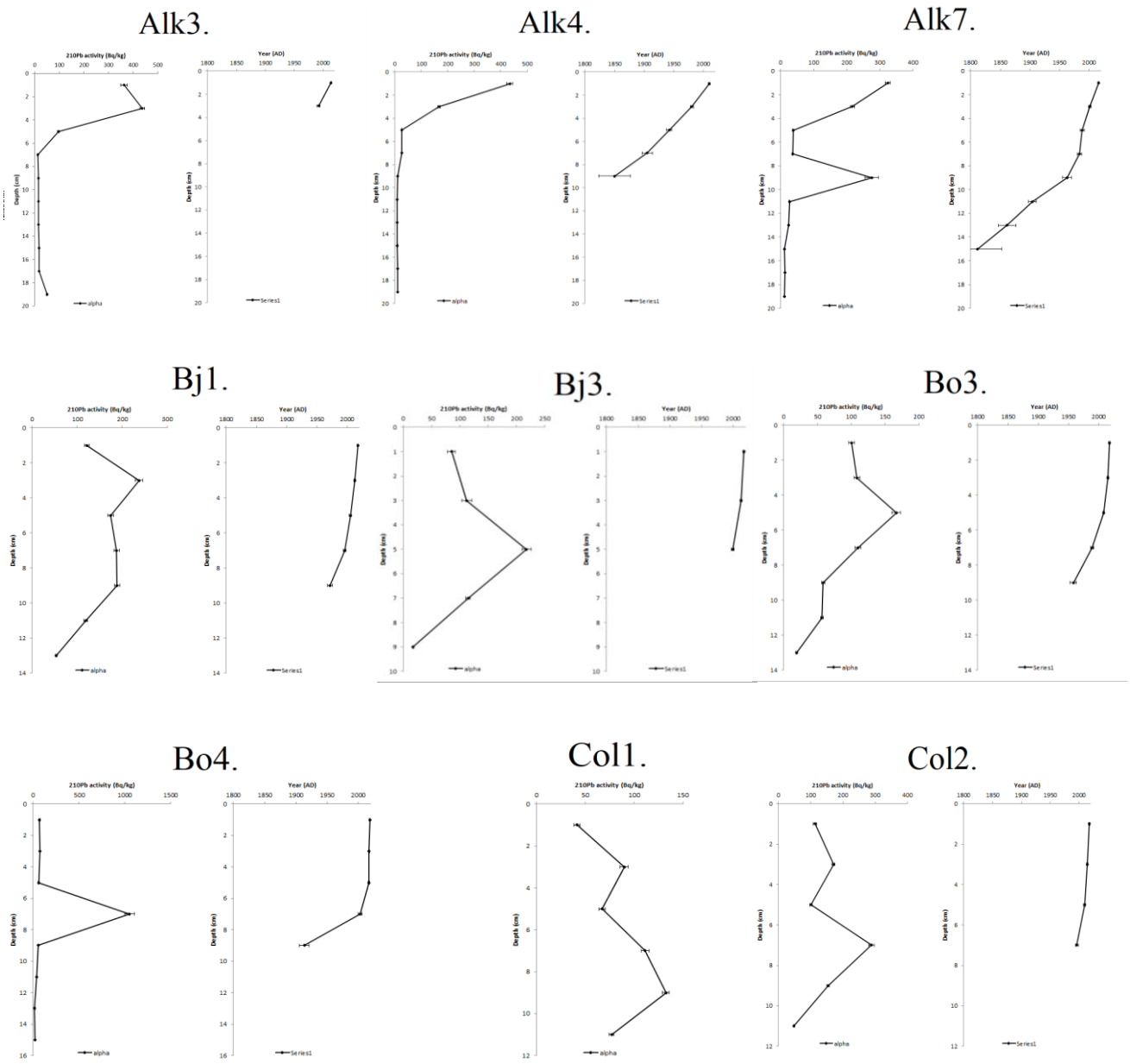

Figure 6. ^{210}Pb dating results with the activity of ^{210}Pb as Bq/kg and the corresponding AD year estimations visualized against soil profile section's depth. Method presumes decreasing activity by depth. Generally, reliable date estimations cannot be produced for deepest measurements, as the decreasing ^{210}Pb activity is associated with increasing level of uncertainty. Thus, most date estimates produced here reach circa halfway mark of the full profile length. For unresolved reason Col1. sample activity did not follow decreasing trend, and zero activity level was never reached. Thus, reliable date estimates could not be derived for this profile.

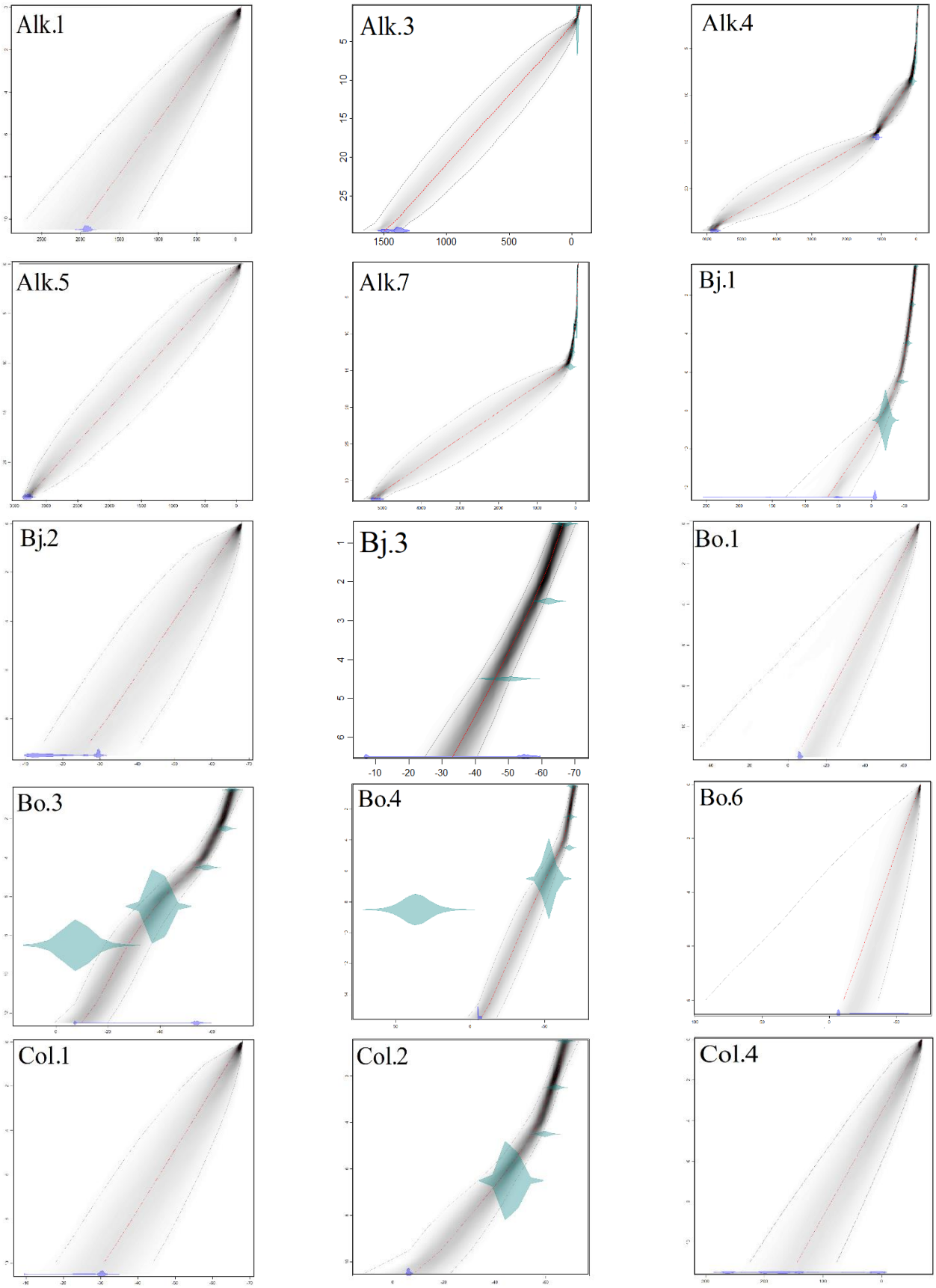

Figure 7. Age-depth models results visualized (X-axis presents dates (BP cal.) and Y-axis sample segment depth (cm)). Individual plot-scales differ due to variation in profile thickness and accumulation histories. ^{14}C results are presented in blue and ^{210}Pb results with green. Dark dotted lines present 95% confidence intervals, areas with grey shading present posterior probability distribution of date estimates and red line their mean.

7.3 Recent carbon accumulation rates

In total, recent C accumulation rates with one-centimetre depth interval, were successfully calculated for 237 sample segments. Dated bottom ages varied significantly between profiles and between sites. Focus was set on three determined periods to facilitate comparison: 1900 AD, 1940 AD and 1980 AD till present, omitting observations dated older than 1900 AD. Count of remaining C accumulation rate estimates per focus period were: 129, 121, 88 (gross portion of accumulation rate estimates concerning Alkehornet were omitted due to their old age). Accumulation rates were not constant within the profiles nor within the sites (Figure 8). Björndalen, Bolterdalen and Colesdalen sites had individual bottom samples younger than 1940 AD and younger than 1980 AD. Thus, recent accumulation rate estimations of some profiles did not cover all three focus periods.

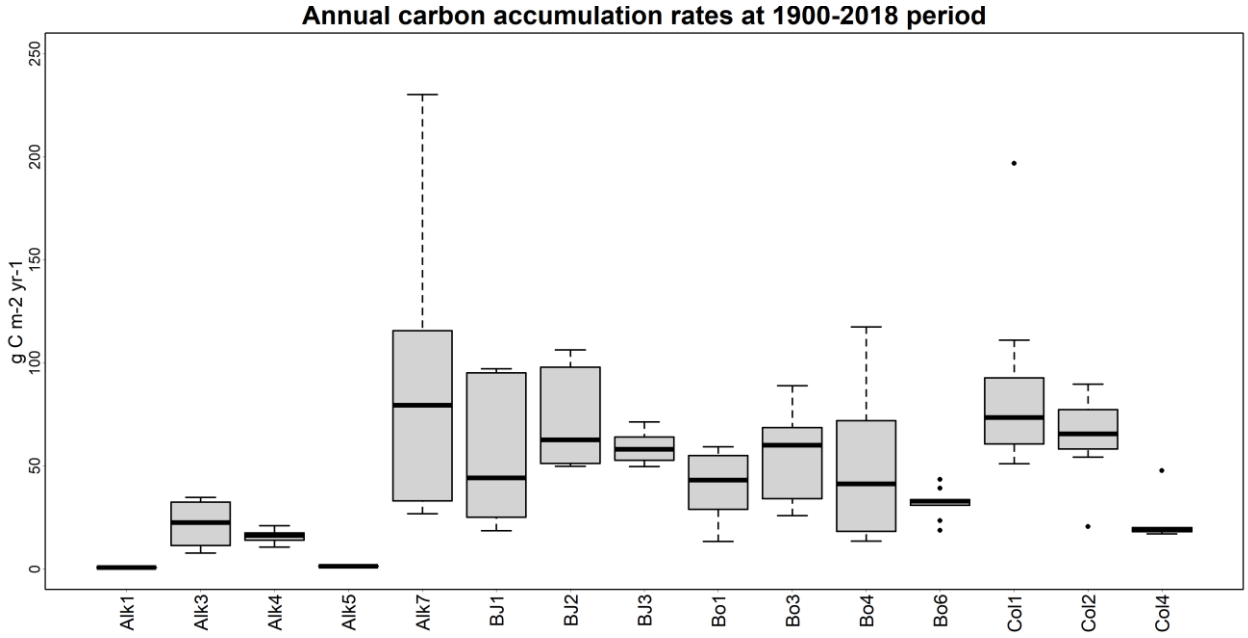

Figure 8. Distribution of annual carbon accumulation rates per soil profile within the longest focus period presented. Large profile and site-specific variations are distinguishable. Alk.7 demonstrates large variation when compared to other profiles from Alkehornet.

Alk.1 and Alk.5 profiles had only one observation that was dated younger than 1900 AD. Thus, no variation within study period was observed, concerning these two profiles. Bo.4 profile had highest count of 16 observations placing within the longest study period. Large variation in count of observations is strongly related to variation in magnitude of organic matter and C accumulation rates. Profiles with large count of date estimates, have accumulated a thicker soil layer in a shorter time, compared to the ones with lower observation count. Overall, calculated accumulation rates for individual profile segments ranged between 0.68 and 230.20 g C m-2 yr-1. Both, smallest and largest values were obtained from Alkehornet. Average of all accumulation rates within the longest focus period was 53.76 g C m^{-2} yr^{-1}.

Despite large variation in soil profile-wise annual accumulation rates, a growing trend was perceivable within most of the soil profiles when averaged per study periods (Table 5). However, Bo.1 -profile had a decrease of 7.77 g C m^{-2} yr^{-1} in average accumulation rates between 1940 AD and 1980 AD. Also, Bj.2 and Bo.6 showed minute decreases during the same period. Site-specific averages and average of all the calculated accumulation rates still conveyed information of increasing trend during 1900 to 2018 AD period (Table 6).

Table 5. Average recent carbon accumulation rates (RERCA) (g C m^{-2} yr^{-1}) per soil profile (Profile ID) were calculated for periods 1900 AD, 1940 AD and 1980 AD till present. Bottom age indicates date estimation of when organic soil has started to accumulate in calibrated BP dates. If core-specific accumulation rate estimates did not cover certain focus period, not available (NA) value was determined.

Profile ID	Bottom age (BP cal.)	RERCA 1900 AD	RERCA 1940 AD	RERCA 1980 AD
Alk1.	1950	0.68	0.68	0.68
Alk3.	1497	21.95	26.68	32.53
Alk4.	5863	15.98	16.06	16.38
Alk5.	3218	1.30	1.30	1.30
Alk7.	5228	92.27	98.83	124.38
Bj1.	67	53.30	59.71	74.82
Bj2.	-27	NA	72.54	71.08
Bj3.	-33	NA	NA	58.99
Bo1.	-7	NA	41.10	33.33
Bo3.	-10	NA	54.52	62.28
Bo4.	-7	NA	47.47	57.66
Bo6.	-10	NA	31.98	31.55
Col1.	-31	NA	NA	85.23
Col2.	-8	NA	65.47	69.76
Col4.	155	23.63	25.56	32.96

Table 6. Average recent carbon accumulation rates (RERCA) (g C m^{-2} yr^{-1}) per site (Site) and for all the sites together (Total) were calculated for periods 1900 AD, 1940 AD and 1980 AD till present. Bottom age indicates average of all dated profile bottom segments per site in calibrated BP dates. If none of the site's profiles reached as far back as the study period, not available (NA) value was determined. Otherwise site-specific average was calculated from available data.

Site	Bottom age (BP cal.)	RERCA 1900 AD	RERCA 1940 AD	RERCA 1980 AD
Alkehornet	3551	52.72	60.85	76.80
Björndalen	2	61.31	64.28	68.54
Bolterdalen	-8	NA	47.84	52.53
Colesdalen	39	64.27	67.69	74.36
Total	896	53.76	56.04	62.94

7.4 Recent climate history

In a previous study, substantial variation in temperature and precipitation has been observed at Svalbard during 20th and 21st century (Førland et al., 2011). Positive trend in both temperature and precipitation at Svalbard was detected. However, 1943–1965 was a period with rather strong winter cooling, which led to an overall decline in the annual temperatures. Obtained measured weather data used here agrees with those observations (Figure 9).

Range of annual mean temperatures for 1900–1909 period was from -8.1 to -7.0 °C. In comparison, range of average of annual mean temperatures for 2009–2018 period was from -3.3 to -1.8°C, suggesting significant increase in annual temperatures between these decades. Data of the summer month mean temperatures starts from the year 1914. Range of summer month mean temperatures during the first decade of observations (1914–1923) was from 3.4 to 4.5 °C, and range of 2009–2018 period was from 5.74 to 6.1 °C. Implying that temperature rise has not been as strong during the summer months (growing season) as for the rest of the year. The annual sum of the effective temperature does not show similarly distinct positive trend, supporting deduction that warming has been less pronounced for the growing season. Annual precipitation data shows large fluctuation during the 20th century followed by a sharp increase during 21st century.

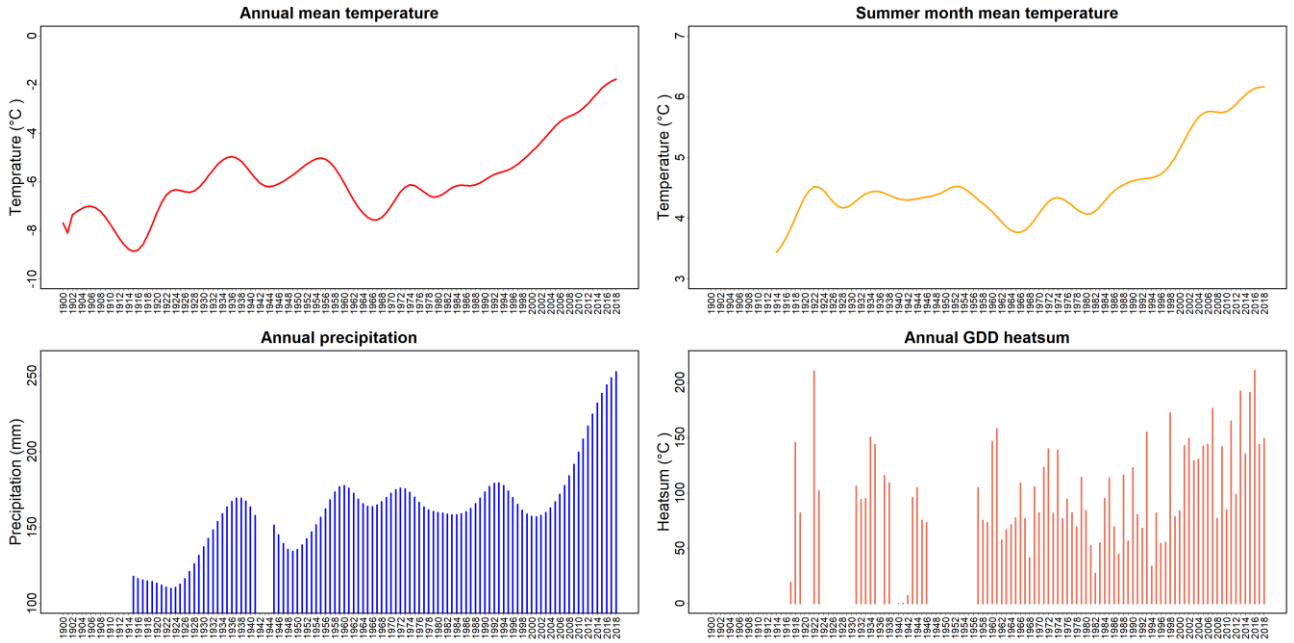

Figure 9. Four historical weather datasets plotted, for the years with available data (Norwegian Meteorological Institute, 2020a,2020b,2020c,2020d). Annual mean temperatures and summer month mean temperatures both have followed similar rising trend. Annual precipitation displays fluctuation and large increase during 21st century. Annual sum of the effective temperature days (Annual GDD heat sum) shows more variation compared to the two other temperature variables. Still, similar growing trend is distinct from the 1980's forward.

7.5 Landsat co-registration and topographic correction

In total, co-registration process of the 54 acquistions, took approximately 74 hours. Processing time of individual image varied from 33 minutes (tie point grid of 4605points, resulting in 1508 valid matches) to 2 hours and 40 minutes (tie point grid of 18456 points, resulting in 15727 valid matches). Thirteen images went through the two-phased co-registration. Ten of these images were eventually disregarded in the validation phase (Figure 10), as they could not reach a sub-pixel accuracy. Images that could not be corrected, suffered at least from one of these traits: majority of the image was covered by clouds, image had extremely large spatial shifts or image had distinct geometrical distortions (portion of L1GS images). Largest shift detected by global registration was 316 pixels on

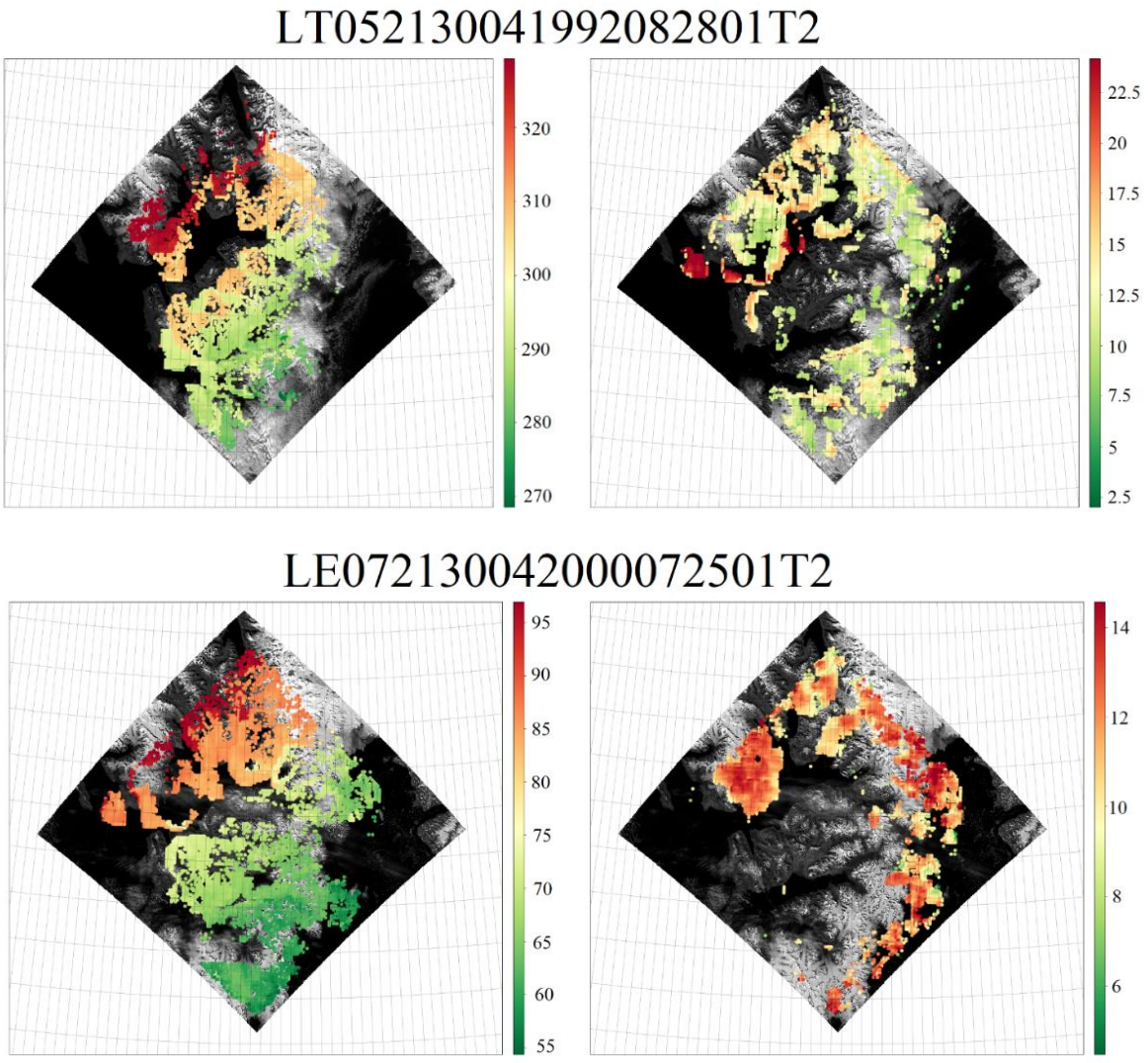

Figure 10. Results of one Landsat 5 and one Landsat 7 acquisition co-registration with AROSICS presented. Acquisition filenames are presented on top of the presentations. Panels on the left side, presents initial spatial shifts in meters found by AROSICS in the original acquisition images. In co-registration process 4421 valid tie points were found for the Landsat 5 and 6035 valid tie points for Landsat 7 image presented here. Right Panel shows spatial shifts observed after co-registration. It is evident that spatial shifts remain within the imagery, but they are significantly reduced. In both presented images, sub-pixel accuracy was reached.

X-axis and 702 pixels on Y-axis, translating to a shift of 9.48 kilometres on x-axis and 21.06 kilometres on Y-axis. Out of 54 images with insufficient georegistration, 44 were reliably co-registered. When taking Landsat 8 data into account, a total image pool of 84 reliably geo registered images within 1985 to 2018 period was achieved (Table 7). For all these images topographic correction was successful.

Table 7. Year of acquisition (year) and number of reliably co-registered images (images) presented. These statistics includes Landsat 8 images that were initially reliably geo-registered. Due to high cloud cover at the study area and acquisitions that could not be reliably co-registered, five years of the study period are missing imagery completely. It is noticeable that quantity of images available per year is focused towards the end of the study period.

Year	Acquisitions
1985	3
1986	4
1987	2
1988	0
1989	5
1990	0
1991	2
1992	4
1993	2
1994	1
1995	1
1996	1

Year	Acquisitions
1997	0
1998	1
1999	2
2000	3
2001	1
2002	3
2003	0
2004	1
2005	1
2006	3
2007	0
2008	1

Year	Acquisitions
2009	2
2010	4
2011	4
2012	2
2013	2
2014	8
2015	4
2016	10
2017	2
2018	5

7.6 Spatiotemporal trends of NDVI

From successfully co-registered and topographically corrected images, cloud free annual pixelwise maximum NDVI composites were composed. Resulting to 29 annual maximum value composites. Leaving five years with no data available (Table 7). Pixelwise masking of Theil-Sen's slope raster by Tau and p-values resulted into gross portion of high elevation and glaciated areas being masked out. Thus, regarding pixel-wise change in NDVI values only at areas with significant change.

Masked Theil Sen's slope values ranged between -0.0309 and 0.0300 (Figure 11). Low quantity of pixels with a slope value zero, is a result of Tau-value masking. Calculated average of slope values was 0.0059. Utilizing this average value, to

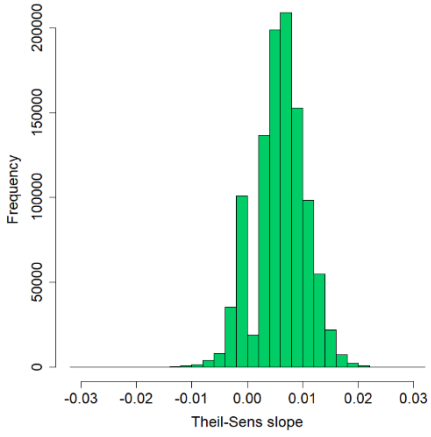

Figure 11. Distribution of masked Theil-Sens slope values.

estimate NDVI change during the study period, results in NDVI increase of 0.1950. Comparing this to average value from corresponding pixels in maximum NDVI composite of the year 1985 (average NDVI of 0.1955), this would translate to 99% increase in average NDVI values. To support these results annual averages of pixels corresponding to masked Theil Sen's values were calculated from annual maximum value NDVI composites (Figure 12). Averages derived from maximum value composites raster, showed an increasing trend. Though, extremely low average NDVI values were noted for three of the years (1994, 1996 and 2009).

In terms of spatial variation, positive slope values were detected at valleys and lowland areas (Figure 13). Implying to greening during the 1985 AD to 2018 AD period. High values on a large area, were especially noted in the south-eastern section of the covered study area (Reindalen). All off the soil profile coring sites, showed positive slope values. Negative values were found from riverbeds, furrows and high-altitude areas (Similar areas where most NA values appeared.), gross portion located at north-western parts of the study area. Affects of the Landsat 7 missions missing scan line corrector can be seen at the northern shoreareas of Isfjord, where sections with clearly striped spatial pattern of NA-values can be seen.

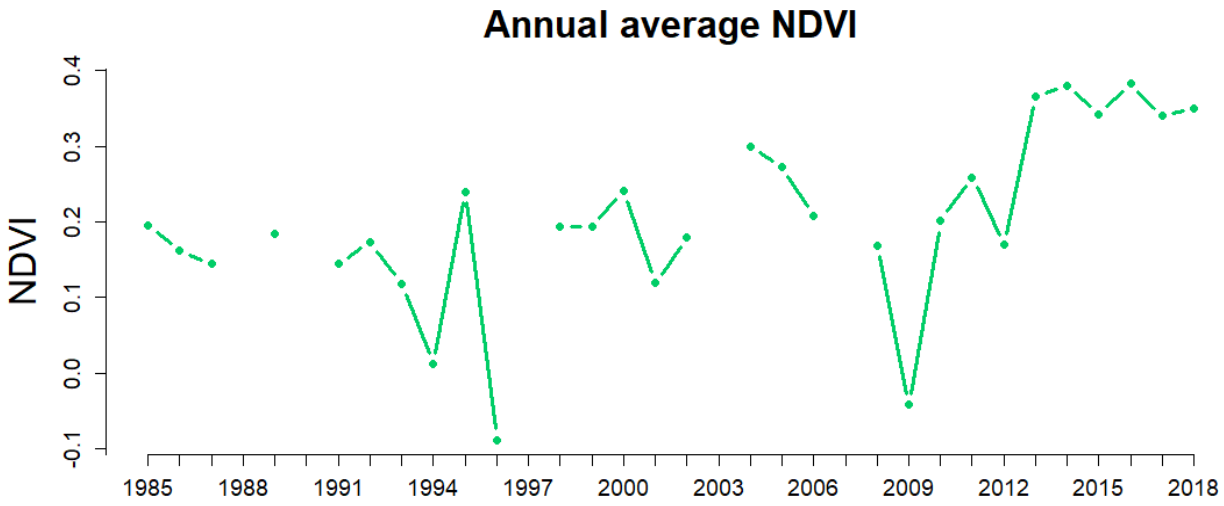

Figure 12. Annual average NDVI values calculated from maximum NDVI composites. Values were calculated from pixels corresponding to the masked Theil-Sens slope pixels. At least two years with clears outlier values are evident. Years 1996 and 2009 were strongly affected by scarcity of data and possibly large areas recorded were still snow-covered.

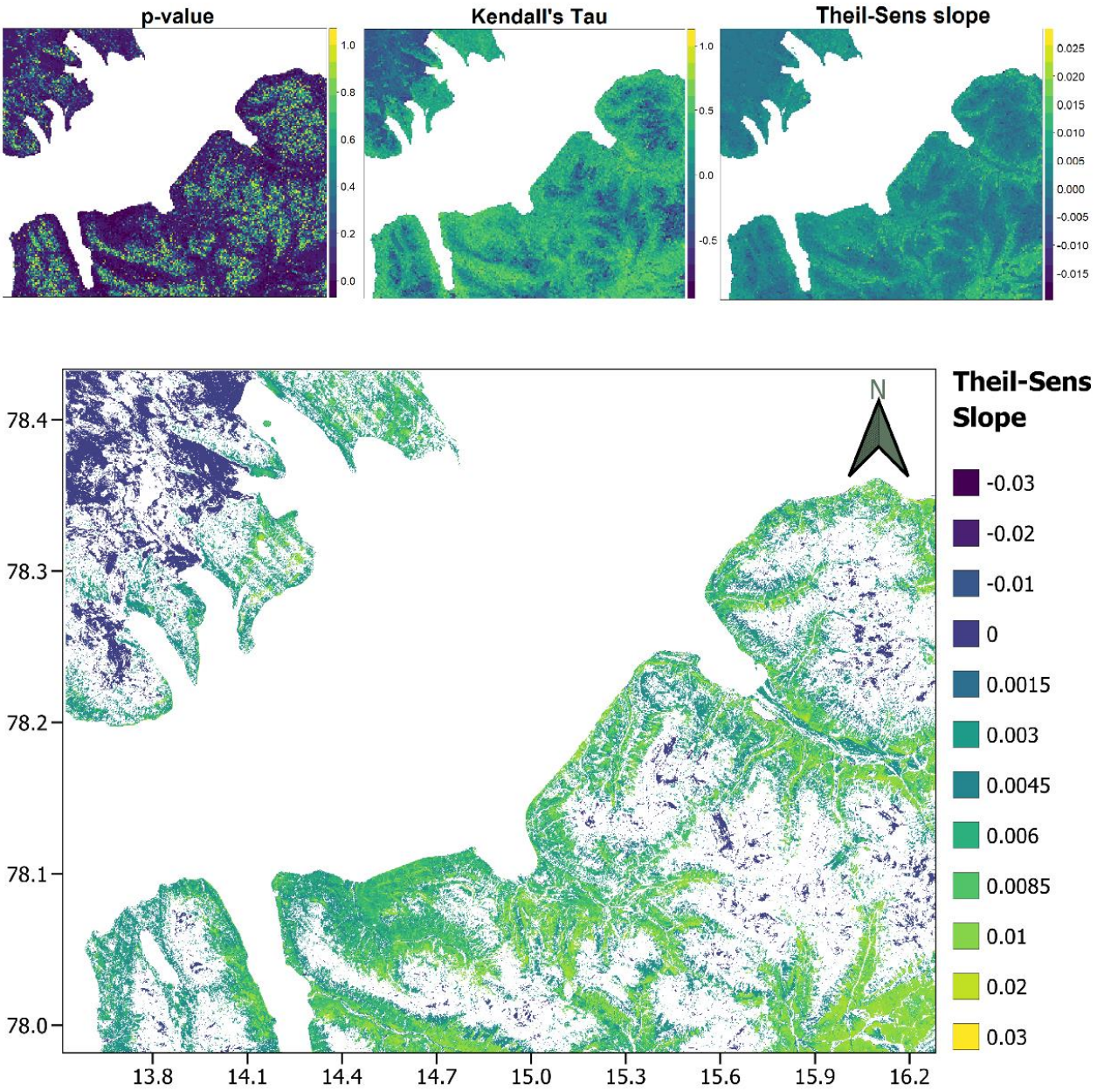

Figure 13. In the top row original output rasters of regional Mann-Kendall test are presented. Pixels with high p-values occurred mostly at high altitude areas. Tau values at valley floors and at shore areas showed strong positive trends. Tau values close to zero appear at high altitude areas, showing no clear change. Thus, advancing masking of pixels from high altitude areas. Masked Theil-Sens slope pixels present strong positive trends at valleys and low land areas. Large areas with high positive slope values occur in the valleys located in the south-eastern parts of the study area. Negative trends were found from high altitude areas, riverbeds, and furrows. However, it should be noted that, most streams and rivers have been masked out.

7.7 NDVI and recent carbon accumulation rate

Profile-wise, three-year moving window averaging resulted to 79 pairwise observations of NDVI and recent apparent C accumulation rates. Count of pairwise observations was unevenly distributed between sampling plots (Table 8). Few extremely high C accumulation rates were estimated for years with high soil accumulation rates. These were not treated as outliers nor removed. In the input data original annual maximum NDVI and recent apparent C accumulation rates showed Pearson correlation of only 0.03. Using NDVI data averaged with the three-year moving window increased Pearson correlation to 0.14. Thus, moving window averaged data was selected for the following analysis steps (In this chapter NDVI -term refers to this averaged data).

Table 8. Distribution of pairwise recent carbon accumulation rates and NDVI observations during the 1985 to 2018 period. Limited amount of observations hindered evaluation of the relationship at individual plots.

Profile	Alk.1	Alk.3	Alk.4	Alk.5	Alk.7
Observations	1	2	2	1	5
Profile	Bj.1	Bj.2	Bj.3	Bo.1	Bo.3
Observations	7	8	6	7	7
Profile	Bo.4	Bo.6	Col.1	Col.2	Col.4
Observations	9	5	10	7	2

Fitting plot-wise linear regression lines between NDVI and accumulation rates, confirmed presumptions of plot-wise differences in the slopes and intercepts (Figure 14). Large variation was visually observable. In addition, intercept only mixed model supported observations of plot-wise differences in terms of intercept values (Appendix E). Intercept only model showed large residual variance on profile plot level, with an intraclass correlation value of 0.50. Fair intraclass correlation value shows that observations are more similar within the plots than between them (plot-wise clustering explains 50% of variance). These observations enforced the assumption that the final model should take into consideration the random effects caused by variation between soil profile coring plots.

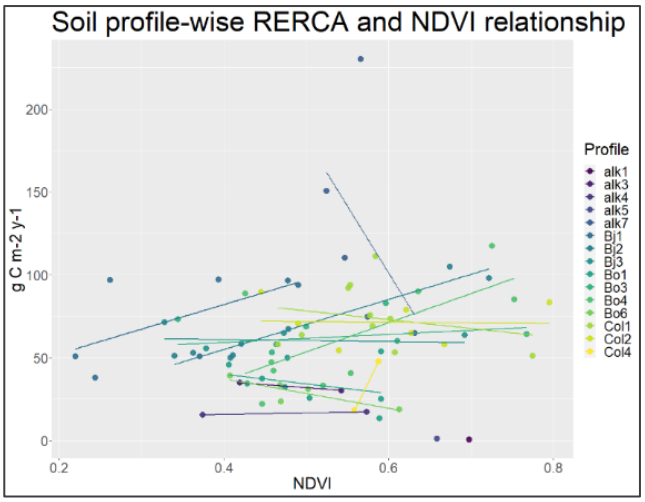

Figure 14. Soil profile-wise linear regression lines between recent carbon accumulation rates (RERCA) and normalized difference vegetation index (NDVI).

Sequentially adding random intercept and slope, did not lead to eminent improvements in AIC or BIC values retuned by ANOVA-test, nor were comparison within statistically significant range ($p<0.05$) (Table 8). With the full model intercept and slope returned a correlation value of -1, which implies that model cannot simultaneously consider individual random variation of both. Also, conditional ICC rose and marginal R2 lowered when adding random slope. Still, theoretically the full model is most justified option. Root-mean-square results did not show large variation between the models. Large range of confidence interval implies uncertainty in accuracy fixed effect estimates. In addition, all models were tested for singularity and residuals for homoscedasticity and normality. All model tested false for singularity and in terms of homoscedasticity residuals were evenly distributed.

Table 9. Results of compared individual models: intercept only (ic.only), random intercept (r.ic), random intercept and random slope model (full). Statistics include fixed effects estimates for intercept (IC) and NDVI, analysis of variance, conditional intraclass correlation (ICC), marginal R2 (R2), root mean square deviation (RMSE) and 95% confidence intervals. Every model returned conditional R2 value (conditional ICC + marginal R2) over 0.50, but NDVI was responsible of only a fraction of the variation (marginal R2), and plot-wise variation explains over 50% with every model. RMSE results of every model were congruent. Confidence intervals show large range for fixed effects.

Model fit	Fixed effects estimates		Analysis of variance			ICC	R2	RMSE	95% confidence interval	
	IC	NDVI	AIC	BIC	p-value				IC	NDVI
ic.only	53.856	NA	770.47	777.58	NA	0.503	0	23.98	39.92 to 68.80	NA
r.ic	28.82	46.86	769.71	779.18	0.09638	0.523	0.02	23.29	-3.62 to 61.26	-7.63 to 101.07
full	39.0	26.68	772.24	786.46	0.48160	0.530	0.01	23.08	11.79 to 66.21	-30.39 to 87.75

In summary, every model implied plot-wise difference, and mainly positive relationship between apparent C accumulation rates and NDVI (Figure 15). Fixed effect of NDVI appeared to be strong, but wide 95% confidence intervals lead to low accuracy of the estimates. Explanatory power of the models was weak, even at its best only 2% of the total variation of apparent C accumulation rates was explained by NDVI, when over 50% resulted from plot-wise variation.

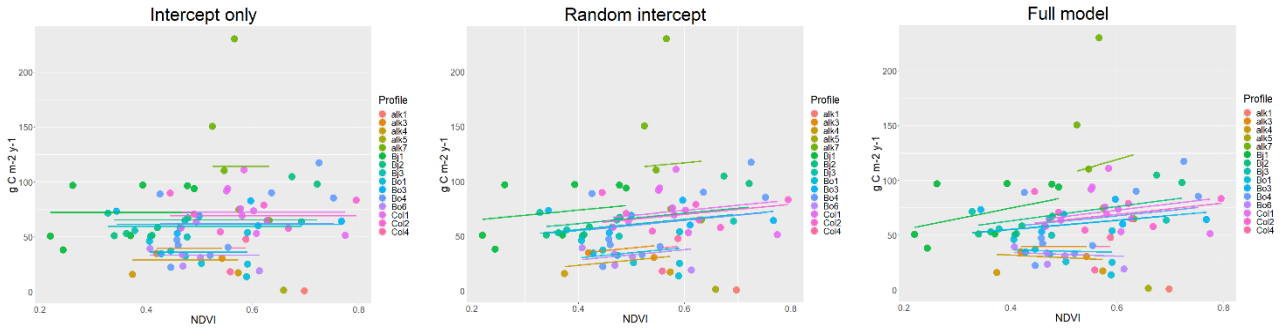

Figure 15. Results of all three model fits presented. Fitted measurement points and regression lines are plot-wise color-coded. Intercept only model shows variation of plot-wise intercept estimates. With random intercept model this variation of intercept is considered, but the NDVI as predictor variable has fixed slope regardless of the plot. Full model includes plot wise variation both in intercept and slope. Every plot likely had individual land cover traits and vegetation development history. Thus, full model theoretically permits most solid estimation of relationships between NDVI and soil C accumulation rates.

8. Discussion

Site-specific recent average C accumulation rates obtained in this study are higher than maximum rates estimated for northern peatland areas during the Holocene and higher than recent average annual rates (Loisel et al., 2014; Treat et al. 2016; Z. Yu et al., 2011). However, range of profile-wise calculated accumulation rates was large. Only few remote sensing studies from Isfjord area utilizing NDVI have been conducted. Touching on subjects of NDVI and field-recorded phytomass (B. Johansen & Tømmervik, 2014), spatiotemporal variability in the onset of the growing season (Karlsen et al., 2014) and monitoring of arctic greening (Vickers et al., 2016). To authors best knowledge, no earlier studies from Svalbard exist that would have produced directly comparable results, in terms of recent soil C accumulation rates. Nor has NDVI timeseries applicability as a predictor of soil C accumulation, been assessed against dated soil samples before.

8.1 Recent carbon accumulation rates and environmental drivers

Soil C accumulation rates are highly variable spatially and temporally. Local variation can occur even within seemingly homogenous and small areas. The soil C fluxes are controlled by multitude of biogeochemical transformation and transfer processes. Results suggested that organic soil formation, possibly indicating onset of paludification at Björndalen, Bolterdalen and Colesdalen sites has initiated in the recent past (Table 4 & Table 5). Oldest bottom age measured from these sites was dated 225 years old, youngest bottom age was dated to -33 BP. Soil profile bottom ages from Alkehornet differed clearly from these ages, as they were thousands of years old. Mineral soil was

reached only with one of the Alkehornet soil profiles due to permafrost, thus complete thickness of organic soil profile could not be measured. Minor discrepancies in organic matter accumulation histories were evident in profiles collected from Alkehornet (Figure 5); occasionally the organic layers were interrupted by minerogenic input mixing into organic soil matrix, likely due to cryoturbation or soil mass movements induced by gelifluction at the ridges.

All profiles with multiple dated segments, showed increase in recent organic matter accumulation rates (Figure 7). Nonetheless, large variation in recent C accumulation rates between individual soil profiles and within the study sites were observed (Table 5 & Figure 8). Reason behind of all intra-site variations were not differentiated. Levelling of extreme values took place as site-specific recent C accumulation rates were calculated, in pursuance of regionally representative data. Site-specific average rate results (Table 6) and average rate of all observations during the 1900 AD to 2018 AD period (53.76 g C m^{-2} yr^{-1}), implied that recent apparent C accumulation rates at the study area have been greater than at most high-latitude peatland areas. All site-specific recent average C accumulation rates coherently showed an increasing trend, implying increase in soil C pool at inner fjord areas of Svalbard. Still, it should be taken to consideration, that the newly added litter has not had time to fully decompose. Thus, interpretation of the signal is not unambiguous. Studies concerning high-latitude peatlands have reported alike high recent average annual C accumulation rates and notable increasing trend, from south central Alaska (Loisel & Yu, 2013), north-western Québec, Canada (Piilo et al., 2019), northern Finland and Russia (Zhang et al., 2018).

Due to climate change the need to understand and predict current Arctic environmental changes has increased. A relatively sparse measurement network limits the availability of information concerning recent changes in C accumulation rates of high-arctic ecosystems. Multiyear C balance measurements carried out during the recent decades at multiple northern peatlands, have shown a large weather-driven interannual variability from weak C sources to strong C sinks, as a response to hydrological and temperature conditions (Z. Yu et al., 2011). Despite large interannual variations, site averages converge around 20–30 g C m^{-2} yr^{-1}, with an overall mean modelled net C balance of 25 (±31) g C m^{-2} yr^{-1}. Accumulation rates calculated for all the sites studied here, had higher average accumulation rates than before mentioned results.

Data synthesis of peatland dynamics since the Last Glacial Maximum, reported highest rates of C accumulation (~25 g C m^{-2} yr^{-1}) in northern peatlands during early Holocene (Z. Yu et al., 2010). This was likely due to maximum summer insolation and the greatest seasonality in insolation and climate

at that time. These results are supported by another database synthesis covering the whole Holocene, on basis of 151 peat cores from 127 sites (located north of 45 °N). It reported that highest rates of C accumulation (25–28 g C m^{-2} yr^{-1}) were recorded during the early Holocene (Loisel et al., 2014). However, Treat et al. (2016) separated samples that were classified into environmental class of "tundra permafrost peatland" and calculated median C accumulation rate for samples older than 1000 years. They reported median C accumulation rate of 108 g C m^{-2} yr^{-1}. After the maximum peak rate, C accumulation during the mid- and late Holocene declined. No estimates on how large percentage of recently accumulated C at the study sites will become part of the long-term C store were carried out here. However, results indicate that changes in the declining trend reported by the long-term studies, could be taking place.

Some efforts to study long term trends of C accumulation and estimation of soil C stocks at Svalbard have been taken. Peat cores covering the active layer were collected and dated from moss tundra area of Stuphallet in 2011 AD, approximately 100 km to northwest from the study area of this thesis (Nakatsubo et al., 2015). Average thickness of active layer was reported to be 28 centimetres with permafrost layer present below. Dated bottom ages of active layer varied between 701 to 81 BP cal. The long-term apparent C accumulation rate estimates ranged between 9.0 to 19.2 g C m^{-2} yr^{-1}. A single permafrost layer from Stuphallet (depth of 103.7 –105 centimetres) has been dated to 5710 ± 150 BP by Rozema et al. (2006). They also dated segments of tundra peat cores collected from Ny Ålesund, Stuphallet, Blomstrand and Isdammen. Respectively, obtained calibrated ^{14}C dates for the profile bottom samples were 350–490 BP, 5710 BP, 4670 BP and 700–900 BP. Showing large site-specific variation of bottom ages. Notably, none of these bottom ages place in the most recent centuries, diverging from results obtained from most sites in this thesis.

Colony of seabirds nesting nearby Stuphallet sampling sites, was recognised as an important factor affecting nutrient supply area (Nakatsubo et al., 2015). Conveying information alike to samples collected from Alkehornet (average profile depth 24.4 cm, nutrition supply dispensed by bird colonies and organic matter continuing below permafrost boundary). Fertilizing effect of the sea bird colony at Alkehornet was noticeable in N content measurements, as they depict clearly higher percentual content than samples from other sites (Table 3). This eminent nutrition supply together with position on southwards opening ridge (higher insolation than other sites), could partly be responsible why this environment has been suitable for initiation of organic matter accumulation much earlier than the other study sites. In terms of current soil C stocks in Svalbard as a whole, efforts towards extensive spatial upscaling has been carried out (Weiss et al., 2017; Wojcik et al., 2019). Altogether, permafrost

soil organic C storage in 0- to 1-meter depth at unglaciated areas of Spitsbergen island has been estimated to be 105 Tg, with an average of 6.26 ± 1.47 kg C m^{-2} (Weiss et al., 2017).

As soil C accumulation is a balance between assimilation rate and decomposition rate, changes in factors controlling these processes likely impact the accumulation rates. Strong increasing trend in annual average temperatures and precipitation at the study area was observed (Figure 9). Virtually all biogeochemical reactions are dependent on thermal activation and proceed more rapidly at higher temperatures (Petrucci et al., 2007). Thus, prevailing surface temperatures significantly affects rates in which these processes advance. Simultaneously, temperature rise during the summer months elongates the growing season (Le Quéré et al., 2016). Modelled results for 1961 AD to 2012 AD period, reported that snow onset date has been delayed by two days per decade in response to autumn warming (van Pelt et al., 2016). Non-significant ($p>0.1$) trend in springtime snow disappearance of 0.7 days per decade was reported. Longer snow free periods and warmer summers are associated with greater soil mineralization and higher nutrient turnover (Aerts et al., 2006; Albon et al., 2017; Barber et al., 2009). Simultaneous increase in atmospheric CO_2 concentration is predicted to have a fertilizing effect on flora. During 2002 to 2011 period, rise in atmospheric CO_2 concentrations were 2.0 ± 0.1 ppm annually (Field et al., 2014). Together with changing climate, regional factors affecting moisture conditions and nutrition supply, have had influence on the C accumulation rates and potential initiation of paludification at the younger sites.

Regional factors hypothesized to affect recent apparent C accumulation rates of the study sites, were fertilizing sea bird colonies, grazing reindeers and concomitant fertilizing effect, and glacier meltwaters with fine grainsized rock flour. It is feasible to deduct that these changes have affected the flora and soil C accumulation rates during the study period (Albon et al., 2017; Gąsiorowski, 2019; Gunnarsen et al., 2019; Hodgkins et al., 2009; Le Moullec et al., 2019). Effects of bird colonies could be differentiated from the data. Fertilizing effect of reindeer faecal pellets is probable, but the fact that they were present at every study site, prevented comparison between the sites. However, experimental study at 12 study locations across the Scandinavian mountains, showed that soil mineral N content were almost twice as high in areas where reindeers grazed, then at areas with no grazing reindeer (Sundqvist et al., 2019). No difference in soil phosphorus content were noted between areas. Also, it has been proposed that plant response to nutrient addition at subarctic tundra is not consistent but differs along elevation gradients and vegetation types (Sundqvist et al., 2014). Hansen et al. (2007) studied vegetation changes through a 26 years long period, following Svalbard reindeer population that was not subjected to predation. A population was introduced to an area free from

reindeers. This had strong trophic top-down effects on the vegetation, as they have a varied diet and eat almost all types of vegetation. Long-term faecal accumulation acts as N fertilization. Still, areas with moss, vascular plant or lichen cover declined. Previously dominant fruticose lichens were almost depleted. During the study, population number crashed during one winter with strong resource limitation due to ground icing. Even after the population crash, lichens showed no signs of recovery. This indirectly effected recovery rates of other plant groups after the crash. Mosses recovered completely and even exceeded pre-reindeer levels. Contrary, it has been suggested that increase in reindeer population, rises grazing pressure and this could lead to increased productivity of the tundra vegetation (Albon et al., 2017). Grazing reduces thickness of the moss layer, which in turn, can lead to increase in soil temperature. Higher temperature enhances soil mineralization and nutrient turnover, possibly leading to increased plant productivity. Recent reindeer abundance estimates for Svalbard are the largest ever recorded with a mean of population size estimates of 22,435 (Le Moullec et al., 2019). Total population size estimates from which the mean value was calculated, withheld estimates 13 times higher than the minimum estimates from the late 1950s, and twice as high as an estimate based on counts between 1969–2008. Considerable population development during the study period, supports deduction of grazing reindeers' possible fertilizing effect at the study sites.

In addition to biotic nutrition sources, decline of glaciers of western Svalbard during recent decades, may have provided source of mineral material rich in macronutrients for the study sites (Bourgeois et al., 2016; Gunnarsen et al., 2019). Glacial movement results in bedrock abrasion, producing fine-grained rock flour with high reactivity. Simultaneously, retreating glaciers reveal bare soil susceptible for erosion. This material is often deposited to proglacial areas (Hodgkins et al., 2009). All the study sites are located so that meltwaters originating from glaciers at higher elevations, are likely to affect them. In addition, local environmental conditions and individual characteristics of every study site should not be neglected, as the mixed modelling results also suggested (Table 9).

In summary, an increasing trend in recent apparent soil C accumulation rates was observed at inner fjord areas of Svalbard. Regional factors and processes that have potentially influenced local C dynamics jointly with changing climate were identified. Factors like topography, moisture conditions, nutrient supply, vegetation composition, with soil microbial communities play their role in establishing conditions beneficial for soil C accumulation at Svalbard (Adachi et al., 2006; Yoshitake et al., 2011, 2018). Interactions between these factors are presumable, as is their adjustment to the changing climate. Thus, warming trend of surface temperatures can be expected to accelerate discussed processes and continue to influence soil C accumulation rates at the study area.

8.2 NDVI timeseries, greening and recent carbon accumulation

Potential of various remote sensing methods producing data suitable to be used as proxy in C dynamics studies of organic soils has been recognized (Lees et al., 2018; Lopatin et al., 2019; McPartland et al., 2019). Still, only earth observing satellite data provides suitable, global, temporally, and spatially consistent data, covering the last decades (Fensholt et al., 2012). However, using satellite based remote sensing to directly monitor changes in below ground C stocks is still challenging, due to disturbance caused by vegetation cover (Rasel et al., 2017).

Gross portion of lower level Landsat products were successfully co-registered, topographically corrected, and composited. Method was unsuccessful with imagery suffering from large spatial shifts and distinct geometrical distortions. However, results showed that with reasonable amount of processing, lower level Landsat products (L1GS and L1GT) can be co-registered to satisfactory level, cloud masked, topographically corrected and timeseries with annual maximum value composites generated. As a remark, the methodology did not take into consideration possible errors caused by deficient terrain correction of L1GS images.

Approach selected for trend detection, resulted into gross portion of high elevation and glaciated areas being masked out. Multiple possible reasons for this exist. First, it is possible that at these areas significant changes have not happened. Secondly, annual fluctuation of snow or ice cover, could have led to insignificant Tau values. Thirdly, cloud masking process at times masks out snow-covered or glaciated areas. This again, could have led to lower availability of data from these areas. Lower availability of data, in turn, can increase the pixelwise p-values. Pixels with p-value exceeding 0.05 limit were masked out. Thus, resulting time-series presents areas where noticeable change had happened during the study period (Figure 13).

Results implicated significant positive trend in NDVI, showing average annual increase of 0.0059. Which translates to average 0.1950 increase of NDVI at the study area, during the 1985-2018 period. If compared to average maximum NDVI of the corresponding pixels, during year of 1985, this would lead to percentual increase of 99%. Negative slope values notable at riverbeds and furrows, resulted likely from variation of flowing water between acquisitions or fluvial erosion. Several central Spitsbergen valleys are strongly affected by erosion and accumulation processes (Elvebakk, 2005). Flooding and aeolian sand silt transportation alter the valley floors. Resulting in forming of perennial mud flats and instable areas covered by pioneer vegetation. Areas with instable trends, were

predisposed to being masked out by Kendall Tau filtering. Negative values at high altitude areas, were likely not caused by declining vegetation at these areas, rather its an outcome of snow and ice cover producing negative NDVI values. However, significant greening trend was observed virtually at all low-lying areas. These observations indicate increased vegetation productivity across the study area. Simultaneously, mean annual temperature data showed most rapid increase during the period in which the remote sensing data covers. Rozema et al. (2006) focused on vegetation, climate and environment reconstruction based on peat cores collected from multiple sites at Svalbard. In this study an undated peat core with length of 19 centimetres was collected near Longyearbyen, next to the drinking water reservoir Isdammen, located within eastern section of the area covered by remote sensing data of this thesis (Figure 13). Surprisingly, they reported that the profile pollen record seemed stable during the recent past, not showing clear changes in vegetation composition and suggesting dry and nutrient poor tundra environment.

Additionally, NDVI's suitability as s proxy for vegetation productivity solely was assessed. Mixed model results showed strong positive effects, but explanatory power of the models was weak and confidence interval ranges large. Therefore, actual strength of the effect could not be stated. NDVI was used as a proxy for GPP, neglecting changes in other factors possibly affecting NPP and C accumulation rates. NDVI is strongly tied to the vegetation type of the study area. At many areas NDVI includes contributions from both mosses and vascular plants covering the soil. However, for the same NDVI response, moss can generate only about one third of the GPP that vascular plants can, due to much lower photosynthetic capacity (W. Yuan et al., 2014). This variation could have hampered performance of the models. In addition, processes regulating C accumulation rates, like litter degradability, pH, ER variation, changes in water table levels, erosion and exportation of organic material, biochemical processes in the soil were not taken into consideration (Limpens et al., 2008), since most of these factors cannot be detected by NDVI. Comparable efforts quantify decades long NDVI timeseries and soil C accumulation rates have not been previously conducted.

Alike approaches to identify changes or trends in landcover and vegetation, with linear regression slopes has been used successfully in other studies (Fensholt et al., 2012; Fensholt & Proud, 2012; Xiaoyi Guo et al., 2017). Vickers et al. (2016) studied greening at Isfjord area during the 1986-2015 period, using maximum-value NDVI derived from AVHRR series of satellites (spatial resolution of 1 kilometre), at areas where pixelwise average NDVI values were above 0.2 during their study period. Thus, possibly masking out areas where vegetation succession might have advanced during latter part of their study period. To account for years with outlier maximum NDVI values, for all possible pairs

of years, they removed the corresponding temperature and maximum NDVI values. This sequential subsetting was conducted to identify which pair of years, when removed from the dataset, produced the best correlation between mean summer temperature and maximum NDVI. They detected average increase of 29% for the whole dataset and increase 59% for the best fit subset timeseries. Thus, supporting results of significant rising trend at the area. Still, large differences in scale of the change between studies exists. Results are not directly comparable due to differences in study period, spatial resolution, and basis of pixelwise masking. Method presented here took into consideration plant composition changes without average NDVI limitations, thus possible succession at areas with previously non or minor vegetation was more likely observed. Also, no attempts to remove outlier values were taken, as the Mann-Kendall rank correlation used for masking is not as strongly affected by the weight of extreme values as many other correlation tests.

In summary, results suggested that NDVI is useful in detecting spatiotemporal patterns of vegetation composition change, however this information cannot be used directly to estimate soil C accumulation rates. Complex relationships with multiple environmental factors govern the soil C accumulation rates, and here no other factors than NDVI as presentative of GPP was taken into consideration. Thus, these results do not imply that NDVI could not be successfully used as an input variable of more robust modelling structures.

8.3 Potential error sources

This thesis combined highly technical methods, from the fields of palaeoecology and remote sensing (Figure 16). Utmost caution was followed when treating the soil samples at all stages, and precautions taken to reduce possible error sources disturbing remote sensing data. To mitigate possible humane error sources high precision demanding stages of laboratory work concerning dating methods, were conducted under supervision. Soil profile segments were dated with resolution of one centimetre. This is high precision compared to many palaeoecological studies. However, discrepancy of temporal resolution between soil C accumulation rates and annual maximum NDVI values complicated joining the datasets.

Lowest organic layers were determined visually due to schedule imposed by reserved sample dating. Due to expenses, dating of multiple samples from deep layers of every profile was not possible. Large variation in the organic matter content of the bottom samples was noted, pointing to differences in the stages of potential paludification process between the samples. Nevertheless, extensive view of C

accumulation history was obtained through age-depth modelling. Bacon age-depth modelling results were not compared to other methods, which could have strengthened the reliability of obtained results. However, performance comparison of five novel age-depth modelling methods (including Bacon) stated that all the models yielded comparable results for recent accumulation histories (Sikorski, 2019).

Age-depth modelling results included segments with thousands of years old bottom ages, showing rapid increase in organic matter accumulation rates when approaching modern times (Alk.4 and Alk.7 profiles). These results might partly suffer from the fact, that accumulation rates of recently formed peat cannot be reliably compared older, deeper, peat layers (D. M. Young et al., 2019). As the newly added litter has not had time to fully decompose, and eventually only part of it will become part of the long-term C store. As emphasis here was solely put on the recent changes, this potential bias did not require consideration.

Insufficient ground control points have hindered reliable geo-registration of Landsat acquisitions at high latitudes (Dwyer, 2019). High cloud cover and the relatively short growing season of the study area, limited availability of cloudless acquisitions recorded during growing season. Also, topographical alteration is large at the study area, and sun elevation angle stays relatively low even in the summer months. These two variables can limit success rate of atmospheric correction, required to process surface reflectance data products (United States Geological Survey, n.d.-b, 2019c, 2019b). Semi-automated methodology was presented to bypass these problems at least partly, with co-

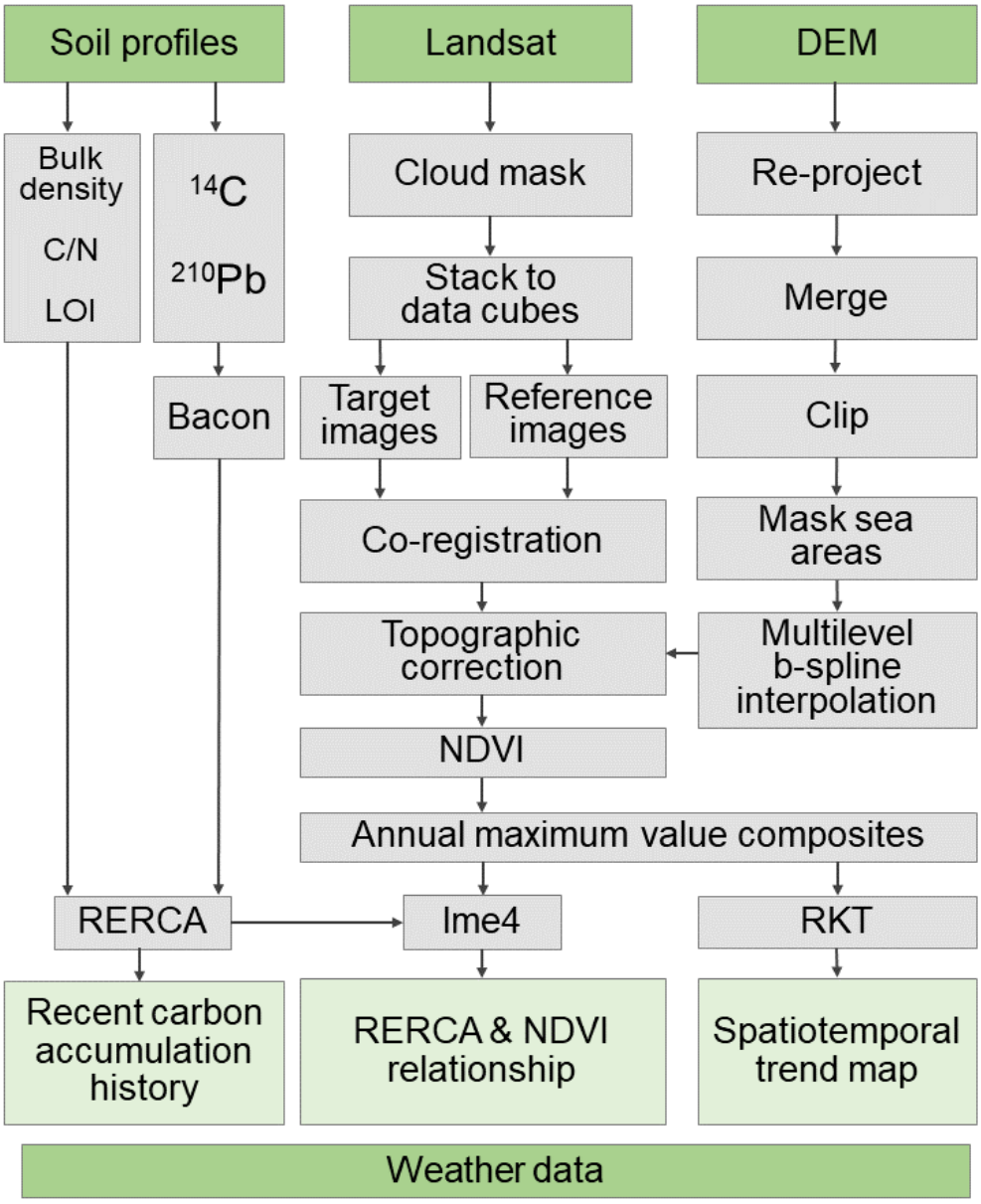

Figure 16. Summary of workflow steps of this thesis simplified and summarised. Dark green textboxes depict initial data sources. Grey textboxes depict processing steps. Light-green textboxes depict analysis results. Abbreviation used in the figure: digital elevation model (DEM), carbon and nitrogen measurements (C/N), loss on ignition (LOI), radiocarbon dating (^{14}C), lead dating (^{210}Pb), normalized difference vegetation index (NDVI), recent apparent carbon accumulation rates (RERCA), Linear Mixed-Effects Models using 'Eigen' and S4 - package (lme4) and Seasonal and Regional Kendall Tests (RKT).

registration as a significant step. AROSICS co-registration performance was not compared with other solutions. However, a study where Landsat 8 and Sentinel 2 -imagery where co-registered using AROSICS, computed mean RMSE of 3.4 ± 1.3 metres in xy-coordinates (Stumpf et al., 2018). Supporting selection of AROSICs as a valid option performing well in co-registration of multi-temporal datasets.

Sufficiency of image pool size used in this study can be questioned. Years with no or only one annual NDVI raster available were present. Thus, it is likely that the actual annual maximum NDVI was not recorded for multiple years during study period. Larger image pool of time series analysis ready data would have raised reliability and enabled calculation of study area specific sensor correction coefficients. Average NDVI Values for the study area showed considerable increase at year 2013, just when Landsat 8 sensor data becomes available. More frequent availability of images could have bettered detection of actual NDVI maximum peak, or this could be caused by a defect in the sensor cross calibration. As an example of extensive data pool, Chávez et al. (2019) provided first digital peatland inventory and multiscale productivity assessment for the Chilean Altiplano (63,705 km^2), using 31 years of Landsat data with 8997 acquisition scenes. Soon constraints of time series analysis ready Landsat data also at high-latitudes could be largely removed, as Landsat Collection 2 is released (United States Geological Survey, n.d.-a). Several processing, geometric, and radiometric improvements are promised. Until then, end-users must rely on external processing steps. Processing large image collections that meet these requirements demand significant data storage capacity and high computational power (Azzari & Lobell, 2017). To answer these needs, cloud computing platforms that have direct access to remote sensing data, now enables large spatial-scale multitemporal ground cover classification and environmental monitoring at all locations on earth where time series analysis ready data is available (M. C. Hansen et al., 2013; Mahdianpari et al., 2018; Tian et al., 2020).

Data scarcity likely affected which areas were masked out in the trend detection phase and results from these areas (Figure 13). At areas with lower quantity of data, even a small number of notably low values could have distorted the potential trends. It has been noted that these results can be confound by other environmental (i.e. soil moisture) and anthropogenic factors (i.e. agriculture and increase of impermeable surfaces) (Ahmed et al., 2017; Raynolds & Walker, 2016; Wen et al., 2017). Increase in quantity of water may be masking increases in vegetation, when using the water sensitive NDVI. This could be a credible error source in the analysis. Since at Svalbard topography causes large variation in snow cover, ground temperature and permafrost thickness, which can all play a role

in local moisture conditions (Cooper et al., 2011; Humlum et al., 2003). Minor quantity of pixels with negative slope values were recorded at high altitudes, near waterbodies and at valley floors. These observations were assumed to originate from variations in snow cover at the high altitudes, quantity of water in streams and stored in water bodies (moving shoreline of water bodies) and erosion. Also, drought can notably affect the reflectance values recorded from mosses covering the ground (Harris, 2008; W. Yuan et al., 2014). Use of annual maximum NDVI compositing, should reduce effects of momentary changes in soil moisture. However, previously stated insufficiency of image pool could have lowered the success rate of this approach.

As portion of the annual composites did not cover the whole study area. This increased count of NA values when compiling soil-profile wise timeseries. However, use of three-year moving window averaging of the profile-wise NDVI values, enabled finding a comparable pair for every C accumulation rate estimate between 1985 AD and 2018 AD. This did not remove the fact that, some soil profiles had only 1 or 2 pairwise observations of NDVI and annual average C accumulation rates. Which heavily impacted performance of the linear mixed effects model.

9. Conclusions

Knowledge of soil C stocks located at high-latitude permafrost regions and their response to climate change is still deficient. This thesis brought together information of recent C accumulation history of organic soils, climate history and vegetation succession at four moss tundra sites in Svalbard, Norway. As Svalbard was affected by “Little ice age” till 1900 AD, focus was set on changes taken place later than this. Dataset of soil properties and accumulation histories of 15 soil profiles were successfully compiled. Averages of multiple profiles were used to exclude the influence intra-site variation in accumulation rates, thus separating the genuine regional effect of changing climate.

Increase of annual average temperatures greater than the global average rate, accompanied with increase in precipitation was noted at the study area. Significant changes in vegetation composition and productivity has taken place, associated with increase in recent soil C accumulation rates. This is suggesting that ecosystems at Svalbard are experiencing rapid ecological change, due to forcing imposed by climate change. NDVI indices revealed clear patterns in spatiotemporal development of vegetation composition and productivity. Greening trend was notable virtually at all valleys and low-lying areas. However, information derived from indices, could not reliably explain spatiotemporal

variation in soil C accumulation rates, suggesting that NDVI indicates variations in fPAR but is not a good proxy of NPP at high-latitude moss tundra areas.

Climate change and regionally impacting factors in synergy have increased organic matter and C accumulation rates at Svalbard's moss tundra areas, pointing to potential onset of paludification process. This is emphasizing potential significance of high-latitude moss tundra areas in regards of soil C sequestration. Spatiotemporal heterogeneity of C transformation and transfer processes still impose large challenges for C-cycle modelling. To alleviate this problem, representative data from wider range of environmental conditions needs to be covered. Constantly developing remote sensing products offer data sources for method development concerning upscaling and estimation of soil-atmosphere C fluxes. More efforts towards synergetic use of field sampling and remote sensing are needed to further predictions of Arctic soil C pools response to climate change.

10. Acknowledgements

This Master's Thesis was brought forth as a part of a larger research project: Response of high-latitude peatlands to past and recent warming - predictions for future climate feedbacks. I want to thank the project manager and my first supervisor Minna Väliranta for the opportunity and guidance throughout the project. I express my gratitude for my supervisor Miska Luoto, for valuable guidance regarding spatiotemporal statistical methods. I also want to thank Sanna Piilo and Teemu Juselius for providing help and guidance in soil profile sample analysis. Lastly, I want to thank my friends, family, and partner for their unceasing support.

Portion of soil profile samples were dated at the University of Exeter. For travel purposes, a grant was admitted by the master's programme of Geography at the University of Helsinki. Thank you.

11. References

"4 per 1000" Initiative. (2018). *4 per 1000 Initiative*. 4p1000.Org. https://www.4p1000.org/

Adachi, M., Ohtsuka, T., Nakatsubo, T., & Koizumi, H. (2006). The methane flux along topographical gradients on a glacier foreland in the High Arctic, Ny-Ålesund, Svalbard. *Polar Bioscience*, *20*, 9.

Aerts, R., Cornelissen, J. H. C., & Dorrepaal, E. (2006). Plant performance in a warmer world: General responses of plants from cold, northern biomes and the importance of winter and spring events. In Jelte Rozema, R. Aerts, & H. Cornelissen (Eds.), *Plants and Climate Change* (Vol. 41, pp. 65–78). Springer Netherlands. https://doi.org/10.1007/978-1-4020-4443-4_5

Ahmed, M., Else, B., Eklundh, L., Ardö, J., & Seaquist, J. (2017). Dynamic response of NDVI to soil moisture variations during different hydrological regimes in the Sahel region. *International Journal of Remote Sensing*, *38*(19), 5408–5429. https://doi.org/10.1080/01431161.2017.1339920

Akaike, H. (1974). A new look at the statistical model identification. *IEEE Transactions on Automatic Control*, *19*(6), 716–723. https://doi.org/10.1109/TAC.1974.1100705

Albon, S. D., Irvine, R. Justin., Halvorsen, O., Langvatn, R., Loe, L. E., Ropstad, E., Veiberg, V., Wal, R., Bjørkvoll, E. M., Duff, E. I., Hansen, B. B., Lee, A. M., Tveraa, T., & Stien, A. (2017). Contrasting effects of summer and winter warming on body mass explain population dynamics in a food-limited Arctic herbivore. *Global Change Biology*, *23*(4), 1374–1389. https://doi.org/10.1111/gcb.13435

Alm, J., Shurpali, N. J., Tuittila, E.-S., Laurila, T., Maljanen, M., Saarnio, S., & Minkkinen, K. (2007). *Methods for determining emission factors for the use of peat and peatlands—Flux measurements and modelling*. *12*, 17.

Anaconda Software Distribution. (2016). *Anaconda, Computer software* (Version 2019.10) [Computer software]. https://anaconda.com

Andrejko, M., Fiene, F., & Cohen, A. (1983). Comparison of Ashing Techniques for Determination of the Inorganic Content of Peats. In P. Jarrett (Ed.), *Testing of Peats and Organic Soils* (pp. 5–20). ASTM International. https://doi.org/10.1520/STP37331S

Appleby', P. G., & Oldfield, F. (1983). The assessment of 210Pb data from sites with varying sediment accumulation rates. *Hydrobiologia Volume*, *103*, 7.

Azzari, G., & Lobell, D. B. (2017). Landsat-based classification in the cloud: An opportunity for a paradigm shift in land cover monitoring. *Remote Sensing of Environment; Big Remotely Sensed Data: Tools, Applications and Experiences*, *202*, 64–74. https://doi.org///doi.org/10.1016/j.rse.2017.05.025

Baniya, B., Tang, Q., Huang, Z., Sun, S., & Techato, K. (2018). Spatial and Temporal Variation of NDVI in Response to Climate Change and the Implication for Carbon Dynamics in Nepal. *Forests*, *9*(6), 329. https://doi.org/10.3390/f9060329

Barba, J., Cueva, A., Bahn, M., Barron-Gafford, G. A., Bond-Lamberty, B., Hanson, P. J., Jaimes, A., Kulmala, L., Pumpanen, J., Scott, R. L., Wohlfahrt, G., & Vargas, R. (2018). Comparing ecosystem and soil respiration: Review and key challenges of tower-based and soil measurements. *Agricultural and Forest Meteorology*, *249*, 434–443. https://doi.org/10.1016/j.agrformet.2017.10.028

Barber, D. G., Lukovich, J. V., Keogak, J., Baryluk, S., Fortier, L., & Henry, G. H. R. (2009). The Changing Climate of the Arctic. *ARCTIC*, *61*(5), 7–26. https://doi.org/10.14430/arctic98

Bates, D., Mächler, M., Bolker, B., & Walker, S. (2015). Fitting Linear Mixed-Effects Models Using lme4. *Journal of Statistical Software*, *67*(1). https://doi.org/10.18637/jss.v067.i01

Blaauw, M., Christen, J. A., & Aquino, L. (2020). *rbacon: Age-Depth Modelling using Bayesian Statistics* (Version 2.4.1) [Computer software]. https://CRAN.R-project.org/package=rbacon

Boike, J., Juszak, I., Lange, S., Chadburn, S., Burke, E., Overduin, P. P., Roth, K., Ippisch, O., Bornemann, N., Stern, L., Gouttevin, I., Hauber, E., & Westermann, S. (2018). A 20-year record (1998–2017) of permafrost, active layer and meteorological conditions at a high Arctic permafrost research site (Bayelva, Spitsbergen). *Earth System Science Data*, *10*(1), 355–390. https://doi.org/10.5194/essd-10-355-2018

Bolker, B. M., Brooks, M. E., Clark, C. J., Geange, S. W., Poulsen, J. R., Stevens, M. H. H., & White, J.-S. S. (2009). Generalized linear mixed models: A practical guide for ecology and evolution. *Trends in Ecology & Evolution*, *24*(3), 127–135. https://doi.org/10.1016/j.tree.2008.10.008

Bourgeois, S., Kerhervé, P., Calleja, M. Ll., Many, G., & Morata, N. (2016). Glacier inputs influence organic matter composition and prokaryotic distribution in a high Arctic fjord (Kongsfjorden, Svalbard). *Journal of Marine Systems*, *164*, 112–127. https://doi.org/10.1016/j.jmarsys.2016.08.009

Chambers, F. M., Beilman, D. W., & Yu, Z. (2011). *Methods for determining peat humification and for quantifying peat bulk density, organic matter and carbon content for palaeostudies of climate and peatland carbon dynamics*. 10.

Charman, D.J., Beilman, D.W., Blaauw, M., Booth, R.K., Brewer, S., Chambers, F.M., Christen, J.A., Gallego-Sala, A., Harrison, S.P., Hughes, P.D.M., Jackson, S.T., Korhola, A., Mauquoy, D., Mitchell, F.J.G., Prentice, I.C., Linden, M. van der, Vleeschouwer, F.D., Yu, Z.C., Alm, J., Bauer, I.E., Corish, Y.M.C., Garneau, M., Hohl, V., Huang, Y., Karofeld, E., Roux, G.L., Loisel, J., Moschen, R., Nichols, J.E., Nieminen, T.M., MacDonald, G.M., Phadtare, N.R., Rausch, N., Sillasoo, U., Swindles, G.T., Tuittila, E.-S., Ukonmaanaho, L., Valiranta, M., Bellen, S. van, Geel, B. van, Vitt, D.H., Zhao, Y. (2013). *Climate-related changes in peatland carbon accumulation during the last millennium*. http://hdl.handle.net/10138/165312

Chávez, R. O., Christie, D. A., Olea, M., & Anderson, T. G. (2019). A Multiscale Productivity Assessment of High Andean Peatlands across the Chilean Altiplano Using 31 Years of Landsat Imagery. *Remote Sensing*, *11*(24), 2955. https://doi.org/10.3390/rs11242955

Chen, P.-Y., Srinivasan, R., Fedosejevs, G., & Kiniry, J. R. (2003). Evaluating different NDVI composite techniques using NOAA-14 AVHRR data. *International Journal of Remote Sensing*, *24*(17), 3403–3412. https://doi.org/10.1080/0143116021000021279

Christen, J. A., & Fox, C. (2010). A general purpose sampling algorithm for continuous distributions (the t-walk). *Bayesian Analysis*, *5*(2), 263–281. https://doi.org/10.1214/10-BA603

Christensen, T., Barry, T., Taylor, J. J., Doyle, M., Aronsson, M., Braa, J., Burns, C., Coon, C., Coulson, S., Cuyler, C., Falk, K., Heiðmarsson, S., Kulmala, P., Lawler, J., MacNearney, D., Ravolainen, V., Smith, P. A., Soloviev, M., & Schmidt, N. M. (2020). Developing a circumpolar programme for the monitoring of Arctic terrestrial biodiversity. *Ambio*, *49*(3), 655–665. https://doi.org/10.1007/s13280-019-01311-w

Civco, D. (1989). Topographic Normalization of Landsat Thematic Mapper Digital Imagery. *Photogrammetric Engineering and Remote Sensing*, *55*(9), 1303–1309.

Clymo, R. S. (1965). Experiments on Breakdown of Sphagnum in Two Bogs. *The Journal of Ecology*, *53*(3), 747. https://doi.org/10.2307/2257633

Clymo R.S. (1998). Sphagnum, the peatland carbon economy, and climate change. In Bates J.W., Ashton N.W., Duckett J.G. (Ed.), *Bryology for the Twenty-First Century* (pp. 361–368). Maney Publishing Company and The British Bryological Society. http://research.sbcs.qmul.ac.uk/r.clymo/Clymo-article-PDFs/57-Clymo-1998-Sphagnum-and-climate-change.pdf

Cnaan, A., Laird, N.M. & Slasor, P. (1997), Using the general linear mixed model to analyse unbalanced repeated measures and longitudinal data. *Statistics in Medicine*., 16, 2349-2380. https://doi.org/10.1002/(SICI)1097-0258(19971030)16:20%3C2349::AID-SIM667%3E3.0.CO;2-E

COAT. (2020). *Climate-ecological Observatory for Arctic Tundra (COAT)*. https://www.coat.no/en/

Cooper, E. J., Dullinger, S., & Semenchuk, P. (2011). Late snowmelt delays plant development and results in lower reproductive success in the High Arctic. *Plant Science*, *180*(1), 157–167. https://doi.org/10.1016/j.plantsci.2010.09.005

de Paul Obade, V. (2013). Assessing land cover and soil quality by remote sensing and geographical information systems (GIS) (V. de Paul Obade & R. Lal, Trans.). *Catena, v. 104*, 77–92. PubAg. https://doi.org/10.1016/j.catena.2012.10.014

Descamps, S., Aars, J., Fuglei, E., Kovacs, K. M., Lydersen, C., Pavlova, O., Pedersen, Å. Ø., Ravolainen, V., & Strøm, H. (2017). Climate change impacts on wildlife in a High Arctic Archipelago—Svalbard, Norway. *Global Change Biology*, *23*(2), 490–502. https://doi.org/10.1111/gcb.13381

Dwyer, J. L. (2019). *Landsat Collection 1 Level 1 Product Definition*. 32.

Elvebakk, A. (2005). A vegetation map of Svalbard on the scale 1:3.5 mill. *Phytocoenologia*, *35*(4), 951–967. https://doi.org/10.1127/0340-269X/2005/0035-0951

Fassnacht, F. E., Schiller, C., Kattenborn, T., Zhao, X., & Qu, J. (2019). A Landsat-based vegetation trend product of the Tibetan Plateau for the time-period 1990–2018. *Scientific Data*, *6*(1), 78. https://doi.org/10.1038/s41597-019-0075-9

Fensholt, R., Langanke, T., Rasmussen, K., Reenberg, A., Prince, S. D., Tucker, C., Scholes, R. J., Le, Q. B., Bondeau, A., Eastman, R., Epstein, H., Gaughan, A. E., Hellden, U., Mbow, C., Olsson, L., Paruelo, J., Schweitzer, C., Seaquist, J., & Wessels, K. (2012). Greenness in semi-arid areas across the globe 1981–2007—An Earth Observing Satellite based analysis of trends and drivers. *Remote Sensing of Environment*, *121*, 144–158. https://doi.org/10.1016/j.rse.2012.01.017

Fensholt, R., & Proud, S. R. (2012). Evaluation of Earth Observation based global long-term vegetation trends — Comparing GIMMS and MODIS global NDVI time series. *Remote Sensing of Environment*, *119*, 131–147. https://doi.org/10.1016/j.rse.2011.12.015

Field, C. B., Barros, V. R., & Intergovernmental Panel on Climate Change (Eds.). (2014). *Climate change 2014: Impacts, adaptation, and vulnerability: Working Group II contribution to the fifth assessment report of the Intergovernmental Panel on Climate Change*. Cambridge University Press.

Fischler, M., & Bolles, C. (1981). *Random Sample Consensus: A Paradigm for Model Fitting with Applications to Image Analysis and Automated Cartography*. *24*(6), 381–395.

Flint, R., & Deevey, E. (1962). RDC volume 4 Editorial Statement. *Radiocarbon*, *4*, f1–f6. https://doi.org/10.1017/S0033822200036675

Førland, E. J., Benestad, R., Hanssen-Bauer, I., Haugen, J. E., & Skaugen, T. E. (2011). Temperature and Precipitation Development at Svalbard 1900–2100. *Advances in Meteorology*, *2011*, 1–14. https://doi.org/10.1155/2011/893790

Gallego-Sala, A.V., Charman, D.J., Brewer, S., Page, S.E., Prentice, I.C., Friedlingstein, P., Moreton, S., Amesbury, M.J., Beilman, D.W., Björck, S., Blyakharchuk, T., Bochicchio, C., Booth, R.K., Bunbury, J., Camill, P., Carless, D., Chimner, R.A., Clifford, M., Cressey, E., Courtney-Mustaphi, C., De Vleeschouwer, F., de Jong, R., Fialkiewicz-Koziel, B., Finkelstein, S.A., Garneau, M., Githumbi, E., Hribjlan, J., Holmquist, J., Hughes, P.D.M., Jones, C., Jones, M.C., Karofeld, E., Klein, E.S., Kokfelt, U., Korhola, A., Lacourse, T., Le Roux, G., Lamentowicz, M., Large, D., Lavoie, M., Loisel, J., Mackay, H., MacDonald, G.M., Makila, M., Magnan, G., Marchant, R., Marcisz, K., Martínez Cortizas, A., Massa, C., Mathijssen, P., Mauquoy, D., Mighall, T., Mitchell, F.J.G., Moss, P., Nichols, J., Oksanen, P.O., Orme, L., Packalen, M.S., Robinson, S., Roland, T.P., Sanderson, N.K., Sannel, A.B.K., Silva-Sánchez, N., Steinberg, N., Swindles, G.T., Turner, T.E., Uglow, J., Väliranta, M., van Bellen, S., van der Linden, M., van Geel, B., Wang, G., Yu, Z., Zaragoza-Castells, J., Zhao, Y. (2018). Latitudinal limits to the predicted increase of the peatland carbon sink with warming. *Nature Climate Change*, *8*(10), 907–913. https://doi.org/10.1038/s41558-018-0271-1

Gąsiorowski, M. (2019). *Bird population changes reconstructed from isotopic signals of peat developed in a nutrient enriched tundra*. *646*, 1359–1366. https://doi.org/10.1016/j.scitotenv.2018.07.453

Goodwin, H. (1962). Half-life of Radiocarbon. *Nature*, *195*. https://doi.org/10.1038/195984a0

Gunnarsen, K. C., Jensen, L. S., Gómez-Muñoz, B., Rosing, M. T., & de Neergaard, A. (2019). Glacially abraded rock flour from Greenland: Potential for macronutrient supply to plants. *Journal of Plant Nutrition and Soil Science*, *182*(5), 846–856. https://doi.org/10.1002/jpln.201800647

Hajek, T., & Beckett, R. P. (2007). Effect of Water Content Components on Desiccation and Recovery in Sphagnum Mosses. *Annals of Botany*, *101*(1), 165–173. https://doi.org/10.1093/aob/mcm287

Hamed, K. H. (2011). The distribution of Kendall's tau for testing the significance of cross-correlation in persistent data. *Hydrological Sciences Journal*, *56*(5), 841–853. https://doi.org/10.1080/02626667.2011.586948

Hansen, B. B., Henriksen, S., Aanes, R., & Sæther, B.-E. (2007). Ungulate impact on vegetation in a two-level trophic system. *Polar Biology*, *30*(5), 549–558. https://doi.org/10.1007/s00300-006-0212-8

Hansen, M. C., Potapov, P. V., Moore, R., Hancher, M., Turubanova, S. A., Tyukavina, A., Thau, D., Stehman, S. V., Goetz, S. J., Loveland, T. R., Kommareddy, A., Egorov, A., Chini, L., Justice, C. O., & Townshend, J. R. G. (2013). High-Resolution Global Maps of 21st-Century Forest Cover Change. *Science*, *342*(6160), 850–853. https://doi.org/10.1126/science.1244693

Harris, A. (2008). Spectral reflectance and photosynthetic properties of Sphagnum mosses exposed to progressive drought. *Ecohydrology*, *1*(1), 35–42. https://doi.org/10.1002/eco.5

Hast, A., Nysjö, J., & Marchetti, A. (2013). Optimal RANSAC - Towards a Repeatable Algorithm for Finding the Optimal Set. *Journal of WSCG*, *21*, 10.

Heiri, O., Lotter, A. F., & Lemcke, G. (2001). Loss on ignition as a method for estimating organic and carbonate content in sediments: Reproducibility and comparability of results. *Journal of Paleolimnology*, *25*, 10.

Herranen, T. (2009). The sulfur concentration of peat in Finland. *Geological Survey Of Finland - Report of Peat Investigation*, *398*, 61.

Hodgkins, R. (1997). Glacier hydrology in Svalbard, Norwegian high arctic. *Quaternary Science Reviews*, *16*(9), 957–973. https://doi.org/10.1016/S0277-3791(97)00032-2

Hodgkins, R., Cooper, R., Wadham, J., & Tranter, M. (2009). The hydrology of the proglacial zone of a high-Arctic glacier (Finsterwalderbreen, Svalbard): Atmospheric and surface water fluxes. *Journal of Hydrology*, *378*(1–2), 150–160. https://doi.org/10.1016/j.jhydrol.2009.09.020

Humlum, O., Instanes, A., & Sollid, J. L. (2003). Permafrost in Svalbard: A review of research history, climatic background and engineering challenges. *Polar Research*, 25.

Intergovernmental Panel on Climate Change. (2018). *Global warming of 1.5°C*. http://www.ipcc.ch/report/sr15/

Jobbágy, E. G., & Jackson, R. B. (2000). the vertical distribution of soil organic carbon and its relation to climate and vegetation. *Ecological Applications*, *10*(2), 423–436. https://doi.org/10.1890/1051-0761(2000)010[0423:TVDOSO]2.0.CO;2

Johansen, B. E., Karlsen, S. R., & Tømmervik, H. (2012). Vegetation mapping of Svalbard utilising Landsat TM/ETM+ data. *Polar Record*, *48*(1), 47–63. https://doi.org/10.1017/S0032247411000647

Johansen, B., & Tømmervik, H. (2014). The relationship between phytomass, NDVI and vegetation communities on Svalbard. *International Journal of Applied Earth Observation and Geoinformation*, *27*, 20–30. https://doi.org/10.1016/j.jag.2013.07.001

Joosten, H., & Clarke, D. (2002). *Wise use of mires and peatlands: Background and principles including a framework for decision-making*. International Peat Society; International Mire Conservation Group.

Ju, J., & Masek, J. G. (2016). The vegetation greenness trend in Canada and US Alaska from 1984–2012 Landsat data. *Remote Sensing of Environment*, *176*, 1–16. https://doi.org///doi.org/10.1016/j.rse.2016.01.001

Jung, M. (2008). *Uncertainties of terrestrial carbon cycle modelling: Studies on gross carbon uptake of Europe*. 145.

Juselius, T., Piilo, S., Müller, M., Ravolainen, V., Zhang, H., Gallego-Sala, A. & Väliranta, M. (2020) Recent changes in carbon accumulation to organic soils in Svalbard, Norway. Manuscript in preparation.

Karlsen, S., Elvebakk, A., Høgda, K., & Grydeland, T. (2014). Spatial and Temporal Variability in the Onset of the Growing Season on Svalbard, Arctic Norway—Measured by MODIS-NDVI Satellite Data. *Remote Sensing*, *6*(9), 8088–8106. https://doi.org/10.3390/rs6098088

Kendall, M. G. (1948). *Rank correlation methods.* Griffin.

Klein, E. S., Booth, R. K., Yu, Z., Mark, B. G., & Stansell, N. D. (2013). Hydrology-mediated differential response of carbon accumulation to late Holocene climate change at two peatlands in Southcentral Alaska. Quaternary Science Reviews, 64, 61–75. https://doi.org/10.1016/j.quascirev.2012.12.013

Kutsch, W., Bahn, M., & Heinemeyer, A. (2010). *Soil Carbon Dynamics: An Integrated Methodology*. Cambridge University Press. https://doi.org/10.1017/CBO9780511711794

Lai, D. Y. F. (2009). Methane Dynamics in Northern Peatlands: A Review. *Pedosphere*, *19*, 409–421. https://doi.org/10.1016/S1002-0160(09)00003-4

Landsat Science. (n.d.). *Landsat 7*. Retrieved May 26, 2020, from https://landsat.gsfc.nasa.gov/landsat-7/

Landva, A., Korpijaakko, E., & Pheeney, P. (1983). Geotechnical Classification of Peats and Organic Soils. In P. Jarrett (Ed.), *Testing of Peats and Organic Soils* (pp. 37–51). ASTM International. https://doi.org/10.1520/STP37333S

Lara, M. J., Nitze, I., Grosse, G., Martin, P., & McGuire, A. D. (2018). Reduced arctic tundra productivity linked with landform and climate change interactions. *Scientific Reports*, *8*(1), 2345. https://doi.org/10.1038/s41598-018-20692-8

Le Moullec, M., Pedersen, Å. Ø., Stien, A., Rosvold, J., & Hansen, B. B. (2019). A century of conservation: The ongoing recovery of Svalbard reindeer. *The Journal of Wildlife Management*, *83*(8), 1676–1686. https://doi.org/10.1002/jwmg.21761

Le Quéré, C., Andrew, R. M., Canadell, J. G., Sitch, S., Korsbakken, J. I., Peters, G. P., Manning, A. C., Boden, T. A., Tans, P. P., Houghton, R. A., Keeling, R. F., Alin, S., Andrews, O. D., Anthoni, P., Barbero, L., Bopp, L., Chevallier, F., Chini, L. P., Ciais, P., Currie, K., Delire, C., Doney, S., Friedlingstein, P., Gkritzalis, T., Harris, I., Hauck, J., Haverd, V., Hoppema, M., Klein Goldewijk, K., Jain, A., Kato, E., Körtzinger, A., Landschützer, P., Lefèvre, N., Lenton, A., Lienert, S., Lombardozzi, D., Melton, J.R., Metzl, N., Millero, F., Monteiro, P., Munro, D., Nabel, J., Nakaoka, S., Brien, K., Olsen, A., Omar, A., Ono, T., Pierrot, D., Poulter, B., Rödenbeck, C., Salisbury, J., Schuster, U., Schwinger, J., Séférian, R., Skjelvan, I., Stocker, B., Sutton, A., Takahashi, T., Tian, H., Tilbrook, B., van der Laan-Luijkx, I., van der Werf, G., Viovy, N., Walker, A., Wiltshire,A. & Zaehle, S. (2016). Global Carbon Budget 2016. *Earth System Science Data*, *8*(2), 605–649. https://doi.org/10.5194/essd-8-605-2016

Lees, K. J., Quaife, T., Artz, R. R. E., Khomik, M., & Clark, J. M. (2018). *Potential for using remote sensing to estimate carbon fluxes across northern peatlands – A review* (Vol. 615). https://doi.org/10.1016/j.scitotenv.2017.09.103

Leutner, B. (2019). *Package 'RStoolbox.'* https://github.com/bleutner/RStoolbox

Limpens, J., Berendse, F., Blodau, C., Canadell, J. G., Freeman, C., Holden, J., Roulet, N., Rydin, H., & Schaepman-Strub, G. (2008). *Peatlands and the carbon cycle: From local processes to global implications – a synthesis*. 17.

Loisel, J., & Yu, Z. (2013). Recent acceleration of carbon accumulation in a boreal peatland, south central Alaska: Recent peat carbon sequestration rates. *Journal of Geophysical Research: Biogeosciences*, *118*(1), 41–53. https://doi.org/10.1029/2012JG001978

Loisel, J., Yu, Z., Beilman, D., Camill, P., Alm, J., Amesbury, M., Anderson, D., Andersson, S., Bochicchio, C., Barber, K., Belyea, L., Bunbury, J., Chambers, F., Charman, D., Vleeschouwer, F., Fiakiewicz-Kozie, B., Finkelstein, S., Gaka, M., Garneau, M., Hammarlund, D., Hinchcliffe, W., Holmquist, J., Hughes, P., Jones, M., Klein, E., Kokfelt, U., Korhola, A., Kuhry, P., Lamarre, A., Lamentowicz, M., Large, D., Lavoie, M., MacDonald, G., Magnan, G., Mäkilä, M., Mallon, G., Mathijssen, P., Mauquoy, D., McCarroll, J., Moore, T., Nichols, J., O'Reilly, B., Oksanen, P., Packalen, M., Peteet, D., Richard, P., Robinson, S., Ronkainen, T., Rundgren, M., Sannel, A.B., Tarnocai, C., Thom, T., Tuittila, E.-S., Turetsky, M., Väliranta, M., van, der L., Geel, B. van, Bellen, S. van, Vitt, D., Zhao, Y., Zhou, W. (2014). A database and synthesis of northern peatland soil properties and Holocene carbon and nitrogen accumulation. *The Holocene, 24*(9), 1028–1042. https://doi.org/10.1177/0959683614538073

Lopatin, J., Kattenborn, T., Galleguillos, M., Perez-Quezada, J. F., & Schmidtlein, S. (2019). Using aboveground vegetation attributes as proxies for mapping peatland belowground carbon stocks. *Remote Sensing of Environment*, *231*, 111217. https://doi.org/10.1016/j.rse.2019.111217

Lund, M., Lafleur, P. M., Roulet, N. T., Lindroth, A., Christensen, T. R., Aurela, M., Chojnicki, B. H., Flanagan, L. B., Humphreys, E. R., Laurila, T., Oechel, W. C., Olejnik, J., Rinne, J., Schubert, P., & Nilsson, M. B. (2010). Variability in exchange of CO2 across 12 northern peatland and tundra sites. *Global Change Biology*, *16*(9), 2436–2448. https://doi.org/10.1111/j.1365-2486.2009.02104.x

Ma, Q., Jin, H., Yu, C., & Bense, V. F. (2019). Dissolved organic carbon in permafrost regions: A review. *Science China Earth Sciences*, *62*(2), 349–364. https://doi.org/10.1007/s11430-018-9309-6

Mahdianpari, M., Salehi, B., Mohammadimanesh, F., Homayouni, S., & Gill, E. (2018). The First Wetland Inventory Map of Newfoundland at a Spatial Resolution of 10 m Using Sentinel-1 and Sentinel-2 Data on the Google Earth Engine Cloud Computing Platform. *Remote Sensing*, *11*(1), 43. https://doi.org/10.3390/rs11010043

Mäkilä, M. (2011). Carbon Accumulation In Pristine And Drained Mires. *Geological Survey of Finland, Special Paper*, *49*, 171–177.

Marchetto, A., & Marchetto, M. A. (2017). Package 'rkt.' *Technology*, *40*, 4066–4073.

Masek, J. G. (2020). *The Worldwide Reference System « Landsat Science*. https://landsat.gsfc.nasa.gov/the-worldwide-reference-system/

May, J. L., Parker, T., Unger, S., & Oberbauer, S. F. (2018). *Short term changes in moisture content drive strong changes in Normalized Difference Vegetation Index and gross primary productivity in four Arctic moss communities* (Vol. 212). https://doi.org/10.1016/j.rse.2018.04.041

McGuire, A. D., Anderson, L. G., Christensen, T. R., Dallimore, S., Guo, L., Hayes, D. J., Heimann, M., Lorenson, T. D., Macdonald, R. W., & Roulet, N. (2009). Sensitivity of the carbon cycle in the Arctic to climate change. *Ecological Monographs*, *79*(4), 523–555. https://doi.org/10.1890/08-2025.1

McLaughlin, J., & Webster, K. (2014). Effects of Climate Change on Peatlands in the Far North of Ontario, Canada: A Synthesis. *Arctic, Antarctic, and Alpine Research*, *46*(1), 84–102. https://doi.org/10.1657/1938-4246-46.1.84

McNeish, D. (2017). Small Sample Methods for Multilevel Modeling: A Colloquial Elucidation of REML and the Kenward-Roger Correction. *Multivariate Behavioral Research*, *52*(5), 661–670. https://doi.org/10.1080/00273171.2017.1344538

McPartland, M. Y., Kane, E. S., Falkowski, M. J., Kolka, R., Turetsky, M. R., Palik, B., & Montgomery, R. A. (2019). The response of boreal peatland community composition and NDVI to hydrologic change, warming, and elevated carbon dioxide. *Global Change Biology*, *25*(1), 93–107. https://doi.org/10.1111/gcb.14465

Monteith, J. L. (1977). *Climate and the efficiency of crop production in Britain*. 18.

Moore, P. D. (1987). Ecological and hydrological aspects of peat formation. *Geological Society, London, Special Publications*, *32*(1), 7. https://doi.org/10.1144/GSL.SP.1987.032.01.02

Nakagawa, S., Johnson, P. C. D., & Schielzeth, H. (2017). The coefficient of determination R2 and intra-class correlation coefficient from generalized linear mixed-effects models revisited and expanded. *Journal of the Royal Society. Interface, 14, 20170213.* https://doi.org/10.1098/rsif.2017.0213

Nakatsubo, T., Bekku, Y. S., Uchida, M., Muraoka, H., Kume, A., Ohtsuka, T., Masuzawa, T., Kanda, H., & Koizumi, H. (2005). Ecosystem development and carbon cycle on a glacier foreland in the high Arctic, Ny-Ålesund, Svalbard. *Journal of Plant Research*, *118*(3), 173–179. https://doi.org/10.1007/s10265-005-0211-9

Nakatsubo, T., Uchida, M., Sasaki, A., Kondo, M., Yoshitake, S., & Kanda, H. (2015). Carbon accumulation rate of peatland in the High Arctic, Svalbard: Implications for carbon sequestration. *Polar Science*, *9*(2), 267–275. https://doi.org/10.1016/j.polar.2014.12.002

Norwegian Meteorological Institute. (2020a). *Air temperature in Svalbard, annual mean*. URL: http://www.mosj.no/en/climate/atmosphere/temperature-precipitation.html

Norwegian Meteorological Institute. (2020b). *Precipitation in Svalbard, Hopen and Jan Mayen, annual total*. http://www.mosj.no/en/climate/atmosphere/temperature-precipitation.html

Norwegian Meteorological Institute. (2020c). *Seasonal temperatures for Svalbard Airport.* http://www.mosj.no/en/climate/atmosphere/temperature-precipitation.html

Norwegian Meteorological Institute. (2020d). *Growing degree days*. http://eklima.met.no/

Norwegian Polar Institute. (2014). *Kartdata Svalbard 1:100 000 (S100 Kartdata) / Map Data [Data set]*. https://doi.org/10.21334/npolar.2014.645336c7

Norwegian Polar Institute. (2020). *Svalbardkartet*. https://svalbardkartet.npolar.no/Html5Svb/index.html?viewer=Svalbardkartet

Nouri, H., Anderson, S., Sutton, P., Beecham, S., Nagler, P., Jarchow, C. J., & Roberts, D. A. (2017). NDVI, scale invariance and the modifiable areal unit problem: An assessment of vegetation in the Adelaide Parklands. *Science of The Total Environment*, *584–585*, 11–18. https://doi.org/10.1016/j.scitotenv.2017.01.130

Petrucci, R., Sharwood, W., Herring, G., & Madura, J. (2007). *General Chemistry: Principles & Modern Applications* (9th ed.).

Piilo, S. (2018) Study areas of Alkehornet, Colesdalen, Björndalen and Bolterdalen [photographs].

Piilo, S. R., Zhang, H., Garneau, M., Gallego-Sala, A., Amesbury, M. J., & Väliranta, M. M. (2019). Recent peat and carbon accumulation following the Little Ice Age in northwestern Québec, Canada. *Environmental Research Letters*, *14*(7), 075002. https://doi.org/10.1088/1748-9326/ab11ec

Pimple, U., Sitthi, A., Simonetti, D., Pungkul, S., Leadprathom, K., & Chidthaisong, A. (2017). Topographic Correction of Landsat TM-5 and Landsat OLI-8 Imagery to Improve the Performance of Forest Classification in the Mountainous Terrain of Northeast Thailand. *Sustainability*, *9*(2), 258. https://doi.org/10.3390/su9020258

Piotrowska, N., Blaauw, M., Mauquoy, D., & Chambers, F. M. (2011). *Constructing deposition chronologies for peat deposits using radiocarbon dating*. 15.

Pironkova, Z., Whaley, R., & Lan, K. (2018). *Time series analysis of Landsat NDVI composites with Google Earth Engine and R: User guide—Science and Research Technical Manual TM-06*. https://doi.org/10.13140/RG.2.2.16830.95040

Porter, C., Morin, P., Howat, I., Noh, M.-J., Bates, B., Peterman, K., Keesey, S., Schlenk, M., Gardiner, J., Tomko, K., Willis, M., Kelleher, C., Cloutier, M., Husby, E., Foga, S., Nakamura, H., Platson, M., Wethington, M., Williamson, C. & Bojesen, M. (2018). *ArcticDEM* [Data set]. Harvard Dataverse. https://doi.org/10.7910/DVN/OHHUKH

Post, E., Alley, R. B., Christensen, T. R., Macias-Fauria, M., Forbes, B. C., Gooseff, M. N., Iler, A., Kerby, J. T., Laidre, K. L., Mann, M. E., Olofsson, J., Stroeve, J. C., Ulmer, F., Virginia, R. A., & Wang, M. (2019). The polar regions in a 2°C warmer world. *Science Advances*, *5*(12), eaaw9883. https://doi.org/10.1126/sciadv.aaw9883

QGIS Development Team. (2020). *QGIS Geographic Information System* (Version 3.10.2) [Computer software]. http://qgis.osgeo.org/

R Core Team. (2019). *R: A Language and Environment for Statistical Computing* (Version 3.6.2) [Computer software]. R Foundation for Statistical Computing. https://www.R-project.org/

Rasel, S. M. M., Groen, T. A., Hussin, Y. A., & Diti, I. J. (2017). Proxies for soil organic carbon derived from remote sensing. *International Journal of Applied Earth Observation and Geoinformation*, *59*, 157–166. https://doi.org/10.1016/j.jag.2017.03.004

Raynolds, M. K., & Walker, D. A. (2016). Increased wetness confounds Landsat-derived NDVI trends in the central Alaska North Slope region, 1985–2011. *Environmental Research Letters*, *11*(8), 085004. https://doi.org/10.1088/1748-9326/11/8/085004

Reichstein, M., Bahn, M., Mahecha, M. D., Kattge, J., & Baldocchi, D. D. (2014). Linking plant and ecosystem functional biogeography. *Proceedings of the National Academy of Sciences*, *111*(38), 13697–13702. https://doi.org/10.1073/pnas.1216065111

Reimer, P.J., Bard, E., Bayliss, A., Beck, J.W., Blackwell, P.G., Ramsey, C.B., Buck, C.E., Cheng, H., Edwards, R.L., Friedrich, M., Grootes, P.M., Guilderson, T.P., Haflidason, H., Hajdas, I., Hatté, C., Heaton, T.J., Hoffmann, D.L., Hogg, A.G., Hughen, K.A., Kaiser, K.F., Kromer, B., Manning, S.W., Niu, M., Reimer, R.W., Richards, D.A., Scott, E.M., Southon, J.R., Staff, R.A., Turney, C.S.M., van der Plicht, J. (2013). IntCal13 and Marine13 Radiocarbon Age Calibration Curves 0–50,000 Years cal BP. *Radiocarbon*, *55*(4), 1869–1887. https://doi.org/10.2458/azu_js_rc.55.16947

Rennermalm, A. K., Nordbotten, J. M., & Wood, E. F. (2010). Hydrologic variability and its influence on long-term peat dynamics. *Water Resources Research*, *46*(12). https://doi.org/10.1029/2009WR008242

Riano, D., Chuvieco, E., Salas, J., & Aguado, I. (2003). Assessment of different topographic corrections in landsat-TM data for mapping vegetation types (2003). *IEEE Transactions on Geoscience and Remote Sensing*, *41*(5), 1056–1061. https://doi.org/10.1109/TGRS.2003.811693

Robert J. Hijmans. (2020). *raster: Geographic Data Analysis and Modeling* (Manual R package version 2.8-4). https://CRAN.R-project.org/package=raster

Rouse, J. W., Haas, R. H., Schell, J. A., Deering, D. W., & Harlan, J. C. (1974). *Monitoring the vernal advancement and retrogradation (greenwave effect) of natural vegetation* [Technical report]. NASA. https://ntrs.nasa.gov/archive/nasa/casi.ntrs.nasa.gov/19750020419.pdf

Rozema, J., Boelen, P., Doorenbosch, M., Bohncke, S., Blokker, P., Boekel, C., Broekman, R. A., & Konert, M. (2006). A vegetation, climate and environment reconstruction based on palynological analyses of high arctic tundra peat cores (5000–6000 years BP) from Svalbard. In Jelte Rozema, R. Aerts, & H. Cornelissen (Eds.), *Plants and Climate Change*, 41, 155–174. Springer Netherlands. https://doi.org/10.1007/978-1-4020-4443-4_11

Rydin, H., Jeglum, J. K., & Hooijer, A. (2006). *The Biology of Peatlands*. Oxford University Press, Oxford. https://doi.org/10.1093/acprof:oso/9780198528722.001.0001

Santin-Janin, H., Garel, M., Chapuis, J.-L., & Pontier, D. (2009). Assessing the performance of NDVI as a proxy for plant biomass using non-linear models: A case study on the Kerguelen archipelago. *Polar Biology*, *32*(6), 861–871. https://doi.org/10.1007/s00300-009-0586-5

Scheffler, D., Hollstein, A., Diedrich, H., Segl, K., & Hostert, P. (2017). AROSICS: An Automated and Robust Open-Source Image Co-Registration Software for Multi-Sensor Satellite Data. *Remote Sensing*, *9*(7), 676. https://doi.org/10.3390/rs9070676

Scholze, M., Buchwitz, M., Dorigo, W., Guanter, L., & Quegan, S. (2017). Reviews and syntheses: Systematic Earth observations for use in terrestrial carbon cycle data assimilation systems. *Biogeosciences*, *14*(14), 3401–3429. https://doi.org/10.5194/bg-14-3401-2017

Schwarz, G. (1978). Estimating the Dimension of a Model. *The Annals of Statistics*, *6*(2), 461–464.

Sihi, D., Inglett, P. W., Gerber, S., & Inglett, K. S. (2018). Rate of warming affects temperature sensitivity of anaerobic peat decomposition and greenhouse gas production. *Global Change Biology*, *24*(1), 259–274. https://doi.org/10.1111/gcb.13839

Sikorski, J. (2019). A new method for constructing Pb-210 chronology of young peat profiles sampled with low frequency. *Geochronometria*, *46*(1), 1–14. https://doi.org/10.1515/geochr-2015-0101

Soil Survey Staff. (1999). *Soil Taxonomy: A Basic System of Soil Classification for Making and Interpreting Soil Surveys* (2nd ed.). Natural Resources Conservation Service. U.S. Department of Agriculture. https://www.nrcs.usda.gov/Internet/FSE_DOCUMENTS/nrcs142p2_051232.pdf

Stuiver, M., & Polach, H. A. (1977). Discussion Reporting of ^{14}C Data. *Radiocarbon*, *19*(3), 355–363. https://doi.org/10.1017/S0033822200003672

Stumpf, A., Michéa, D., & Malet, J.-P. (2018). Improved Co-Registration of Sentinel-2 and Landsat-8 Imagery for Earth Surface Motion Measurements. *Remote Sensing*, *10*(2), 160. https://doi.org/10.3390/rs10020160

Sundqvist, M. K., Liu, Z., Giesler, R., & Wardle, D. A. (2014). Plant and microbial responses to nitrogen and phosphorus addition across an elevational gradient in subarctic tundra. *Ecology*, *95*(7), 1819–1835. https://doi.org/10.1890/13-0869.1

Sundqvist, M. K., Moen, J., Björk, R. G., Vowles, T., Kytöviita, M., Parsons, M. A., & Olofsson, J. (2019). Experimental evidence of the long-term effects of reindeer on Arctic vegetation greenness and species richness at a larger landscape scale. *Journal of Ecology*, *107*(6), 2724–2736. https://doi.org/10.1111/1365-2745.13201

Svendsen, J. I., & Mangerud, J. (1997). Holocene glacial and climatic variations on Spitsbergen, Svalbard. *The Holocene*, *7*(1), 45–57. https://doi.org/10.1177/095968369700700105

Swindles, G. T., Morris, P. J., Mullan, D. J., Payne, R. J., Roland, T. P., Amesbury, M. J., Lamentowicz, M., Turner, T. E., Gallego-Sala, A., Sim, T., Barr, I. D., Blaauw, M., Blundell, A., Chambers, F. M., Charman, D. J., Feurdean, A., Galloway, J. M., Gałka, M., Green, S. M., Kajukało, K., Karofeld, E., Korhola, A., Lamentowicz, Ł., Langdon, P., Marcisz, K., Mauquoy, D., Mazei, Y.A., McKeown, M.M., Mitchell, E.A.D., Novenko, E., Plunkett, G., Roe, H.M., Schoning, K., Sillasoo, Ü., Tsyganov, A.N., van der Linden, M., Väliranta & Warner, B. (2019). Widespread drying of European peatlands in recent centuries. *Nature Geoscience*, *12*(11), 922–928. https://doi.org/10.1038/s41561-019-0462-z

Tarnocai, C., Canadell, J. G., Schuur, E. a. G., Kuhry, P., Mazhitova, G., & Zimov, S. (2009). Soil organic carbon pools in the northern circumpolar permafrost region. *Global Biogeochemical Cycles*, *23*(2). https://doi.org/10.1029/2008GB003327

Teillet, P. M., Guindon, B., & Goodenough, D. G. (1982). On the Slope-Aspect Correction of Multispectral Scanner Data. *Canadian Journal of Remote Sensing*, *8*(2), 84–106. https://doi.org/10.1080/07038992.1982.10855028

Theil, H. (1950). *A rank-invariant method of linear and polynomial regression analysis. I, II, III*. *53*, 386–392, 521–525, 1397–1412.

Tian, J., Wang, L., Yin, D., Li, X., Diao, C., Gong, H., Shi, C., Menenti, M., Ge, Y., Nie, S., Ou, Y., Song, X., & Liu, X. (2020). Development of spectral-phenological features for deep learning to understand Spartina alterniflora invasion. *Remote Sensing of Environment*, *242*, 111745. https://doi.org/10.1016/j.rse.2020.111745

Treat, C. C., Jones, M. C., Camill, P., Gallego-Sala, A., Garneau, M., Harden, J. W., Hugelius, G., Klein, E. S., Kokfelt, U., Kuhry, P., Loisel, J., Mathijssen, P. J. H., O'Donnell, J. A., Oksanen, P. O., Ronkainen, T. M., Sannel, A. B. K., Talbot, J., Tarnocai, C., & Väliranta, M. (2016). Effects of permafrost aggradation on peat properties as determined from a pan-Arctic synthesis of plant macrofossils: Permafrost Effects on Peat Properties. Journal of Geophysical Research: Biogeosciences, 121(1), 78–94. https://doi.org/10.1002/2015JG003061

Tucker, C. J. (1979). *Red and photographic infrared linear combinations for monitoring vegetation* (Vol. 8). https://doi.org/10.1016/0034-4257(79)90013-0

Turetsky, M. R., Manning, S. W., & Wieder, R. K. (2004). Dating recent peat deposits. *Wetlands, 24*(2), 324–356. https://doi.org/10.1672/0277-5212(2004)024[0324:DRPD]2.0.CO;2

United nations. (2015). *Paris agreement*. https://unfccc.int/files/essential_background/convention/application/pdf/english_paris_agreement.pdf

United States Geological Survey. (n.d.-a). *Landsat Collection 2 Level-1 Data*. Retrieved March 28, 2020, from https://www.usgs.gov/land-resources/nli/landsat/landsat-collection-2-level-1-data?qt-science_support_page_related_con=1#qt-science_support_page_related_con

United States Geological Survey. (n.d.-b). *Landsat Surface Reflectance*. Landsat Surface Reflectance. Retrieved March 17, 2020, from https://www.usgs.gov/land-resources/nli/landsat/landsat-surface-reflectance

United States Geological Survey. (2019a). *EarthExplorer*. https://earthexplorer.usgs.gov/

United States Geological Survey. (2019b). *Landsat 4-7 Surface Reflectance (LEDAPS) Product Guide*. https://www.usgs.gov/media/files/landsat-4-7-surface-reflectance-code-ledaps-product-guide

United States Geological Survey. (2019c). *Landsat 8 Surface Reflectance Code (LASRC) Product Guide*. https://www.usgs.gov/media/files/land-surface-reflectance-code-lasrc-product-guide

USGS-EROS/espa-bulk-downloader. (2020). [Python]. USGS-EROS. https://github.com/USGS-EROS/espa-bulk-downloader (Original work published 2015)

van der Bilt, W. G. M., Bakke, J., Vasskog, K., D'Andrea, W. J., Bradley, R. S., & Ólafsdóttir, S. (2015). Reconstruction of glacier variability from lake sediments reveals dynamic Holocene climate in Svalbard. *Quaternary Science Reviews, 126,* 201–218. https://doi.org/10.1016/j.quascirev.2015.09.003

van der Knaap, W.O. (1988). *A Pollen Diagram from Brøggerhalvøya, Spitsbergen: Changes in Vegetation and Environment from CA. 4400 to CA. 800 BP*. *20*(1). https://doi.org/10.1080/00040851.1988.12002656

van der Knaap, W. O. (1989). Past Vegetation and Reindeer on Edgeoya (Spitsbergen) Between c. 7900 and c. 3800 BP, Studied by Means of Peat Layers and Reindeer Faecal Pellets. *Journal of Biogeography*, *16*(4), 379. https://doi.org/10.2307/2845229

van Pelt, W. J. J., Kohler, J., Liston, G. E., Hagen, J. O., Luks, B., Reijmer, C. H., & Pohjola, V. A. (2016). Multidecadal climate and seasonal snow conditions in Svalbard: Seasonal snow conditions in Svalbard. *Journal of Geophysical Research: Earth Surface*, *121*(11), 2100–2117. https://doi.org/10.1002/2016JF003999

Vickers, H., Høgda, K. A., Solbø, S., Karlsen, S. R., Tømmervik, H., Aanes, R., & Hansen, B. B. (2016). Changes in greening in the high Arctic: Insights from a 30 year AVHRR max NDVI dataset for Svalbard. *Environmental Research Letters*, *11*(10), 105004. https://doi.org/10.1088/1748-9326/11/10/105004

Vleeschouwer, F. D., Chambers, F. M., & Swindles, G. T. (2010). *Coring and sub-sampling of peatlands for palaeoenvironmental research*. 10.

Vogelmann, J. E., Xian, G., Homer, C., & Tolk, B. (2012). Monitoring gradual ecosystem change using Landsat time series analyses: Case studies in selected forest and rangeland ecosystems. *Remote Sensing of Environment*, *122*, 92–105. https://doi.org/10.1016/j.rse.2011.06.027

Walker, D. A. (2003). Phytomass, LAI, and NDVI in northern Alaska: Relationships to summer warmth, soil pH, plant functional types, and extrapolation to the circumpolar Arctic. *Journal of Geophysical Research*, *108*(D2), 8169. https://doi.org/10.1029/2001JD000986

Wang, M., Moore, T. R., Talbot, J., & Riley, J. L. (2015). The stoichiometry of carbon and nutrients in peat formation: C and nutrients in peat. *Global Biogeochemical Cycles*, *29*(2), 113–121. https://doi.org/10.1002/2014GB005000

Weiss, N., Faucherre, S., Lampiris, N., & Wojcik, R. (2017). Elevation-based upscaling of organic carbon stocks in High-Arctic permafrost terrain: A storage and distribution assessment for Spitsbergen, Svalbard. *Polar Research*, *36*(1), 1400363. https://doi.org/10.1080/17518369.2017.1400363

Wen, Z., Wu, S., Chen, J., & Lü, M. (2017). NDVI indicated long-term interannual changes in vegetation activities and their responses to climatic and anthropogenic factors in the Three Gorges Reservoir Region, China. *Science of The Total Environment*, *574*, 947–959. https://doi.org/10.1016/j.scitotenv.2016.09.049

Wojcik, R., Palmtag, J., Hugelius, G., Weiss, N., & Kuhry, P. (2019). Land cover and landform-based upscaling of soil organic carbon stocks on the Brøgger Peninsula, Svalbard. *Arctic, Antarctic, and Alpine Research*, *51*(1), 40–57. https://doi.org/10.1080/15230430.2019.1570784

Wulder, M. A., Masek, J. G., Cohen, W. B., Loveland, T. R., & Woodcock, C. E. (2012). Opening the archive: How free data has enabled the science and monitoring promise of Landsat. *Remote Sensing of Environment*, *122*, 2–10. https://doi.org/10.1016/j.rse.2012.01.010

Xiaoyi Guo, Hongyan Zhang, Zhengfang Wu, Jianjun Zhao, & Zhengxiang Zhang. (2017). Comparison and Evaluation of Annual NDVI Time Series in China Derived from the NOAA AVHRR LTDR and Terra MODIS MOD13C1 Products. *Sensors*, *17*(6), 1298. https://doi.org/10.3390/s17061298

Xu, J., Morris, P. J., Liu, J., Ledesma, J. L. J., & Holden, J. (2020). Increased Dissolved Organic Carbon Concentrations in Peat-Fed UK Water Supplies Under Future Climate and Sulfate Deposition Scenarios. *Water Resources Research*, *56*(1). https://doi.org/10.1029/2019WR025592

Yang, Z., Yang, W., Yuan, L., Wang, Y., & Sun, L. (2020). Evidence for glacial deposits during the Little Ice Age in Ny-Alesund, western Spitsbergen. *Journal of Earth System Science*, *129*(1), 19. https://doi.org/10.1007/s12040-019-1274-7

Yoshitake, S., Uchida, M., Iimura, Y., Ohtsuka, T., & Nakatsubo, T. (2018). Soil microbial succession along a chronosequence on a High Arctic glacier foreland, Ny-Ålesund, Svalbard: 10 years' change. *Polar Science*, *16*, 59–67. https://doi.org/10.1016/j.polar.2018.03.003

Yoshitake, S., Uchida, M., Ohtsuka, T., Kanda, H., Koizumi, H., & Nakatsubo, T. (2011). Vegetation development and carbon storage on a glacier foreland in the High Arctic, Ny-Ålesund, Svalbard. *Polar Science*, *5*(3), 391–397. https://doi.org/10.1016/j.polar.2011.03.002

Young, D. M., Baird, A. J., Charman, D. J., Evans, C. D., Gallego-Sala, A. V., Gill, P. J., Hughes, P. D. M., Morris, P. J., & Swindles, G. T. (2019). Misinterpreting carbon accumulation rates in records from near-surface peat. *Scientific Reports*, *9*(1), 17939. https://doi.org/10.1038/s41598-019-53879-8

Young, N. E., Anderson, R. S., Chignell, S. M., Vorster, A. G., Lawrence, R., & Evangelista, P. H. (2017). A survival guide to Landsat preprocessing. *Ecology*, *98*(4), 920–932. https://doi.org/10.1002/ecy.1730

Yu, Z., Beilman, D. W., Frolking, S., MacDonald, G. M., Roulet, N. T., Camill, P., & Charman, D. J. (2011). Peatlands and Their Role in the Global Carbon Cycle. *Eos, Transactions American Geophysical Union*, *92*(12), 97–98. https://doi.org/10.1029/2011EO120001

Yu, Z. C. (2012). Northern peatland carbon stocks and dynamics: A review. *Biogeosciences*, *9*(10), 4071–4085. https://doi.org/10.5194/bg-9-4071-2012

Yuan, L., Sun, L., Long, N., Xie, Z., Wang, Y., & Liu, X. (2010). Seabirds colonized Ny-Ålesund, Svalbard, Arctic ~9,400 years ago. *Polar Biology*, *33*(5), 683–691. https://doi.org/10.1007/s00300-009-0745-8

Yuan, W., Liu, S., Dong, W., Liang, S., Zhao, S., Chen, J., Xu, W., Li, X., Barr, A., Black, T.A., Yan, W., Goulden, M.L., Kulmala, L., Lindroth, A., Margolis, H.A., Matsuura, Y., Moors, E., van, der M., Ohta, T., Pilegaard, K., Varlagin, A., Vesala, T. (2014). Differentiating moss from higher plants is critical in studying the carbon cycle of the boreal biome. *Nature Communications*, *5*, 4270.

Zhang, H., Gallego-Sala, A. V., Amesbury, M. J., Charman, D. J., Piilo, S. R., & Väliranta, M. M. (2018). Inconsistent Response of Arctic Permafrost Peatland Carbon Accumulation to Warm Climate Phases. *Global Biogeochemical Cycles*, *32*(10), 1605–1620. https://doi.org/10.1029/2018GB005980

Zhou, L., Tucker, C. J., Kaufmann, R. K., Slayback, D., Shabanov, N. V., & Myneni, R. B. (2001). Variations in northern vegetation activity inferred from satellite data of vegetation index during 1981 to 1999. *Journal of Geophysical Research: Atmospheres*, *106*(D17), 20069–20083. https://doi.org/10.1029/2000JD000115

Zhu, Z., Wang, S., & Woodcock, C. E. (2015). Improvement and expansion of the Fmask algorithm: Cloud, cloud shadow, and snow detection for Landsats 4–7, 8, and Sentinel 2 images. *Remote Sensing of Environment*, *159*, 269–277. https://doi.org///doi.org/10.1016/j.rse.2014.12.014

12. Appendixes

Appendix A: Espa-bulk-downloader

Before starting you need to have python, git and pip installed:

python (https://www.python.org/downloads/)

GIT (https://gitforwindows.org/)

pip (download get-pip.py (https://bootstrap.pypa.io/get-pip.py).

Run through command line:

python get-pip.py

Next step: install the USGS-EROS ESPA-bulk downloader through command line:

pip install git+https://github.com/USGS-EROS/espa-bulk-downloader.git

Compose bulk download order of Landsat level-2 (Surface reflectance) products of your choice at USGS earth explorer (https://earthexplorer.usgs.gov). When the products are processed to Level-2 confirmation e-mail with order-id will be sent. Then bulk downloading trough command line is possible by:

python download_espa_order.py -e "your e-mail" -o "your order ID" -d "destination folder" -u "ERS username" -p "password"

Bulk downloading to your destination folder should start.

Appendix B: Age-depth modelling script

```
# Needed packages
install.packages("rbacon")
install.packages(“stringr”)
library(rbacon)
library(stringr)

# Empty global environment
rm(list=ls())
```

```
#set working directory
setwd("Your_directory_here")

####   Calculate C14 ages from pMC values of radiocarbon dates ####
# Needed variables:
# mn = Reported mean of the pMC.
# sdev = Reported error of the pMC.
# ratio = Most modern-date values are reported against 100. If it is against 1 instead, use 1 here.
# decimals = Count of decimals required for the radiocarbon age.

pMC.age(mn = 129.31, sdev = 0.34, ratio = 100, decimals = 2)

#### Age-depth modelling   ###
# List all profile directories and go through all profile-files by changing CoreDir[] index
# Thickness (thick=) affects flexibility of the age-depth model. Smoother with smaller sections but computationally heavy.
# choose correct post bomb-calibration curve (http://calib.org/CALIBomb/)
# 14C calibration curve is IntCal13 (cc=1). Options are cc=2 (Marine13), cc=3 (SHCal13), or cc=4 (an alternative curve).

#Retrieve directory names (core files) to a list
coreDirList = list.dirs(path = ".", full.names = FALSE, recursive = FALSE)

#Check that the length of the list matches number of your samples
length(coreDirList)

#change the coreDirList[] -index value to change the input sample file (from 1 - to list length)
coreName = coreDirList[1]

#Main modelling function
#"acc.mean" control estimated deposition speed.
#"thick" controls size of sections function splits core into
#"d.by" controls output depths for which ages are calculated.
```

```
Bacon(coredir= ".", core = coreName, acc.mean = , thick = 0.5, d.by = 1, postbomb = 1, cc = 1,
depth.unit="cm", age.unit = "yr", rotate.axes = TRUE, rev.age = TRUE)

#Test if the MCMC mixing of your core, with the applied settings, can be trusted (not compulsory)
#Values above 1.05 threshold of the 'Gelman and Rubin Reduction Factor' indicates poor mixing
#"run =" determines how many model runs will be compared
Baconvergence(core = coreName, run = 10, coredir= ".", thick =  1, postbomb = 1, cc = 1,
depth.unit="cm", age.unit = "yr")

#Configure agedepth-plot only
agedepth(model.only = TRUE, rotate.axes = TRUE , rev.age = TRUE, age.lab = 'Year (cal BP)',
d.lab='Depth (cm)', bty='O')

#Plot core's estimated accumulation rates cm/yr
accrate.age.ghost(rev.age = TRUE, plot.range = FALSE, cmyr = TRUE, acc.lim = c(0,3))

#Add site name to the plot, with x & y values that converge with the created plot upper left corner
text(x = 37, y = 2.7, labels = coreName, cex = 1.8)
```

Appendix C: Landsat cloud masking

```
#Clear environment
rm(list = ls())
options(stringsAsFactors= FALSE)

#### Needed packages ###
install.packages("raster")
install.packages("rgdal")
library("raster")
library("rgdal")

### INPUT DATA PATHS ###
#Local path for Landsat 8 OLI images
imgPathOli = "F:/lsTimeSeries/oli/wrs2/"
```

```
#Local path for OLI images chosen to act as reference images
refPath = "F:/ref_Images/"
#Local path for TM images to be corrected
imgPath = "F:/lsTimeSeries/tm/wrs2/"

### Pixel values to be masked ###
# Landsat 8 surface reflectance code (LASRC) product guide:
https://www.usgs.gov/media/files/land-surface-reflectance-code-lasrc-product-guide
# Pixels with low confidence cloud assessment are not taken into consideration
# Cloud shadow: 328, 392, 840, 904, 1350
# Cloud: 352, 368, 416, 432, 480, 864, 880, 928, 944, 992
# Medium confidence cloud: 386, 388, 392, 400, 416, 432, 898, 900, 904, 928, 944
# High confidence cloud: 480, 992
# High confidence cirrus: 834, 836, 840, 848, 864, 880, 898, 900, 904, 912, 928, 944, 992

# Landsat 4-7 Surface Reflectance (LEDAPS) Product Guide:
https://www.usgs.gov/media/files/landsat-4-7-surface-reflectance-code-ledaps-product-guide
# Pixels with low confidence cloud assesment are not taken in to consideration
# Cloud shadow: 72, 136
# Cloud: 96, 112, 160, 176, 224
# Medium confidence cloud: 130, 132, 136, 144, 160, 176
# High confidence cloud: 224

### LANDSAT 8 OLI IMAGES ###

#index
i=1
#WRS 2 scenes
wrs = list("210004", "211004",
214004","215004","216004","217003","217004","218003","219003")

#Iterate WRS scenes
for (i in 1:length(wrs)){
```

```
  #Find sub directories containing individual acquisition directories
  subDirs = list.dirs(paste(imgPathOli, wrs[i], sep=""), recursive=FALSE)
  #sub-directory index
  j=1

  for (j in 1:length(subDirs)){

    #Find pixel_qa -file
    qaFile = list.files(path = subDirs[j], pattern = "pixel_qa.tif", full.names = FALSE)
    qaFilePath = paste(subDirs[j],"/",qaFile[1], sep="")
    qaFileName = gsub(pattern = "\\.tif$","", qaFile)

    #Boolean raster from qa-band cloud values
    #Result has cloud values TRUE (1) and clear pixels FALSE (0)
    raster_qa = raster(qaFilePath)
    raster_qa[raster_qa %in% c(328, 392, 840, 904, 1350, 352, 368, 416, 432, 480, 864, 880, 928,
944, 992, 386, 388, 400, 898, 900, 944, 834, 836, 848, 912)] = 9999
    raster_qa[raster_qa != 9999] = FALSE
    raster_qa[raster_qa == 9999] = TRUE
    #Set NA pixels to have value TRUE
    raster_qa[is.na(raster_qa)] = TRUE

    #write cloud mask file to same folder
    outputD = paste(subDirs[j],"/", sep="")
    out_path = paste(outputD,qaFileName,"_cloudMask.tiff",sep="")
    writeRaster(raster_qa, out_path, format= "GTiff", overwrite=TRUE, datatype = "INT2S")

    #remove variables
    rm(qaFile, qaFilePath, qaFileName, raster_qa, outputD, out_path)
    removeTmpFiles(h = 0.016)

    j= j+1
    }
i = i+1
```

```
}

### LANDSAT 5TM and Landsat 7 TM+ data ###
# Determine WRS-2 scenes
wrs = list("210004", "211004", "212004", "213004",
"214004","215004","216004","217003","217004","218003","219003")
# Index
i=1

#loop through WRS-2 scenes
for (i in 1:length(wrs)){

  #Find sub directories containing individual acquisition directories
  subDirs = list.dirs(paste(imgPath,wrs[i], sep=""), recursive=FALSE)
  #Sub-directory index
  j = 1

  for (j in 1:length(subDirs)){

    #Find pixel_qa -file
    qaFile = list.files(path = subDirs[j], pattern = "pixel_qa.tif", full.names = FALSE)
    qaFilePath = paste(subDirs[j],"/",qaFile[1], sep="")
    qaFileName = gsub(pattern = "\\.tif$","", qaFile)

    #Boolean cloud mask from qa-band
    #Result has cloud values TRUE (1) and clear pixels FALSE (0)
    raster_qa = raster(qaFilePath)
    raster_qa[raster_qa %in% c(72, 136,96, 112, 160, 176, 224,130, 132, 144)] <- 9999
    raster_qa[raster_qa != 9999] = FALSE
    raster_qa[raster_qa == 9999] = TRUE
    #Set NA pixels to have value TRUE
    raster_qa[is.na(raster_qa)] = TRUE

    #write cloud mask to same folder
```

```
    outputD = paste(subDirs[j],"/", sep="")
    out_path = paste(outputD,qaFileName,"_cloudMask.tiff",sep="")
    writeRaster(raster_qa, out_path, format= "GTiff", overwrite=TRUE, dataType = "INT2S")

    #remove variables
    rm(qaFile, qaFilePath, qaFileName, raster_qa, outputD, out_path)
    removeTmpFiles(h = 0.016)

    j= j+1
  }
 i = i+1
}
```

Appendix D: Landsat co-registration

```
# These installation commands should work within local Jupyter lab
# Install packages needed for AEROSICS-package to work properly
import sys
!conda install --yes --prefix {sys.prefix} -c conda-forge numpy gdal scikit-image matplotlib pyproj shapely geopandas pandas cmocean basemap pykrige

# Package to speed up AROSICS local co-registration function. (Not necessary and not compatible with newest Python versions). Co-registration will work without this package - just slower.
!conda install --yes --prefix {sys.prefix} -c jesserobertson pyfftw

# Package to read the filepaths
!{sys.executable} -m pip install glob2

# Package for co-registration of images
!{sys.executable} -m pip install arosics

# Package for stacking image bands
!{sys.executable} -m pip install rasterio
# If this does not work, download and install binaries from:
https://www.lfd.uci.edu/~gohlke/pythonlibs/#rasterio
```

```
# Import needed packages
import glob2 as glob
from arosics import COREG_LOCAL
from arosics import COREG
import rasterio
import os
import gdal
import numpy as np
import matplotlib.pyplot as plt

#Input directories
#Landsat 8 OLI images chosen to work as reference
refPath = "F:/refImages/"

#All other Landsat 8 OLI images
imgPathOli = "F:/lsTimeSeries/oli/wrs2/"

#Landsat 5 TM and Landsat 7 ETM+ images to be corrected
imgPath = "F:/lsTimeSeries/tm/wrs2/"
# Define band stacking functions (OLI and TM Sensors have differing bands)
# Landsat 8 data
def stackBandsL8(bandList, out_path):
    '''Stacks bands given in a list. Modified from Loïc Dutrieux post at:
    https://gis.stackexchange.com/questions/223910/using-rasterio-or-gdal-to-stack-multiple-bands-
without-using-subprocess-commands
    '''
    #band names
    descriptions = [
    'cloudMask',
    'B4',
    'B5'
    ]
```

```
# Read metadata of first file
    with rasterio.open(bandList[0], dtype = rasterio.int16) as src0:
        meta = src0.meta

    # Update meta to reflect the number of layers
    meta.update(count = len(bandList))

    # Read each layer and write it to stack. Define the data type to signed integer 16 bit
    with rasterio.open(out_path, 'w', **meta) as dst:
        for id, layer in enumerate(bandList, start=1):
            with rasterio.open(layer) as src1:
                dst.write_band(id, src1.read(1).astype(rasterio.int16))
                dst.set_band_description(id, descriptions[id-1])

# Landsat 5 and 7 data
def stackBandsL5L7(bandList, out_path):
    '''Stacks bands given in a list. Modified from Loïc Dutrieux post at:
    https://gis.stackexchange.com/questions/223910/using-rasterio-or-gdal-to-stack-multiple-bands-
without-using-subprocess-commands
    '''
    #band names
    descriptions = [
    'cloudMask',
    'B3',
    'B4'
    ]
    # Read metadata of first file
    with rasterio.open(bandList[0], dtype = rasterio.int16) as src0:
        meta = src0.meta

    # Update meta to reflect the number of layers
    meta.update(count = len(bandList))
    # Read each layer and write it to stack. Define the data type to to signed integer 16 bit.
    with rasterio.open(out_path, 'w', **meta) as dst:
```

```
        for id, layer in enumerate(bandList, start=1):
            with rasterio.open(layer) as src1:
                dst.write_band(id, src1.read(1).astype(rasterio.int16))
                dst.set_band_description(id, descriptions[id-1])

# Stack Landsat 8 cloudmask, red- and NIR-bands into "datacubes"
# Determine WRS-2 scenes where input data is recorded
wrs = ["210004", "211004", "214004","215004","216004","217003","217004","218003","219003"]

for sceneId in wrs:
    ''' Iteratively create datacubes by stacking bands within each acquistion scene folder'''

    #check sub-directories (acquistions) under every WRS-scene
    subDirs = os.listdir(imgPathOli + sceneId + "/")
    for directory in subDirs:

        #iterate subdirectories, create list of bands and compile datacubes
        cloudMask = glob.glob(imgPathOli + sceneId + "/" + directory + "/*cloudMask.tif")
        band4 = glob.glob(imgPathOli + sceneId + "/" + directory + "/*band4.tif")
        band5 = glob.glob(imgPathOli + sceneId + "/" + directory + "/*band5.tif")
        bandList = cloudMask + band4 + band5

        #output
        outputD = imgPathOli + sceneId + "/" + directory + "/"
        filename = directory + "_STACK.tiff"
        out_path = outputD + filename
        stackBandsL8(bandList, out_path)

# Stack Landsat 5 and 7 cloudmask, red- and NIR-bands into "datacubes"
# Determine WRS-2 scenes where input data is recorded
wrs = ["210004", "211004", "212004", "213004",
"214004","215004","216004","217003","217004","218003","219003"]
for sceneId in wrs:
    ''' Iteratively create datacubes by stacking bands within each acquistion scene folder'''
```

```
    #check sub-directories (acquistions) under every WRS-scene
    subDirs = os.listdir(imgPath + sceneId + "/")
    for directory in subDirs:

        #iterate subdirectories, create list of bands and compile datacubes
        cloudMask = glob.glob(imgPath + sceneId + "/" + directory + "/*cloudMask.tif")
        band3 = glob.glob(imgPath + sceneId + "/" + directory + "/*band3.tif")
        band4 = glob.glob(imgPath + sceneId + "/" + directory + "/*band4.tif")
        bandList = cloudMask + band3 + band4

        #output
        outputD = imgPath + sceneId + "/" + directory + "/"
        filename = directory + "_STACK.tiff"
        out_path = outputD + filename
        stackBandsL5L7(bandList, out_path)

# Compile co-registration function. Set inputs are:
# reference image, target image, reference cloud mask, target cloud mask, and output-path

def co_reg(im_reference, im_target, cloud_mask_ref, cloud_mask_tgt, out_path):
    '''co-registers reference and target images. Pre-determined bands from the stacks
    are for L8 OLI B6 and for L5&L7 B5.  '''
    CRL = COREG_LOCAL(im_reference,im_target, mask_baddata_ref=cloud_mask_ref,
mask_baddata_tgt=cloud_mask_tgt, path_out=out_path, grid_res=40, max_iter=20, max_shift=40,
window_size=(360,360), fmt_out= 'GTIFF')
    CRL.correct_shifts()

#Co-Register all the Landsat 5 and 7 stacks iteratively, using Landsat 8 NIR band as reference

wrs = ["210004", "211004", "212004", "213004",
"214004","215004","216004","217003","217004","218003","219003"]
for sceneId in wrs:
```

```
    """Iterates all the WRS-2 acquisition scenes. Co-registers all the Landsat 5 & 7 raster stacks to a Landsat 8 raster stack from a corresponging WRS-2 scene. Corrected raster stacks are the written as an output"""

    #path for reference raster
    refFile = glob.glob(refPath+sceneId+"/*/*band5.tif")
    refFile = "".join(refFile) #list to str

    #path for reference cloud-mask
    refCloudMask = glob.glob(refPath+sceneId+"/*/*_cloudMask.tif")
    refCloudMask = "".join(refCloudMask) # List to str

    # List sub-directories of raster stacks to be corrected
    imgSubDirs = os.listdir(imgPath + sceneId + "/")
    #iterate target image directories at imgSubDirs:

        #path for target raster stack
        imgStack = glob.glob(imgPath+ sceneId+"/"+directory+ "/*STACK.tiff")
        imgStackPath = "".join(imgStack) # List to str

        #path for target cloud mask
        tgtCloudMask = glob.glob(imgPath+sceneId+"/"+directory+ "/*_cloudMask.tif")
        tgtCloudMask = "".join(tgtCloudMask) # List to str

        #Output path
        outputD = imgPath + sceneId + "/" + directory + "/"
        filename = directory + "_STACK_cor.tiff"
        output_path = imgPath + filename

        #Co-register
       CRL =  co_reg(im_reference = refFile, im_target = imgStackPath, cloud_mask_ref = refCloudMask, cloud_mask_tgt = tgtCloudMask, out_path = output_path)
```

```
# Visualization of the calculated absolute lenghts of the initial shift vectors.
CRL.view_CoRegPoints(figsize=(15,15), backgroundIm='tgt')

#By comparing corrected image to the initial reference image, one can achieve map of shifts present AFTER shift correction. (Do not set output for local co-registration)
CRL_after_corr = COREG_LOCAL(im_ref= "reference stack path", im_tgt="corrected output filepath",grid_res=150, fmt_out= 'GTIFF', max_iter= 10, max_shift= 15, window_size=(60,60))
CRL_after_corr.view_CoRegPoints(figsize=(15,15),backgroundIm='ref')

#GLOBAL REGISTRATION – if needed (paths and coordinates manually set)
#Reference data
im_reference = "F:/refImages/216004/LC082160042015080101T1-SC20200106154242/LC08_L1TP_216004_20150801_20170406_01_T1_sr_band5.tif"
cloud_maskRef = "F:/refImages/216004/LC082160042015080101T1-SC20200106154242/LC08_L1TP_216004_20150801_20170406_01_T1_pixel_qa_cloudMask.tif"

#Target data
im_target = "F:/lsTimeSeries/tm/wrs2/218003/LT052180031998071501T2-SC20200106121650/LT052180031998071501T2-SC20200106121650_STACK.tiff"
im_mask = "F:/lsTimeSeries/tm/wrs2/218003/LT052180031998071501T2-SC20200106121650/LT05_L1GS_218003_19980715_20161223_01_T2_pixel_qa_cloudMask.tif"

#Ouput path
output_path = "F:/lsTimeSeries/tm/wrs2/reRun/corGL/LT052180031998071501T2-SC20200106121650_STACK_GLcor.tiff"

# Determine matching window centroid XY-coordinates manually
wpCoords = (439191,8771931)
#Global co-registration
coRegImg = COREG(im_reference, im_target, mask_baddata_ref=cloud_maskRef, mask_baddata_tgt= im_mask, s_b4match=3, wp= wpCoords, max_iter=40, max_shift=705, ws=(4000,4000), path_out=output_path)
coRegImg.correct_shifts()
```

Appendix E: Topographic correction

```
# Applying sensor calibration coefficients to NDVI images (Pironkova et al. 2018)

#clear environment
rm(list = ls())
options(stringsAsFactors= FALSE)

#install.packages("raster")
#install.packages("rgdal")
#install.packages("gdalUtils")
##install.packages("RStoolbox")
library(rgdal)
library(gdalUtils)
library(raster)
library(RStoolbox)

#Area of interest .shp file (AOI)
aoi = readOGR("F:/ data/GIS/AOI/isfjord.shp")
#Extract crs and aoi information
targetCrs = crs(aoi)
targetExtent = extent(aoi)

#Digital elevation model
dem = raster("F:/arcticDEM/isfjord_DEM30m_crop.tif")
#Make sure datasets have same crs
dem = projectRaster(dem, crs = targetCrs)
#Extract slope and aspect information as radians
terrDem = terrain(dem, opt=c('slope','aspect'), unit= 'radians')
rm(dem)

### Landsat 8 data ###
oliPath = "F:/lsTimeSeries/oli/wrs2/"
outputD = "F:/topoCorNDVI/"
```

```
wrs = list("210004", "211004",
"214004","215004","216004","217003","217004","218003","219003")

#index
i=1

#Iterate WRS scenes
for (i in 1:length(wrs)){

 #Sub directories of individual acquisitions
 subDirs = list.dirs(paste(oliPath,wrs[i], sep=""), recursive=FALSE)
 #sub-directory index
 j=1

 for (j in 1:length(subDirs)){

  #Read in data stack
  stackPath = list.files(path = subDirs[j], pattern = "STACK.tiff", full.names = T)
  dataStack = stack(stackPath)

  #Extract filename for output
  stackName = list.files(path = subDirs[j], pattern = "*STACK.tiff", full.names = FALSE)
  outputName = gsub(pattern = "_STACK.tiff$","", stackName)

  #Re-project and crop data
  dataStack = projectRaster(dataStack, crs = targetCrs)
  dataStackCrop = crop(dataStack, targetExtent)
  rm(stackPath, dataStack, stackName)

  #Align terrain data with Landsat data
  terrAlign = resample(terrDem, dataStackCrop[[3]], method ="bilinear")

  #Subset needed bands
  cloudMask = dataStackCrop[[1]]
```

```
redBand = dataStackCrop[[2]]
nirBand = dataStackCrop[[3]]
rm(dataStackCrop)

#Cloudmask red and NIR band
redBandMasked = mask(x = redBand, mask = cloudMask, maskvalue =1, updateValue = NA)
nirBandMasked = mask(x = nirBand, mask = cloudMask, maskvalue =1, updateValue = NA)
rm(redBand, nirBand, cloudMask)

#Valid range of landsat Surface reflectance values is 0 to 10 000 (scale factor 0.0001)
redBandMasked[redBandMasked < 0] = NA
nirBandMasked[nirBandMasked < 0] = NA

redBandMasked[redBandMasked > 10000] = NA
nirBandMasked[nirBandMasked > 10000] = NA

#Read acquisition metadata
metaFilePath = list.files(path = subDirs[j], pattern = "MTL.txt", full.names = T)
metaData <- readMeta(metaFilePath)

#Topographically correct image
redTopo = topCor(redBandMasked, terrAlign, metaData, method = "avgcos")
nirTopo = topCor(nirBandMasked, terrAlign, metaData, method = "avgcos")
rm(redBandMasked, nirBandMasked, terrAlign, metaFilePath, metaData)

#Topographically corrected NDVI values
ndvi = (nirTopo - redTopo) / (nirTopo + redTopo)
rm(nirTopo, redTopo)

#L8 to L7 Calibration coefficient
NDVI_calib = ndvi * 1.0863

#Using calibration coefficient, can cause some pixel values to exceed NDVI limits
NDVI_calib[NDVI_calib > 1] = 1
```

```
    NDVI_calib[NDVI_calib < -1] = -1

    #If image does not fill extent of AOI, fill empty areas within extent with NA values.
    if (extent(NDVI_calib) != targetExtent){
      NDVI_calib = extend(x = NDVI_calib, y = targetExtent, value = NA)
    }

    #Write file
    out_path = paste(outputD,outputName,"_NDVI.tiff",sep="")
    writeRaster(NDVI_calib, out_path, format = "GTiff", overwrite=TRUE)
    rm(NDVI, NDVI_calib, outputName, out_path)

    #To save disk space during the loop - remove temporary raster files older than one minute
    removeTmpFiles(h = 0.016)
    j= j+1
  }
  i = i+1
}

### Landsat 5 & 7 data ###
tmPath <- "F:/lsTimeSeries/tm/wrs2/"
outputD = "F:/topoCorNDVI/"
wrs = list("210004", "211004", "212004", "213004",
"214004","215004","216004","217003","217004","218003","219003")

#index
i=1

#Iterate WRS scenes
for (i in 1:length(wrs)){

  #Find sub directories of individual acquisitions
  subDirs = list.dirs(paste(tmPath,wrs[i], sep=""), recursive=FALSE)
  #sub-directory index
```

```
j=1

for (j in 1:length(subDirs)){

  #Read in data stack - crop with area of interest extent
  stackPath = list.files(path = subDirs[j], pattern = "*_STACK_cor.tiff", full.names = T)
  dataStack = stack(stackPath)

  #Extract filename for output
  stackName = list.files(path = subDirs[j], pattern = "*_STACK_cor.tiff", full.names = FALSE)
  outputName = gsub(pattern = "_STACK_cor.tiff$","", stackName)

  #Project and crop data
  dataStack = projectRaster(dataStack, crs = targetCrs)
  dataStackCrop = crop(dataStack, targetExtent)
  rm(stackPath, dataStack, stackName)
  #Align terrain grid with Landsat data
  terrAlign = resample(terrDem, dataStackCrop[[3]], method ="bilinear")

  #Subset needed bands
  cloudMask = dataStackCrop[[1]]
  redBand = dataStackCrop[[2]]
  nirBand = dataStackCrop[[3]]
  rm(dataStackCrop)

  # Cloudmask red and NIR band
  redBandMasked = mask(x = redBand, mask = cloudMask, maskvalue =1, updateValue = NA)
  nirBandMasked = mask(x = nirBand, mask = cloudMask, maskvalue =1, updateValue = NA)
  rm(redBand, nirBand, cloudMask)

  #Valid range of landsat Surface reflectance values is 0 to 10 000 (scale factor 0.0001)
  redBandMasked[redBandMasked < 0] = NA
  nirBandMasked[nirBandMasked < 0] = NA
```

```
  redBandMasked[redBandMasked > 10000] = NA
  nirBandMasked[nirBandMasked > 10000] = NA

  #Read acquisition metadata
  metaFilePath = list.files(path = subDirs[j], pattern = "MTL.txt", full.names = T)
  metaData <- readMeta(metaFilePath)

  #Topographically correct image
  redTopo = topCor(redBandMasked, terrAlign, metaData, method = "avgcos")
  nirTopo = topCor(nirBandMasked, terrAlign, metaData, method = "avgcos")
  rm(redBandMasked,nirBandMasked, terrAlign, metaFilePath, metaData)

  #Topographically corrected NDVI values
  ndvi = (nirTopo - redTopo) / (nirTopo + redTopo)
  rm(nirTopo, redTopo)

  #Make sure final file's extent matches area of interest
  #If image does not fill extent of aoi, fill empty areas within extent with NA values.
  if (extent(ndvi) != extent(aoi)){
    ndvi = extend(x = ndvi, y = targetExtent, value = NA)
  }

  #Write file
  out_path = paste(outputD,outputName,"_NDVI.tiff",sep="")
  writeRaster(ndvi, out_path, format = "GTiff", overwrite=TRUE)
  rm(ndvi, outputName, out_path)

  #To save disk space during the loop - remove temporary raster files older than one minute
  removeTmpFiles(h = 0.016)
  j= j+1
 }
 i = i+1
}
```

```
# Apply calibration coefficient to Landsat 5 topographically corrected files
l5Files = list.files(path = outputD, recursive = TRUE, pattern = "LT05*", full.names = T)
i = 1

for (i in 1:length(l5Files)){
  l5file = raster(l5Files[i])
  #Landsat 5 to landsat 7 equivalent
  l5file = l5file * 1.036
  #Scale values exceeding NDVI limits
  l5file[l5file > 1] = 1
  l5file[l5file < -1] = -1
  #overwrite raster
  writeRaster(l5file, filename = l5Files[i], format = "GTiff", overwrite=TRUE)
  i=i+1
}
#Literature:
#Pironkova, Whaley & Lan. (2018). Time series analysis of Landsat NDVI composites with Google Earth Engine and R: User guide - Science and Research Technical Manual TM-06. 10.13140/RG.2.2.16830.95040.
```

Appendix F: Annual NDVI composites

```
#clear environment
rm(list = ls())
options(stringsAsFactors= FALSE)

#install.packages("raster")
#install.packages("rgdal")
#install.packages("gdalUtils")
library(rgdal)
library(gdalUtils)
library(raster)
```

```
#Filepaths
ndviPath = "F:/topoCorNDVI"
outputMax = "F:/annualComposites/max/"

#List topographically corrected NDVI files
ndviFiles = list.files(path = ndviPath, pattern = "NDVI.tif", recursive = TRUE, full.names = T)

#Find sub directories of NDVI per year
yearDirs = list.dirs(ndviPath, recursive=FALSE)

#Read in .shp file with Svalbard land areas
#Make sure file has same CRS as NDVI rasters
landMask <- readOGR("F:/data/GIS/NP_S1000_SHP/S1000_Land_f.shp")
landMask <- spTransform(landMask, CRSobj = "+proj=utm +zone=33 +datum=WGS84 +units=m
+no_defs +ellps=WGS84 +towgs84=0,0,0")

#index
i=1

#Iterate directories containin NDVI images per year
for (i in 29:length(yearDirs)){

  #List images of certain year
  ndviFiles = list.files(path = yearDirs[i], pattern = "NDVI.tif", full.names = T)

  #If more than one acquistion is available calculate max values
  #Else use the single image as it is
  if (length(ndviFiles)> 1){

    #Read files into stack and mask sea areas out
    annualData = stack(ndviFiles)
    annualData = mask(annualData, landMask)
```

```
    #Annual Max
    anMax = max(annualData, na.rm = T)
    maxOutPath =  paste(outputMax,years[i],"NDVImax.tif", sep = "")
    writeRaster(anMax, maxOutPath, format = "GTiff", overwrite=TRUE)
    rm(annualData, anMed, anMax)

  } else {

    #Read raster and mask sea areas out
    singleAcq = raster(ndviFiles)
    singleAcq = mask(singleAcq, landMask)

    #Write files
    maxOutPath =  paste(outputMax,years[i],"NDVImax.tif", sep = "")
    writeRaster(singleAcq, maxOutPath, format = "GTiff", overwrite=TRUE)
    rm(singleAcq)
  }

  rm(ndviFiles, maxOutPath)
  removeTmpFiles(h = 0.016)
  i = i+1
}
#Create raster stacks of maximum NDVI composites
maxFiles = list.files(path = outputMax, pattern = "max.tif", recursive = TRUE, full.names = T)
maxStack= stack(maxFiles)
writeRaster(maxStack, filename = "F:/annualComposites/maxStack.tiff",format = "GTiff")
```

Appendix G: Regional Mann-Kendal test and soil profile -wise timeseries

```
#clear environment
rm(list = ls())
options(stringsAsFactors= FALSE)
```

```
#install.packages("rgdal")
#install.packages("raster")
#install.packages("stringr")
#install.packages("stats")
#install.packages("lubridate")
#install.packages("rkt")

library(rgdal)
library(raster)
library(stringr)
library(stats)
library(lubridate)
library(rkt)

#READ IN DATA
maxStack = stack("F:/annualComposites/maxStack.tif")
samplePoints = read.csv("F:/ data/GIS/coringPoints/profilePoints.csv", sep = ";", header = T)

#Acquisition years as list
years = list.dirs("F:/topoCorNDVI", recursive=FALSE, full.names = F)
#Set acquisition date in the middle of July (median of the dates in building composites)
#Convert to date variable
Dates = as.Date(paste(years,"-7-16", sep = ""), format = "%Y-%m-%d", origin="1985-7-16")

#set date values to stack
stackDates = setZ(maxStack, Dates)
#convert year info also to numeric form
year <- as.numeric(substr(getZ(stackDates), 1, 4))

#Define function for pixel-wise Regional Kendall Tests for trend and Theil-Sen's slope estimator.
#Mofified from Pironkova et al (2018)


tsFunc <- function(x) {
```

```
  if(all(is.na(x))){
    c(NA,NA,NA)
  } else {
    mKenn <- rkt(year, x)
    a = mKenn$B
    b = mKenn$sl
    c = mKenn$tau
    return(cbind(a, b, c))
  }
}

#apply Man Kendall test function to maximum NDVI stack
mkRaster <- calc(stackDates, fun=tsFunc)
names(mkRaster) = c("thsSlope", "p-value", "tau")

#Save output
writeRaster(mkRaster, filename = "F:/annualComposites/mkTimeSerie.tiff", format = "GTiff",
overwrite=TRUE)

#MAX VALUE COMPOSITE
#Theil-Sens slope estimator
thSlope = mkRaster[[1]]
#p-value raster
pValue = mkRaster[[2]]
#Tau raster
kTau = mkRaster[[3]]

#p-value maskraster
pValue[pValue > 0.05] = NA
#tau maskraster
kTau[kTau < -0.4 & kTau > 0.4]
#Mask by
maskedSl = mask(thSlope, pValue)
maskedSl = mask(maskedSl, kTau)
```

```
writeRaster(maskedSl, filename = "F:/annualComposites/mkTimeSerieMasked.tiff", format =
"GTiff", overwrite=TRUE)

### INDVIDUSAL MEASUREMENT POINT TIME SERIES ###
#Extract sitenames and xy coordinates in decimal degrees
coords = samplePoints[, c("id", "longitudeDD_E", "latitudeDD_N")]
names(coords) = c("id", "x", "y")

#Set projection information
coordinates(coords)= ~x + y
proj4string(coords) = CRS("+proj=longlat +ellps=WGS84 +datum=WGS84")

#Convert projection
sitesProjected <- spTransform(coords, crs(maxStack))

#Subset samplepoints that have age-depth models composed
Alk1 = subset(sitesProjected, sitesProjected$id == "Alk1.")
Alk3 = subset(sitesProjected, sitesProjected$id ==  "Alk3.")
Alk4 = subset(sitesProjected, sitesProjected$id ==  "Alk4.")
Alk5 = subset(sitesProjected, sitesProjected$id ==  "Alk5.")
Alk7 = subset(sitesProjected, sitesProjected$id ==  "Alk7.")
Bj1 = subset(sitesProjected, sitesProjected$id == "BJ1.")
Bj2 = subset(sitesProjected, sitesProjected$id == "BJ2.")
Bj3 = subset(sitesProjected, sitesProjected$id ==  "BJ3.")
Bo1.1 = subset(sitesProjected, sitesProjected$id ==  "Bo1.1")
Bo1.3 = subset(sitesProjected, sitesProjected$id ==  "Bo1.3")
Bo1.4 = subset(sitesProjected, sitesProjected$id == "Bo1.4")
Bo1.6 = subset(sitesProjected, sitesProjected$id ==  "Bo1.6")
Col1 = subset(sitesProjected, sitesProjected$id ==  "Col1.")
Col2 = subset(sitesProjected, sitesProjected$id == "Col2.")
Col4 = subset(sitesProjected, sitesProjected$id == "Col4.")



#Extract NDVI weighted mean NDVI value from buffer area surrounding sample points
```

```
#Alkehornet sample points
Alk1_maxNdvi = extract(maxStack, Alk1, buffer=50, fun=mean, na.rm=T, weights = T,
normalizeWeigths = T)
Alk1_ts = as.numeric(Alk1_maxNdvi)
write.csv(Alk1_ts, file= "F:/pointTimeSeriesCsv/Alk1_ts.csv")

Alk3_maxNdvi = extract(maxStack, Alk3, buffer=50, fun=mean, na.rm=T, weights = T,
normalizeWeigths = T)
Alk3_ts = as.numeric(Alk3_maxNdvi)
write.csv(Alk3_ts, file= "F:/pointTimeSeriesCsv/Alk3_ts.csv")

Alk4_maxNdvi = extract(maxStack, Alk4, buffer=50, fun=mean, na.rm=T, weights = T,
normalizeWeigths = T)
Alk4_ts = as.numeric(Alk4_maxNdvi)
write.csv(Alk4_ts, file= "F:/pointTimeSeriesCsv/Alk4_ts.csv")

Alk5_maxNdvi = extract(maxStack, Alk5, buffer=50, fun=mean, na.rm=T, weights = T,
normalizeWeigths = T)
Alk5_ts = as.numeric(Alk5_maxNdvi)
write.csv(Alk5_ts, file= "F:/pointTimeSeriesCsv/Alk5_ts.csv")

Alk7_maxNdvi = extract(maxStack, Alk7, buffer=50, fun=mean, na.rm=T, weights = T,
normalizeWeigths = T)
Alk7_ts = as.numeric(Alk7_maxNdvi)
write.csv(Alk7_ts, file= "F:/pointTimeSeriesCsv/Alk7_ts.csv")

#Bjordalen sample points
Bj1_maxNdvi = extract(maxStack, Bj1, buffer=50, fun=mean, na.rm=T, weights = T,
normalizeWeigths = T)
Bj1_ts = as.numeric(Bj1_maxNdvi)
write.csv(Bj1_ts, file= "F:/pointTimeSeriesCsv/Bj1_ts.csv")

Bj2_maxNdvi = extract(maxStack, Bj2, buffer=50, fun=mean, na.rm=T, weights = T,
normalizeWeigths = T)
```

```
Bj2_ts = as.numeric(Bj2_maxNdvi)
write.csv(Bj2_ts, file= "F:/pointTimeSeriesCsv/Bj2_ts.csv")

Bj3_maxNdvi = extract(maxStack, Bj3, buffer=50, fun=mean, na.rm=T, weights = T,
normalizeWeigths = T)
Bj3_ts = as.numeric(Bj3_maxNdvi)
write.csv(Bj3_ts , file= "F:/pointTimeSeriesCsv/Bj3_ts.csv")

#Bolterdalen sample points
Bo1.1_maxNdvi = extract(maxStack, Bo1.1, buffer=50, fun=mean, na.rm=T, weights = T,
normalizeWeigths = T)
Bo1.1_ts = as.numeric(Bo1.1_maxNdvi)
write.csv(Bo1.1_ts, file= "F:/pointTimeSeriesCsv/Bo1.1_ts.csv")

Bo1.3_maxNdvi = extract(maxStack, Bo1.3,buffer=50, fun=mean, na.rm=T, weights = T,
normalizeWeigths = T)
Bo1.3_ts = as.numeric(Bo1.3_maxNdvi)
write.csv(Bo1.3_ts, file= "F:/pointTimeSeriesCsv/Bo1.3_ts.csv")

Bo1.4_maxNdvi = extract(maxStack,Bo1.4, buffer=50, fun=mean, na.rm=T, weights = T,
normalizeWeigths = T)
Bo1.4_ts = as.numeric(Bo1.4_maxNdvi)
write.csv(Bo1.4_ts, file= "F:/pointTimeSeriesCsv/Bo1.4_ts.csv")

Bo1.6_maxNdvi = extract(maxStack, Bo1.6, buffer=50, fun=mean, na.rm=T, weights = T,
normalizeWeigths = T)
Bo1.6_ts = as.numeric(Bo1.6_maxNdvi)
write.csv(Bo1.6_ts, file= "F:/pointTimeSeriesCsv/Bo1.6_ts.csv")

#Colesdalen sample points
Col1_maxNdvi = extract(maxStack, Col1, buffer=50, fun=mean, na.rm=T, weights = T,
normalizeWeigths = T)
Col1_ts = as.numeric(Col1_maxNdvi)
write.csv(Col1_ts, file= "F:/pointTimeSeriesCsv/Col1_ts.csv")
```

```
Col2_maxNdvi = extract(maxStack, Col2, buffer=50, fun=mean, na.rm=T, weights = T,
normalizeWeigths = T)
Col2_ts = as.numeric(Col2_maxNdvi)
write.csv(Col2_ts, file= "F:/pointTimeSeriesCsv/Col2_ts.csv")

Col4_maxNdvi = extract(maxStack, Col4, buffer=50, fun=mean, na.rm=T, weights = T,
normalizeWeigths = T)
Col4_ts = as.numeric(Col4_maxNdvi)
write.csv(Col4_ts, file= "F:/pointTimeSeriesCsv/Col4_ts.csv")
```

Appendix H: Mask and visualize trend test results

```
#clear environment
rm(list = ls())
options(stringsAsFactors= FALSE)

#install.packages("rgdal")
#install.packages("raster")
#install.packages("stringr")
#install.packages("stats")
#install.packages("lubridate")
#install.packages("rkt")

library(rgdal)
library(raster)
library(stringr)
library(stats)
library(lubridate)
library(rkt)
library(viridis)
library(sp)
```

```
#DATA
mktStack = stack("F:/ data/tsStacks/mkTimeSerie.tif")
maxStack = stack("F:/ data/tsStacks/maxStack.tif")

#Theil-Sens slope estimator
thSlope = mktStack[[1]]
#p-value raster
pValue = mktStack[[2]]
#Kendall's TAU
kTau= mktStack[[3]]

#p-value mask raster
pValueMask = pValue
pValueMask[pValueMask > 0.05] = NA
#Tau-mask
tauMask = kTau
tauMask[tauMask < -0.4 & tauMask > 0.4] = NA

#NDVI1985
ndvi1985 = maxStack[[1]]
ndvi2018 = maxStack[[29]]

#Mask slope values with by significant p-values
pMasked = mask(thSlope, pValueMask)
#Mask slope by significant Kendalls Tau
maskedTHS= mask(pMasked, tauMask)
# select same pixels from Max NDVI composite from year 1985
ndvi1985 = maxStack[[1]]
maskedNDVI1985 = mask(ndvi1985 , maskedTHS)

#STATS
cellStats(ndvi1985, mean) #0.1317888
cellStats(maskedNDVI1985, mean) #0.1926941
cellStats(maskedTHS, mean) #0.005802191
```

```
# PERCENTUAL GROWTH OF MAX NDVI VALUES
ndvi85_mean = cellStats(maskedNDVI1985, mean)
nYears = 2019-1985
meanSlope = cellStats(maskedSl, mean)
ndviGrowth = meanSlope * nYears
percentualGrowth = (ndviGrowth / ndvi85_mean) * 100 #102.377% growth
#Min and max slopes
print(cellStats(maskedTHS, min)) # -0.03094007
print(cellStats(maskedTHS, max)) #0.0300209
hist(maskedTHS)

#Values expects vs measured
ndvi2018 = maxStack[[29]]
maskedNdvi2018 = mask(ndvi2018, maskedNDVI1985)
ndvi2018mean = cellStats(maskedNdvi2018, mean)
slopeEstimatedValues = ndvi85_mean * (ndviGrowth / ndvi85_mean + 1)

#Theil-Sens slope estimator
thSlope = mktStack[[1]]
#p-value raster
pValue = mktStack[[2]]
#Kendall's TAU
kTau= mktStack[[3]]

spplot(kTau, main = list("Kendall's Tau", cex = 4), col.regions = viridis(16), cuts = 15, colorkey
=list(labels = list(cex=2)))
spplot(pValue, main = list("p-value", cex = 4), col.regions = viridis(16), cuts = 15, colorkey
=list(labels = list(cex=2)))
spplot(thSlope, main = list("Theil-Sens slope", cex =4), col.regions = viridis(16), cuts = 15,
colorkey =list(labels = list(cex=2)))
```

Appendix I: Linear mixed effects model

```
#clear environment
rm(list=ls())
```

```
#install packages
install.packages("lme4")
install.packages("arm")
install.packages("ggplot2")
install.packages("tidyverse")
install.packages("viridis")
install.packages("fBasics")
install.packages("performance")

library(lme4)
library(arm)
library(ggplot2)
library(tidyverse)
library(viridis)
library(fBasics)
library(performance)

### READ DATA ###
rercaNDVI = read.csv("F:/ data/svalbardCaccAndPredictors.csv", header = T, sep = ";")

#Change one column name to more comprhernsible one
names(rercaNDVI)[3] = "Profile"

#Remove lines with NA values in accumulation rate column
rercaNDVI = subset(rercaNDVI, !is.na(rercaNDVI$C.m2.a))

### PRELIMINARY DATA STUDY ###
#check that site and core_id are read as factors
str(rercaNDVI)
#summary of data variables
summary(rercaNDVI)

#Observations per site are not evenly distributed
table(rercaNDVI$Profile, useNA = "no" )
```

```
#Cross-correlation between numeric parameters
cor(rercaNDVI[,c(4:10)], use="pairwise.complete.obs")

#PLOT average NDVI and apparent carbon accumulation rates per soil profiel plot
with(rercaNDVI,plot(Profile, moving3y_NDVI))
with(rercaNDVI,plot(Profile, C.m2.a))

#Plot NDVI and carbon accumulation relationship per site
plot = ggplot(data      = rercaNDVI,
       aes(x     = moving3y_NDVI,
           y     = C.m2.a,
           col   = Profile,
           group = Profile))+
  geom_point(size     = 4,
             alpha    = .9)+
  theme(legend.position = "right", text=element_text(size=25), plot.title = element_text(size = 42))+
  geom_smooth(method = lm,
              se     = FALSE,
              size   = 1,
              alpha  = .8)+
  xlab("NDVI")+
  ylab("g C m-2 y-1")+
  labs(title = "Soil profile-wise RERCA and NDVI relationship")

plot + scale_colour_viridis(discrete = T, option = "viridis")

### MODEL FITTING ###
#Intercept only model
icOnly = lmer(C.m2.a ~ 1 + (1 | Profile), data = rercaNDVI, REML = F)
#model summary
summary(icOnly)
#Intraclass correlation
icc(icOnly)
```

```
#R2
r2_nakagawa(icOnly, by_group = FALSE)
#95% confidence intervals for fixed parameters
confint(icOnly, oldNames=F, level=0.95, method="Wald")

#Random intercept with fixed effect
r.ic = lmer(C.m2.a ~ 1+ moving3y_NDVI +(1 | Profile), data = rercaNDVI, REML=F)
#summary
summary(r.ic)
#intraclass correlation
icc(r.ic)
#R2
r2_nakagawa(r.ic, by_group = FALSE)
#95% confidence intervals for fixed parameters
confint(r.ic, oldNames=F, level=0.95, method="Wald")

#full model
fullModel = lmer(C.m2.a ~ 1+ moving3y_NDVI +(1 + moving3y_NDVI | Profile), data =
rercaNDVI, REML=F)
summary(fullModel)
#intraclass correlation
icc(fullModel)
#R2
r2_nakagawa(fullModel, by_group = FALSE)
#95% confidence intervals for fixed parameters
confint(fullModel, oldNames=F, level=0.95, method="Wald")
### ANOVA TEST ###
anova(icOnly, r.ic, fullModel)
compare_performance(icOnly, r.ic, fullModel)

#Test singularity
isSingular(icOnly)
isSingular(r.ic)
isSingular(fullModel)
```

```
#homoscedasticity of model residuals
plot(icOnly)
plot(r.ic)
plot(fullModel)

#Test normality of residuals
#IC only
shapiroTest(resid(r.ic))
qqnorm(resid(r.ic))
qqline(resid(r.ic), col = "red")

#random IC
shapiroTest(resid(icOnly))
qqnorm(resid(icOnly))
qqline(resid(icOnly), col = "red")

#full model
shapiroTest(resid(fullModel))
qqnorm(resid(fullModel))
qqline(resid(fullModel), col = "red")

### MODEL FIT SUMMARY PLOT ###
ggplot(fortify(fullModel), aes(moving3y_NDVI, C.m2.a, color=Profile)) +
  stat_summary(fun.data=mean_se, geom="pointrange", size = 1.8, alpha = 0.9 ) +
  stat_summary(aes(y=.fitted), fun=mean, geom="line", size = 1.6, alpha = 0.9)+
  theme(legend.position = "right", text=element_text(size=25), plot.title = element_text(size = 42,
hjust=0.5))+
  xlab("NDVI")+
  ylab("g C m-2 y-1")+
  labs(title = "Full model")
```